Targeted delivery and MRI tracking of magnetically labelled cells

Johannes Riegler

Submitted for the degree of

Doctor of Philosophy in Bioengineering

September 2011

Centre for Mathematics and Physics in the Life Sciences and Experimental Biology (CoMPLEX)

and

Centre for Advanced Biomedical Imaging (CABI), Department of Medicine and Institute of Child Health

University College London

Declaration

I, Johannes Riegler, confirm that the work presented in this thesis is my own work, except where stated otherwise in the text. This work is based on research which has been conducted by me, during the time period from October 2009 to August 2011 at the University College London.

Johannes Riegler

13th of March 2012

Abstract

The realisation of the therapeutic potential of cellular therapies will depend on our ability to deliver these cells to selected positions in the body where they can find a suitable micro-environment to flourish. Additionally our scientific understanding would befit from studies which can assess the behaviour of cells at specific locations inside the body.

Magnetic cell delivery is a potential technology which might allow realising these premises. The major advantage of magnetic delivery compared to other delivery strategies is the ability to spatially localise entities in the body via externally applied magnetic fields. However, the fast decline of these fields with increasing distances is posing a major challenge for its in vivo application.

The aim of this thesis was to investigate potential magnetic delivery approaches which can circumvent some of the typical limitations of this technique. Two different approaches were explored to this end. The first approach was evaluating the feasibility of a magnetic resonance imaging (MRI) system to steer labelled cells in arteries. Such an approach could take advantage of the imaging capabilities of magnetic resonance systems and combine these with steering to interactively guide cells or other entities of interest to a target area.

The second approach was addressing the feasibility of theoretical optimisations and the scalability of experimental results. For that, human MRI data was used to derive geometrical models of the blood vessels to which cells were to be delivered in this scenario. Finite element modelling was then used to explore potential magnet arrangements with the aim to maximise the force acting on cells over all target vessels. The best performing arrangement was then used for computational fluid dynamics simulations to test the possibility of cell capture from the flowing blood stream. Finally the possibility to scale-down such an arrangement to the dimensions of an animal model without changing the forces acting on cells was investigated.

Cells have to be labelled with magnetic materials in order to allow their magnetic actuation. This magnetic materials cause a distinctive contrast on MRI images. The potential of this imaging modality for cell tracking has been illustrated with an in vivo example for cell tracking in a rat heart and an in vitro example for a tissue engineering application.

Experiments with a preclinical MRI system illustrated the feasibility of cell steering with MRI indicating that such an approach could be useful for magnetic cell delivery. Computational models for the evaluation of magnet arrangements allowed the in-silico assessment of their potential and could be used to improve the experimental design of pre-clinical studies.

Acknowledgments

This thesis would not have been possible without the help of Panos Kyrtatos who showed me the essentials of magnetic targeting, Anthony Price who showed me the wonders of magnetic resonance imaging, Kevin Lau who helped me with computational fluid dynamics models, Ana Garcia-Prieto who introduced me to finite element models, Mankin Choy who told me the intricacies of animal models and Baptiste Allain who helped with confocal endoscopy.

I am indebted to my supervisors Dr. Mark Lythgoe and Professor Quentin Pankhurst for their help and support through this project. I am also grateful for the pleasant work environment provided which gave me the freedom to explore whatever caught my interest.

I would like to thank my colleges at CABI; Ken Cheung, Jon Cleary, Jack Wells, Bernard Siow, Simon Walker Samuel, Tammy Kalber, Adam Bader, Inmaculada Villar, Francesca Norris, Adrienne Campell, Ben Duffy, Isabel Christie, Simon Richardosn, Rajiv Ramasawmy, Niral Patel, Miguel Goncalves and my colleges at CoMPLEX; Max Ahmed, Arturo Araujo, Victoria Harris, Raphaela Heussen, Gwenan Knight, Julia Krupic, Dorothy Kuipers, Charles Mullon, Lorette Noriet, David Schulz and Ross Williams.

Finally, my eternal gratitude goes to my girlfriend Astrid Gillich and my family for their continued support and understanding.

Publications arising from research conducted in the context of this thesis

J. Riegler, K.D. Lau, A. Garcia-Prieto, A.N. Price, T. Richards, Q.A. Pankhurst, M.F. Lythgoe, “Magnetic cell delivery for peripheral arterial disease: A theoretical framework.” *Medical Physics* **38**, 3932-43 (2011)

N. Smart, S. Bollini, K.N. Dubé, J.M. Vieira, B. Zhou, S. Davidson, D. Yellon, **J. Riegler**, A.N. Price, M.F. Lythgoe, W.T. Pu and P.R. Riley, “De novo cardiomyocytes from within the activated adult heart after injury.” *Nature* **474**, 640-4 (2011)

S. Bollini, K.K. Cheung, **J. Riegler**, X. Dong, N. Smart, M. Ghionzoli, S.P. Loukogeorgakis, P. Maghsoudlou, K.N. Dubé, P.R. Riley, P. M.F. Lythgoe and P. De Coppi, “Amniotic Fluid Stem Cells Are Cardioprotective Following Acute Myocardial Infarction.”, *Stem Cells and Development* **20**, 1-10 (2011).

J. Riegler, B. Allain, R. J. Cook, M. F. Lythgoe and Q. A. Pankhurst, "Magnetically assisted delivery of cells using a magnetic resonance imaging system." *Journal of Physics D: Applied Physics* **44**, 055001-055011 (2011).

J. Riegler, J. A. Wells, P. G. Kyrtatos, A. N. Price, Q. A. Pankhurst and M. F. Lythgoe, "Targeted magnetic delivery and tracking of cells using a magnetic resonance imaging system." *Biomaterials* **31**, 5366-5371 (2010).

J. Riegler, K. K. Cheung, Y. F. Man, J. O. Cleary, A. N. Price and M. F. Lythgoe, "Comparison of segmentation methods for MRI measurement of cardiac function in rats." *Journal of Magnetic Resonance Imaging* **32**, 869-877 (2010).

S. Bollini, M. Pozzobon, M. Nobles, **J. Riegler**, X. Dong, M. Piccoli, A. Chiavegato, A. Price, M. Ghionzoli, K. Cheung, A. Cabrelle, P. O. Mahoney, E. Cozzi, S. Sartore, A. Tinker, M. Lythgoe and P. De Coppi, "In Vitro and In Vivo Cardiomyogenic Differentiation of Amniotic Fluid Stem Cells." *Stem Cell Reviews and Reports* **7**, 1-17 (2010).

A. N. Price, K. K. Cheung, J. O. Cleary, A. E. Campbell, **J. Riegler** and M. F. Lythgoe, "Cardiovascular Magnetic Resonance Imaging in Experimental Models." *The Open Cardiovascular Medicine Journal* **4**, 278-292 (2010).

Table of content

List of figures

List of tables

Abbreviations

2D	Two dimensional
3D	Three dimensional
AMF	Alternating magnetic field
ASC	Adult stem cell
BMC	Bone marrow cell
CFD	Computational fluid dynamics
DMEM	Dulbecco's Modified Eagle Medium
DNA	Deoxyribonucleic acid
DTPA	Diethylenetriaminepentaacetate
EPC	Endothelial progenitor cell
ESC	Embryonic stem cell
FA	Flip angle
FDA	Food and drug administration of the United States
FE	Frequency encode gradient
FEM	Finite element model
FT	Fourier transformation
GMP	Good manufacturing practice
hESC	Human embryonic stem cell
iPSC	Induced pluripotent cell
LAD	Left anterior descending coronary artery
MEM	Minimum essential media
MI	Myocardial infarction
MNC	Mononuclear cell
MR	Magnetic resonance
MRI	Magnetic resonance imaging
MRT	Magnetic resonance targeting
MSC	Mesenchymal stem cell
NbTi	Niobium titanium
NdFeB	Neodymium Iron Boron
NSA	Number of signal averages
PAD	Peripheral arterial disease
PBS	Phosphate buffered saline
PCR	Polymerase chain reaction

PE	Phase encode gradient
PET	Positron emission tomography
PSU	Power supply unit
rAFSC	Rat amniotic fluid stem cell
RF	Radio frequency
SPECT	Single-photon emission computed tomography
SPION	Superparamagnetic iron oxide nanoparticles
SPM	Superparamagnetic
SS	Slice selection gradient
TE	Time to echo
TR	Time to repletion

Introduction to the layout of this thesis

This thesis consists of 8 chapters whereby the first three chapters give some theoretical background and motivation for the conducted work. The experimental chapters 4-7 start with a brief introduction laying out additional background information which has not been stated in chapters 1-3. Each of the experimental chapters contains Materials and Methods relevant to the particular chapter. This is followed by Results, Discussion and Conclusion. General conclusions and future directions are given in chapter 8.

1 The potential of cellular therapies for vascular diseases

Vascular diseases have a high prevalence in the industrialised world and have now become the most common cause of death globally. Vascular diseases include myocardial infarction, peripheral arterial disease and stroke. All of these diseases lead to extensive cell death in effected organs exceeding the natural regenerative potential of these organs. The discovery of stem cells has sparked hopes to use the high regenerative potential of these cells to replace the dead cells and repair the effected organs. This chapter provides an overview over the diseases of relevance for this thesis and the current state of cellular therapies for each of them. Most of these cellular therapies require the ability to deliver cells to a specific location and monitor their behaviour at that location. Problems related to that will be highlighted as they are the primary concern of this thesis. At the end of the chapter a brief definition will be given for cell types used for this thesis.

1.1 Vascular diseases and stem cell therapies

1.1.1 Myocardial infarction

Coronary artery disease is the most common cause of death in the industrialised world[1]. Coronary artery disease leads to reduced blood supply of the myocardium leading to ischemia (heart attack). Cardiac ischemia causes a chain of events starting with cell death, inflammation, scar tissue formation and remodelling which ultimately leads to heart failure. Despite the improvements due to drugs such as statins the only long term cure is heart transplantation.

The discovery of stem and progenitor cells has led to new hopes that a regenerative medicine approach might be able to restore cardiac function and prevent heart failure. This hope rests on the hypothesis that stem cells or progenitor cells might be able to replicate and differentiate into cardiomyocytes as well as vascular cells replacing dead cells and functionally integrate with neighbouring cells. In order to test this hypothesis two principle strategies might be tested. Firstly it might be possible to mobilise stem or progenitor cells in situ in the heart or hematopoietic system (provided they have sufficient trans-differentiation potential) in sufficient numbers to achieve meaningful repair. Or alternatively externally amplified cells of autologous or homologous origin delivered to the site of injury might be able to survive and functional integrate into the existing tissue.

Most of the research so far has focused on the cell delivery approach. The potential advantages of such an approach are better control over the cell type, amplification potential, delivery time, delivery route, delivery site and potentially genetic manipulation. Potential disadvantages are higher costs (GMP facilities), availability of controlled and approved culture media, ensuring cell stability and identity and the risk for immune reactions and teratoma formation depending on the cell type used. All of the above points are research questions for which we have currently no answers.

The question to start with for a cell delivery approach is: what is the optimum cell type? Conceptually ESCs would offer the greatest potential as they should be able to form new cardiomyocytes and blood vessels due to their totipotent nature. However, this versatility comes with a high risk of teratoma formation and ethical question of potential ESCs sources (ESCs are derived from the inner cell mass of blastocysts (embryos)). ESCs and human ESCs (hESCs) have been used in animal experiments where they showed the ability to repair the AV node[2;3] and improve

cardiac function[4-6]. Human ESC derived cardiomyocytes were able to survive and maturate in immunodeficient rats and mice for at least 12 weeks[6]. However, transplanted cells were surrounded by fibrotic tissue which separated them from the host myocardium. Functional integration of hESC derived cells could not be observed in rodents[7] which might be explained by the differences in their heart rates. The improved cardiac function is hence most likely due to paracrine effects (the release of small signalling molecules) as has been observed for other cell types.

Bone marrow cells (BMCs) (from bone marrow aspirations) and mesenchymal stem cells (MSCs) (isolated from the bone marrow, peripheral blood, adipose tissue or amnion) have been used most frequently for cell transplantation experiments in animals[8-10]. BMCs are a mixed population of cells containing hematopoietic stem and progenitor cells (multipotent) as wells mesenchymal stem cells (multipotent). Mononuclear cells (MNCs) are hematopoietic progenitors of macrophages. This subpopulation of BMCs will be used as a model cell type together with MSCs in chapter 4. Functional improvements have been reported in most of these cell transplantation studies but cell survival is generally poor and strong inflammatory responses have been observed by some. Cell differentiation and integration seem to be a rare event and positive effects are most likely due to paracrine effects[11]. BMCs and MSCs have been used phase 1 and phase 2 clinical trials[12;13]. These trials showed only marginal improvements in cardiac function, generally less than 5% of ejection fraction (pumping efficiency of the heart). These are modest effects compared to some animal experiments indicating the need for improved animal models and assessment standards.

Particular pressing questions in the context of cell delivery after myocardial infarction are: i) what is the right microenvironment to promote cell survival and differentiation, ii) do we have to suppress scar formation, iii) should cells be delivered before or after the inflammatory phase? A question which is of particular interest in context of this thesis is the need for an optimised cell delivery strategy. Currently used intravenous delivery strategies are inefficient and retain less than 5 % of cells in the heart[14]. This can lead to unwanted side effects such as micro emboli in lung and brain and loss of precious cells. Even direct injection into the myocardium has a low retention efficiency but this might be improved via magnetic targeting[15]. Potential methods for magnetic cell delivery will be discussed in chapters (2 and 4) while cell tracking will be illustrated in chapter 7.

The discovery of progenitor cells in the heart[16] and evidence for the trans-differentiation potential of haematopoietic cells towards cardiomyocytes[8] has led to hopes that it might be possible to increase the regenerative potential of an adult human heart. This is particular appealing as the delivery of small molecules or proteins might be sufficient to realise that potential without the need for cell transplantation and the problems associated with it. However, it needs to be proven that this repair potential is sufficient and that it can be activated without causing cell growth in other organs.

1.1.2 Atherosclerosis

Peripheral arterial disease (PAD) is one of the major manifestations of atherosclerosis leading to the obstruction of blood flow in major arteries, most commonly in the pelvis and legs. Prevalence of PAD is approximately 12% for people of more than 60 years of age in the United States, leading to at least 8 million Americans affected[17]. Major risk factors for PAD are similar to those for atherosclerotic diseases in the heart and brain such as advanced age, smoking, diabetes, dislipidema (high blood cholesterol levels) and hypertension. With aging populations and a rise in diabetes in the industrialised world there is an increasing prevalence of PAD[18]. Although PAD is predictive for other cardiovascular events many patients are asymptomatic as other complications such as stroke or heart disease dictate patient symptomatology[19]. In those who are symptomatic, it presents with progressive cramp in the calves on walking (intermittent claudication).

PAD can lead to critical limb ischemia, particularly in diabetics, where the limb is chronically undersupplied with oxygen and nutrients. Symptoms of critical limb ischemia are rest pain, cold or numb feet and non healing ulcers or gangrene. Diabetic PAD is the leading cause of amputation in the Western world.

Treatment of PAD includes life style changes, exercise and risk factor modification. Intervention to alleviate symptoms and prevent amputation require the restoration of pulsatile blood flow to the feet[20;21]. This can be achieved via balloon angioplasty, stenting or surgical intervention such as bypass grafting or endarterectomy (surgical removal of a blockage). Catheter based interventions for angioplasty carry lower risks compared to surgery and reduce the duration of hospitalisation. However, despite initial improvements in blood flow, long term patency following angioplasty is limited by vascular restenosis and neointimal hyperplasia[22;23]. Neointimal hyperplasia, excessive growth of smooth muscle cells in

the blood vessel, is a response of the vessel wall to injury. Several potential solutions for this problem have been suggested including: drug eluting stents[24], cellular therapies[25;26] and specific surface coatings for stents[27], which has led to some increase in patency.

As traditional techniques are reaching their limits[24;27], new avenues leading to cellular therapy via specific cell capture are currently being explored[28]. Drug eluting stents have shown promising results for short term outcome. However, the long term outcome did not improve as vascular healing is delayed[29]. In the last decade, cellular therapies have received more attention particularly since Ashara et al.[30] discovered endothelial progenitor cells (EPCs) in the circulating blood.

Endothelial progenitor cells are a population of bone marrow-derived cells which incorporate into sites of neovascularisation and endothelial injury. Animal studies indicate that the administration of EPCs to sites of vascular injury leads to re-endothelialisation and prolonged vessel patency[25;26;31]. Another area of PAD for which cellular therapies have been tested in clinical trials is to improve collateralization (small blood vessel bridging areas where major blood vessels are blocked start to expand in number and diameter) and neoangenesis (the formation of new blood vessels). Most of these trails have used either BMCs or EPCs[32]. There is some evidence that these therapies with direct cell injection into the muscle may act in a paracrine manner increasing the mobilisation of resident progenitor cells[33]. For cellular therapies with the aim to improve re-endothelisation, the rarity of EPCs and other potential cells combined with low retention efficiencies in arteries poses significant difficulties. Furthermore, EPC concentrations and activity are reduced in patients with PAD due to the associated risk factors[34]; taken together this results in a suboptimal therapy. There is a clear clinical need to develop a therapeutic strategy to target these cells to the area of need and maximise their retention. A potential solution to ensure localised cell delivery and retention with high efficiency will be shown in chapter 6.

1.1.3 General considerations for cell based therapies

Cellular therapies, particular stem and progenitor cell based therapies offer unprecedented potential for new therapies. In order to unlock this potential it is necessary to develop a better understanding of potential risks and benefits in order to define acceptable risk limits for each potential application and advance from preclinical to clinical trials.

The complexity of cellular therapies and their wide range of potential interactions with the recipient organism will need new assessment criteria for preclinical and clinical safety evaluation. This safety issues concern primarily the following points: manufacturing consistency, identification / removable of undifferentiated cells, genetic stability, delivery route / device, biodistribution, tumorigenicity, immunogenicity, and clinical / preclinical endpoint assessment.

Manufacturing consistency should ensure that the cell product in its final formulation is always within specification. In order to achieve that, assays need to be established which can test for cell activity, purity, differentiation status, and more conventional tests to ensure the product is free from contaminations including viruses and prions. Good manufacturing practice will additionally require the full characterisation of all materials used during production which might be difficult if not chemically defined materials such as serum are needed. Achieving manufacturing consistency will be particular challenging for products which are based on the extensive expansion of autologous or allogenic cells as compared to a stable cell line which is to be used for many patients.

Identifying and removing undifferentiated cells will be part of the manufacturing process but deserves special considerations as tumorigenicity is one of the major safety concerns. Efficient differentiation procedures will be necessary as well at test procedures which are sensitive enough to detect small numbers of undifferentiated cells (e.g. PCR for specific genes) und means of removing them.

Extensive expansion of cells in vitro leads to the accumulation of mutations and genetic instability including chromosomal aberrations. As chromosomal aberrations are considered a hallmark of cacner[35], tests for chromosomal integrity and potential mutations need to be part of the final product screening. In addition to these random events there is evidence for inherent instabilities in ESCs , adult stem cells and induced pluripotent stem cells (iPSCs) [36-38]. Most of this changes are time depended. It might hence be necessary to define an acceptable culture time or number of population doublings to reduce the risk of genetic instability.

There are many different possibilities to deliver manufactured cells. Preclinical testing should assess and identify the optimum delivery strategy for each particular treatment application. The selected delivery device needs to be tested together with the final product before it can be used clinically. Such a device might also need

approval. Safety considerations for a delivery device have to include potential accumulation at non target sides and increased difficulties to track cells if delivered into the circulatory system.

Depending on the route of delivery it might be necessary to assess only one organ system or the whole body to estimate the bio-distribution. This should ideally be done with highly sensitive and specific imaging modalities. It would also be desirable if that could include monitoring gene expression and differentiation status. In order to assess the latter aspect, genetic modification to introduce a marker gene might be necessary. Of course it needs to be established, that this does not interfere with therapeutic cell function. Once the question of bio-distribution has been assessed in a preclinical model, suitable means for cell tracking in the clinical setting have to be established. Additional considerations of potential long term immunogenic effects of marker gene expression in humans need to be considered.

Tumorigenicity is the biggest risk factor for stem and progenitor based therapies as the potential to form teratoma is part of their defining characteristics. As mentioned above ensuring undifferentiated cells are not part of the final product is essential. This risk is difficult to assess in preclinical models as most of the will be using immune suppression. Careful assessments to quantify that risk in clinical trials will be necessary. A recent report about a donor derived brain tumour which has been detected after neural stem cell transplantation has highlighted this problem[39]. In order to control this risk the insertion of an activatable apoptosis gene might be necessary[40]. However, this will raise additional regulatory hurdles as cells might be classified as genetically modified organism and cellular therapies.

Immunogenicity is the second biggest risk factor following tumorigenicity. Although some stem cells show some immune privileges it is questionable if that is the case for their differentiated progeny. This will be less of an issue if iPSCs prove suitable for clinical applications. In order to get a better understand of that risk, analogous cells could be derived and tested in animal models. But this can only partially address this problem.

All above mentioned risks have to be compared against potential patient benefit. Defining suitable criteria for the assessment of treatment success is hence very important. Ideally such criteria should be easily and unambiguously measurable in both animal model and humans. These criteria should be standardised across

preclinical experiments and clinical trials. An example of unnecessary confusion and ambiguity can be found in the field of cellular therapies for myocardial infarction were a range of methods that are not easily comparable from histology to MRI has been used.

2 Magnetic delivery of biological entities

Chapter one provided an overview over some vascular diseases and the potential of cellular therapies for them. As indicated previously, efficient cell delivery is necessary for the success of such interventions. Efficient cell delivery and retention might be achieved via magnetic targeting. This chapter will therefore give a general description of concepts related to magnetism which are used throughout this thesis. Following these basic definitions, different applications of magnetic particles in the field of medicine will be discussed. These include magnetic separation, magnetic cell and drug delivery, magnetic hyperthermia and finally magnetic cell tracking via magnetic resonance imaging.

2.1 Definitions and basic principles

2.1.1 Magnetic fields

A magnetic field is an area of space with increased energy density and an energy gradient to its surrounding. A magnetic field can be detected via the force it exerts on a moving charge (Lorentz force), the torque on a magnetic dipole or the alignment of electron and nuclear spins. The most common phenomena of these is the reorientation of a magnetic needle (dipole) by the magnetic field of the earth.

The Lorentz force is given by

$$\boldsymbol{F}_B = q\boldsymbol{v} \times \boldsymbol{B} \,, \qquad \text{Eq. 2.1}$$

with q the charge in Coulomb, $\boldsymbol{v}$ the velocity in m/s and $\boldsymbol{B}$ the magnetic flux density in Tesla.

Magnetic fields are produced by moving electrical charges or the interaction of spin and orbital moments of electrons. Magnetic fields due to current carrying conductors are an example for the former case while permanent magnets are an example for the latter. Although permanent magnets cannot be explained adequately without quantum mechanics a classical explanation can be given by considering electrons as circulating current loops. Magnetic fields generated by time invariant moving electrical currents can be described by the Biot-Savart law:

$$\boldsymbol{B} = \int \frac{\mu_0}{4\pi} \frac{I\, d\boldsymbol{l} \times \hat{\boldsymbol{r}}}{r^2} \qquad \text{Eq. 2.2}$$

where μ_0 is the permeability of free space, I the current in Ampere, $\boldsymbol{l}$ the vector of the current carrying element, $\hat{\boldsymbol{r}}$ unit vector to and r the distance between conductor element and field evaluation point.

The most important equations for magnetism are the Maxwell equations which unified several existing laws from Gauss, Ampere and Faraday. Maxwell's four famous equations showed that electricity and magnetism are coupled phenomena and that light is a form of electromagnetic radiation. These four equations are given in differential form with their names as:

Gauss's law of electric fields

$$\boldsymbol{\nabla} \cdot \boldsymbol{E} = \frac{p}{\varepsilon_0} \ , \qquad \text{Eq. 2.3}$$

Gauss's law of magnetic fields

$$\boldsymbol{\nabla} \cdot \boldsymbol{B} = 0 \ , \qquad \text{Eq. 2.4}$$

Faraday's law

$$\boldsymbol{\nabla} \times \boldsymbol{E} = -\frac{d\boldsymbol{B}}{dt} \quad \text{and} \qquad \text{Eq. 2.5}$$

the Ampere-Maxwell law

$$\boldsymbol{\nabla} \times \boldsymbol{B} = \mu_0 \left(\boldsymbol{J} + \varepsilon_0 \frac{d\boldsymbol{E}}{dt} \right) \ , \qquad \text{Eq. 2.6}$$

with $\boldsymbol{E}$ the electric field in V/m, p the charge density in C/m^3, ε_0 the electric permittivity of free space and $\boldsymbol{J}$ the electric current density in A/m^2.

For this thesis we are mainly concerned with equations 2.4 and 2.6 from which some basic properties of magnetic fields can be deduced. Gauss's law shows that the divergence of magnetic fields is zero at any point. This means that the net magnetic flux going through any real or imaginary surface is zero. This is a direct consequence of closed magnetic field lines and the non-existence of magnetic monopoles. The Ampere-Maxwell law states that a circulating magnetic field is generated by an electric current and time variant electric fields. This was first discovered by Oersted when he saw that a current running through a wire led to the deflection of a compass needle next to it.

The unit for the magnetic field strength $\boldsymbol{H}$ is A/m which follows from its definition as the field produced in the centre of a current loop with 1 meter in diameter carrying one Ampere. Defining the magnetic field strength in this way is useful to distinguish between the applied field and the magnetic flux density or $\boldsymbol{B}$ field which gives the magnetic response at a particular point due to the presence of $\boldsymbol{H}$ and matter. The relation between magnetic induction and magnetic field is given by

$$\boldsymbol{B} = \mu_0(\boldsymbol{H} + \boldsymbol{M}) \ , \qquad \text{Eq. 2.7}$$

with μ_0 the permeability of space ($4\pi \times 10^{-7} H\, m^{-1}$) and $\boldsymbol{M}$ the magnetisation of the material in A/m.

2.1.2 Magnetic properties of matter

Materials can be classified according to their response to an external magnetic field. A dimensionless parameter to describe this is the magnetic susceptibility which is defined as

$$\chi = \frac{M}{H} \quad . \qquad \text{Eq. 2.8}$$

Materials with a negative susceptibility (typically ≈-10^{-5}) are classified as diamagnetic while materials with small positive values (10^{-2}-10^{-5}) are classified as paramagnetic. A special class of ferromagnetic materials are antiferromagnetic materials which show also low suseceptibilites. High suseceptibities (10^{2}-10^{5}) are observed for ferromagnetic, ferrimagnetic and helimagnetic materials.

Diamagnetism is caused by changes in the orbital motion of electrons due to the presence of a magnetic field. This leads to a weak magnetisation which opposes the external magnetic field. Diamagnetism is present in all atoms but can only be observed in materials which show no other form of magnetic behaviour for example copper, silver, bismuth and water.

Paramagnetism is caused by the alignment of atomic magnetic moments with the external field. The spin of unpaired electrons is the primary source of the atomic magnetic moment with contributions from orbital angular momentum. Magnetic moments do not interact in paramagnetic materials and are randomly orientated due to thermal reorientation when the thermal energy is higher than the magnetic. This makes the susceptibility inversely temperature depended. The magnetisation of paramagnets is proportional to $\boldsymbol{H}$ for a low field strength but reaches saturation at a high field strength. Typical materials for this group are aluminium, magnesium and oxygen.

Ferromagnetism is observed in metals such as iron, nickel, cobalt and some rear earth elements. It is caused by the interaction of atomic magnetic moments from unpaired electron spins leading to the alignment of moments over big regions called domains. Moments are aligned parallel in domains due to the exchange interaction of spins but different domains have different random alignment. If they are exposed to external magnetic fields, domains boundaries start to move and increase the net alignment of all domains parallel to the external field. Increasing the temperature beyond a critical temperature the so called Curie temperature increases the thermal energy beyond the interaction energy leading to paramagnetic

behaviour. Ferromagnetic materials can retain their magnetisation (residual flux density B_r) once they have been magnetised. This magnetisation can be reversed with a big enough magnetic field, by the coercive force $\boldsymbol{H_C}$. They also show signs of magnetic memory which is called hysteresis. Another characteristic phenomenon of ferromagnetism is the saturation magnetisation M_S which is the maximum magnetisation which can be achieved. B-H curves are frequently used to illustrate the complex behaviour of ferromagnetic materials. The crystal structure of these materials has an influence on molecular interactions and causes non-isotropic magnetic behaviour.

Antiferromagnetism is found in materials with particular crystal structures leading to antiparallel alignment of magnetic moments between sublattices and parallel alignment within. As these magnetic moments between sublattices are equal, antiferromagnets show no net magnetisation in the absence of a magnetic field. This magnetic behaviour is commonly found in transition metal oxides such as FeO, CoO and MnO. Antiferromagnets show also a transition from an ordered state to an unordered state similar to the Curie temperature, which is called Neel temperature.

Ferrimagnetism is a special case of antiferromagnetism where the magnetic moments of sublattices are unequal resulting in a net magnetisation. Sublattices can be made up by different ions e.g. Fe^{2+} and Fe^{3+} separated by oxygen. They show hysteresis, saturation magnetisation and a Curie temperature at which the ordered state is lost as in ferromagnetic materials. Some of the materials have a temperature below the Curie temperature where the magnetic moments of the sublattices are equal, the magnetisation compensation point. Ferrimagnetism was discovered in ferrites such as: Fe_3O_4, γ-Fe_2O_3 and MO*Fe_2O_3 with M being a transition metal.

Superparamagnetism is found in ferro- and ferrimagnetic nanoparticles where the particle core consists of a single magnetic domain. This allows for random reorientation of the magnetisation orientation due to thermal energy. The mean time between these re-orientations is called Neel relaxation time. Superparamagnetic particle retain no magnetisation after the removal of a magnetic field but exhibit magnetisation similar to paramagnets in a magnetic field. However, their magnetisation is much higher than observed for paramagnets and they show saturation similar to ferro- and ferrimagnetic materials. The magnetisation as a

function of the applied field can be approximated by a Langevin function (see equation 2.13).

Helimagnetism is found in materials with a crystal structure leading to ferromagnetic and antiferromagnetic interactions. Magnetic moments are aligned parallel in one crystal plane while subsequent planes have their moments inclined at an angle leading to a helical structure. This form of magnetism can be observed in dysprosium, holmium, terbium and other rare earth elements at low temperatures.

2.1.3 Magnetic forces

Gauss's law for magnetic fields shows that magnetic moments can only exist as magnetic dipoles. The dipole moment $\boldsymbol{m}$ of a loop with current I is a vector normal to the plane of the loop given by

$$\boldsymbol{m} = I\, r^2 \pi \quad , \qquad \text{Eq. 2.9}$$

with r being the radius of the current loop. The magnetic field of a bar magnet and a current loop are similar and can also be represented by two magnetic poles p separated by distance $\boldsymbol{l}$ giving,

$$\boldsymbol{m} = p\boldsymbol{l} \quad . \qquad \text{Eq. 2.10}$$

Descriptions of the magnetic moment as a current loop or a magnetic dipole are interchangeable. However it has to be remembered that a current loop has no effective pole separation while a dipole has no effective cross section.

A magnetic moment experiences two forces in a magnetic field: a torque to align its dipole moment and a translational force towards regions of high flux density if a field gradient is present. The torque is given by

$$\boldsymbol{\tau} = \boldsymbol{m} \times \boldsymbol{B} \quad , \qquad \text{Eq. 2.11}$$

while a translational force is given by

$$\boldsymbol{F_m} = (\boldsymbol{m} \cdot \boldsymbol{\nabla})\boldsymbol{B} \quad . \qquad \text{Eq. 2.11}$$

For biological applications of magnetic particles it is convenient rewrite the above equation as[41]

$$\boldsymbol{F_m} = \frac{V_m\, \Delta\chi}{\mu_0}(\boldsymbol{B} \cdot \boldsymbol{\nabla})\boldsymbol{B} \quad . \qquad \text{Eq. 2.12}$$

with V_m being the volume of magnetic material and $\Delta\chi$ the susceptibility difference between the magnetic material and its surrounding medium. As mentioned in section 2.1.2 the susceptibility is only directly proportional to the magnetic field for paramagnetic materials. However, the most commonly used materials for magnetic particles are iron oxides that show ferrimagnetic behaviour. It is hence necessary to replace $\Delta\chi$ by a function that models this behaviour such as the Langevin approximation:

$$M/M_s = \coth(\varepsilon) - \frac{1}{\varepsilon} \text{ and} \qquad \text{Eq. 2.13}$$

$$\varepsilon = \frac{\pi \mathrm{D}^3 \mu_0 \mathrm{M_s} \left|\frac{\mathbf{B}}{\mu_0}\right|}{6 \mathrm{k_b T}}, \qquad \text{Eq. 2.14}$$

whereby $\mathrm{M_s}$ is the saturation magnetisation of the particle, D the particle diameter, T temperature, $\left|\frac{\mathrm{B}}{\mu_0}\right|$ magnitude of the magnetic field strength and $\mathrm{k_b}$ Boltzmann's constant.

Magnetic particles for the context of this thesis are nanometre to micrometre sized particles with superparamagnetic (SPM) behaviour unless stated otherwise. This requires that crystal cores are in the size range of 10-30nm depending on the material and shape. The most common materials used are cobalt and iron whereby particles for biological applications are almost exclusively iron oxide particles.

Widely used methods for particle synthesis are colloidal synthesis in organic solvents and co-precipitation of Fe^{2+} and Fe^{3+} by a base in aqueous solutions[42]. These synthesised crystals need to be stabilised to make them useful for biological applications.

Important characteristics for the biological application are: low toxicity, biocompatibility, non-aggregating, high saturation magnetisation, no remnant magnetisation, monodispersity, chemical stability and low unspecific interaction with other biological entities. In order to achieve these properties iron oxide crystals are coated with suitable substances such as dextran, cellulose, alginate or peptides. These polymers can also be used to manufacture bigger particles by embedding several iron oxide crystals in one particle. Further modifications of particles surfaces can be performed to achieve specific binding to epitopes via antibodies or peptides,

absorption of nucleic acids via positive charges, attachment of drugs via organic linkers and others[43-46].

Another important parameter for magnetic particles is their hydrodynamic diameter that determines the drag force on particles, internalisation route for cell labelling and half-life time and clearance route in vivo[47]. The latter two phenomena are of course strongly influenced by other surface characteristics such as charge, hydrophobicity and molecular moieties.

2.2 The application of magnetic particles in medicine

2.2.1 Magnetic separation

Magnetic separation uses inherent or externally provided magnetic moments attached to the entities of interest in order to separate these entities from their surrounding media which has a very weak magnetic moment or is diamagnetic. Major advantages of magnetic separation are: high speed, direct extraction of entities of interest from complex media such as blood and food, extraction of substances from very dilute media, compatibility with downstream analysis techniques (e.g. immunohistochemistry and PCR) and it is a fairly cheap technique. These advantages led to widespread uses in life sciences applications with commercial companies providing a range of separation products.

Only a few biological entities such as red blood cells[48;49] and magnetotactic bacteria[50;51] have sufficient natural magnetic moment for their magnetic separation. All other entities need to be labelled with magnetic substances. Several magnetic substances such as magnetic proteins (ferritin)[52;53] and magnetic particles[41;54-63] have been used. However, magnetic nano- and micro-particles with superparamagnetic behaviour are used most frequently. In most cases affinity ligands with high specificity are used to separate the entities of interest such as: proteins[64;65], cells[55;56;60;61], viruses[66;67], ribonucleic acids[54;68], cell organelles[57], phages[69;70] and spermatozoa[71]. These affinity ligands: antibodies, peptides or organic molecules are attached to magnetic particles via adsorption[72], covalent binding[73;74] or electrostatic interactions[74]. Depending on the aim, direct or secondary labelling procedures might be used. An example for direct labelling in the context of cell isolation would be an antibody against a specific cell surface receptor attached to a magnetic particle. In the indirect case, a combination of a primary antibody and a secondary antibody attached to the magnetic particle would be used. Indirect labelling strategies have

the advantage that a range of different antibodies can be used to increase the specificity for the selected cell. This is particular useful when surface epitopes are not highly expressed. A direct method is usually faster and requires fewer antibodies. In the case of cell separation specificities of up to 99.9% and 3 log depletion efficiencies have been reported[75;76].

After the labelling step, entities of interest with an attached magnetic particle need to be separated from the media. This can be achieved in batch mode in the simplest case by the placement of a permanent magnet next to the tube. More sophisticated separation devices are available which use columns filled with soft magnetic spheres or steel wool and an external magnetic field to generate high field gradients[77]. Other high field gradient devices such as quadrupole and hexapole magnet configurations have been used as well[78]. Additionally continuous separation systems using fluidised bed designs and others have been reported[79].

Following the separation step, an additional step for the removal of the magnetic label might be necessary. This can be achieved for cells in simple cases via cultivation and the addition of media but might involve enzymatic cleavage of the label, active displacement of the label via competitive binding or ionic exchange. Cell viability is normally not negatively affected by magnetic separation techniques due to suitable pH values in the buffered separation media and the low magnitude of the forces used[61;73].

In general it can be said the magnetic separation is a highly versatile fast, efficient and simple separation method suitable for biomedical applications.

2.2.2 Magnetic drug and cell delivery

The increased understanding of human diseases and the development of drugs for their treatment has been the basis for the success of medicine in the 20th century. This is most evident in the field of infectious disease where small molecules globally administered eradicate microorganisms without side effects. However, most drugs do act on non-diseased cells in the body and cause unwanted side effects. For example cancer drugs aimed at fast growing cancer cells kill other fast growing cells such as haematopoietic cells, epithelia cells and hair follicle cells.

Research efforts are accordingly directed towards the development of targeted therapeutics[80]. Ideally, these therapeutics should only interact with pathological cells. One possibility to achieve that is the use of molecular recognition

via specific binding or the use of pro-drugs which are activated in a specific environment. Another possibility is the use of physical forces to spatially localise a drug. Magnetic delivery strategies are promising candidates for that, as magnetic fields can penetrate the human body without generating significant forces on normal cells.

The basic principle behind magnetic delivery strategies is to label drugs or cells with a magnetic entity, in order to make them responsive to a magnetic field, followed by the application of a magnetic field gradient to concentrate the drug or cell at the area of interest[41;81;82].

Accordingly the first step for magnetic drug or cell targeting is the magnetic labelling. Common requirements for these magnetic labels are superparamagnetic behaviour to avoid aggregation of particles which could cause embolisms, biodegradability, high saturation magnetisation, low toxicity and high reproducibility in all manufacturing stages.

Magnetic drug delivery adds additional requirements such as long blood half live time, no immunogenicity, functionalisation potential for drug attachment and controlled release or porosity if the drug is loaded via absorption[83]. Drug attachment to a magnetic particle has to be primarily concerned with the release kinetics and release mechanism. A whole range of release mechanisms from diffusion[84] to controlled release[85-87] are available. Magnetic particles are here mainly a carrier but their route of clearance, degradation and potential interference with the drug have to be addressed.

For cell labelling appropriate charges for attachment or specific receptor ligands for active uptake are necessary[88;89]. Small hydrodynamic diameters are generally favourable as they allow for higher iron concentration in cells due to more efficient uptake. Size is also an important determinant of the uptake route with particles <200 nm being internalised via pinocytosis while bigger ones have to be internalised actively via endocytosis[90]. As different cell types have different phagocytic potentials additional means to increase cellular uptake such as transfection agents[91;92], specific receptors ligands[93;94], serum starvation, electroporation[95] or magnetofection[96] (forcing particles into cells via magnetic field gradients) might be necessary. The primary aim for magnetic cell delivery is to deliver biologically active cells to a specific place. It is hence important that labelling does

not interfere with the therapeutic potential of cells. In particular cell growth, differentiation and migration potential should not be influenced negatively. Additionally increases in mutation rates due to particle breakdown products or increased inflammation have to be avoided.

The need for biodegradability has so far favoured iron oxide nanoparticles as the human body is able to degrade them and integrate the iron into the body iron pool[47;97;98]. Most studies have shown that iron oxide nanoparticles are well tolerated by cells below certain concentrations and do not negatively affect growth or differentiation potential[10;43;88;92;99-106]. Transient up-regulation of several hundreds of genes for up to two weeks following cell labelling with SPIONs has been reported[107]. There have also been reports indicating limited differentiation potential for some cells[104;108]. A potential mechanism for nanoparticle induced DNA damage has been reported, although not for iron oxide based nanoparticles[109]. There are no indications for long term health risks so far. Clinical studies with SPION labelled cells show that labelled cells are well tolerated without unwanted side effects[103;110;111]. However, the safety profile has to be assessed for each cell type and possibly even for each cell line separately.

Generating magnetic field gradients for the localisation of drugs and cells is the second step of magnetic targeting. A simple classification of different devices to generate field gradients is to divide them into three broad groups: permanent magnets, electromagnets and local flux concentrators.

Modern rear earth permanent magnets offer a high flux density without the need for power or cooling. The main disadvantage is the fast decay of the field strength with increasing distance to the surface. Another disadvantage might be the inability to dynamically change the field strength. These magnets can be used as simple blocks or more efficiently in arrangements which focus the magnetic field in a particular area such as Halbach arrangements[112]. Permanent magnets have been placed next to the body for magnetic drug and cell delivery in preclinical settings[15;84;105;113-119] and for magnetic drug delivery in a clinical trial[84]. Animal studies with surgically implanted permanent magnets have also been reported[120].

Electromagnets, mostly used with iron cores, offer the ability of dynamic field strength adjustments which can be used for dynamic control and active guidance. Their main disadvantages are substantial power and cooling requirements and similar

to permanent magnets, the fast decay of the field strength. Electromagnets have been used for clinical and preclinical drug targeting[121-124] and their potential for dynamic control and active guidance has been demonstrated[125]. A special subcategory in the group of electromagnets are superconductors. Superconductors offer high flux density which can't be achieved with electromagnets but don't normally allow for dynamic changes of their field strength. The potential application of superconductors for magnetic targeting has been illustrated by in vitro experiments[126;127]. MRI systems use a combination of a superconductor and electromagnets. This combination has some advantages for magnetic targeting which have recently been shown in in vitro and in vivo experiments[128-130].

In order to address the problem of the fast decay in magnetic field strength with increasing distances mentioned above, attempts have been made to use ferromagnetic objects to act as local flux concentrators. These flux concentrators need to be inserted into the body where they generate high field gradients locally when exposed to an external magnetic field. This enables the generation of sufficient forces for magnetic targeting at a depth in the body that would otherwise not be feasible. Experimental studies have shown the feasibility of this approach particular for applications where metal stents are used[106;128;131-133]. Such an approach could be used for magnetic drug and cell delivery for pathologies which require the deployment of stents. Experimental and theoretical work has been undertaken to extend this concept for guided delivery via the placement of needles next to blood vessel bifurcations to guide magnetic entities along or the used of use of shears as seed points to accumulate drugs[134-136].

Magnetic delivery strategies have demonstrated their potential in preclinical experiments for drug delivery[113;118;137], cell delivery[106;117;119], nucleic acid delivery[106;119;122;138], magnetofection[139;140], viral delivery and blocking of the blood supply to tumours[141]. Additionally their potential in combination with hyperthermia (see section 2.2.3) and MRI (see section 2.2.4) has been demonstrated. New possibilities for the molecular control of cellular mechanisms and advanced applications in tissue engineering are emerging[105;142;143] as well. However, their clinical success has so far been limited to MRI contrast agents and some early trails for drug delivery. One of the biggest problems already mentioned is the fast decline of magnetic force with increasing distances from their source. An additional limitation is the maximum flux density achievable in permanent and electromagnets

which make their translation from animal experiments to humans difficult. Theoretical modelling has been performed for some aspects of magnetic targeting[114;134;144-146]. However, a through theoretical basis addressing questions of suitable experimental designs which can be translated from animals to humans would be desirable. A first step towards that aim will be presented in chapter 6.

Potential clinical applications are also hampered by the lacking availability of clinical grade magnetic particles. Although magnetic particles have been used frequently for MRI, the production of these agents has been discontinued due to economic reasons. New SPION based contrast agents are currently in late clinical trials but they will only eliminate the problem partially. Particularly as requirements for MRI contrast agents are different from targeting or hyperthermia applications. Particles for research applications are available from several commercial companies but pharmaceutical companies have so far not invested in this area despite some commercial potential[147].

2.2.3 Magnetic hyperthermia

Magnetic hyperthermia refers to the use of magnetic particles in combination with alternating magnetic fields to induced localised heat formation. It has to be differentiated form thermal ablation where temperatures of > 50°C are used to destroy cells and tissues. Magnetic hyperthermia aims to achieve temperatures of >42°C to selectively damage cancer cells and induce apoptosis. Another application of magnetic hyperthermia is the controlled release of drugs.

Magnetic materials can generate heat via different mechanisms: Hysteresis loss, Neel relaxation and Brownian relaxation[41;148]. Hysteresis loss is loss of internal magnetic energy due magnetisation typical for ferromagnetic materials. Neel relaxation arises from the time delay between an alternating magnetic field (AMF) and the magnetisation in superparamagnetic particles. This delay can be described by a complex magnetic susceptibility with the power loss related to the imaginary part of it. Heat generation via Neel relaxation reaches a maximum for SPM particles at a particular frequency, which is dependent on particle characteristics such as crystal size. Brownian relaxation is heat energy dissipation due to particle rotation and collision in the suspension media. This is clearly viscosity dependent and diminishes for bound particles. The amount of energy produced by monodisperse SPM in an AMF can be described by the specific loss power as[41;148]

$$P = \chi_0 H_0^2 \mu_0 \pi \frac{2\pi f^2 \tau}{1+(2\pi f\tau)^2} \quad , \qquad \text{Eq. 2.15}$$

with χ_0 the dc magnetic susceptibility, H_0 the amplitude of the AMF, f its frequency and τ the relaxation time. The relaxation time is the combination of Neel (τ_N) and Brownian (τ_B) relaxation times:

$$\frac{1}{\tau} = \frac{1}{\tau_N} + \frac{1}{\tau_B} \quad , \qquad \text{Eq. 2.16}$$

with τ_B defined as

$$\tau_B = \frac{3\eta V_H}{k_B T} \quad , \qquad \text{Eq. 2.17}$$

and τ_N defined by

$$\tau_N = \frac{\sqrt{\pi}}{2} \tau_0 \frac{\exp(\frac{K V_M}{k_B T})}{\sqrt{\frac{K V_M}{k_B T}}} \quad , \qquad \text{Eq. 2.18}$$

with η the viscosity of the fluid, V_H the hydrodynamic particle volume, k_B Boltzmann's constant, T absolute temperature, τ_0 = 10^{-9} s, K the anisotropy constant and V_M the magnetic volume.

The specific power loss increases with the frequency of the AMF (until the maximum for a particular SPM particle system is reached) and the amplitude of the field. However, alternating magnetic fields lead to eddy current induction that can lead to unwanted surface heating and peripheral nerve stimulation. Experimental studies indicate that the limit for $H_0 \cdot f$ might be around 5x10^8 $Am^{-1}s^{-1}$ [149].

Iron oxide based SPM particles have been used most frequently for magnetic hyperthermia[150-154] but cobalt based particles[155] with higher saturation magnetisation and ferromagnetic particles have been used as well. But the toxicity of other elements like cobalt might limit their potential applicability[156;157].

Experimental results particular in animal models of cancer indicate the biggest hurdle for its application is the insufficient temperature increase. Major factors limiting the local heating capabilities are the amplitude of the AMF, the nature of particles, particle concentration, heat dissipation in the tissue and cooling via blood. Achieving high particle concentrations is particular difficult if particles are administered systemically via intravenous injection. Although preferable from a conceptual and practical point of view as it would allow targeting of metastasis

elsewhere in the body, non-specific accumulation in organs of the reticular endothelial system is a problem even for particles with molecular recognition moieties[158-160]. Direct injection of particles into the centre of a tumour might be feasible but it is difficult to achieve a uniform distribution within the tumour. The outer rim of the tumour is frequently well vascularised[161;162] providing an effective heat sink in the regions where tumour stem cells[163] may reside. This makes killing them particular difficult. Other open questions for the application of magnetic hyperthermia for tumour treatment are questions of optimum duration and treatment interval[164-166].

Many researchers acknowledge the limitations of hyperthermia as a single treatment strategy for cancer and are hence investigating combination treatments with radiation[167], chemotherapy[168] and others.

Magnetic hyperthermia offers other interesting applications in medicine particular in the field of controlled drug release. This includes the use for cancer therapies but offers options for other therapies as well. Of particular interest for such applications are magneto-liposomes[85;169;170]. Liposomes are spheres made form phospholipids with an aqueous or gaseous core whereby the melting temperature of the phospholipid membrane is determined via its composition. The core of liposomes can be loaded with a drug and magnetic particles. Magnetic particles can also be attached to the phospholipid membrane. Molecular recognition elements such as antibodies and organic molecules can be attached to the liposome surface to increase targeting specificity. Depending on the magnetic moment of these liposomes magnetic targeting strategies via the use of magnetic field gradients might be used to further increase the concentration of them at the site of interest. After the target regions have been reached an AMF can be used to release the drug on demand. Magnetic hyperthermia can be used for the controlled release from other magneto responsive materials too[86;87].

2.2.4 Magnetic cell tracking

Cellular therapies offer new therapeutic opportunities. However, to get a better understanding of cell based therapies non-invasive imaging methods will be needed. This will allow researchers to address questions such as have the cells been delivered to the area of interest, are cells migrating to other places, what is the best delivery route, do cells functionally integrate into pathological tissues? Potential imaging modalities to address these questions are MRI[92;103;110;111;171], SPECT[172;173],

PET[174-176] and in the preclinical setting bioluminescence[177-179] and near infrared imaging[180-182].

Magnetic resonance imaging is particular suitable for cell tracking in the context of magnetic cell delivery, as cells are already labelled with magnetic particles which allow tracking on MR images. Additional advantages of MR imaging are the high soft tissue contrast, the ability to acquire additional information via functional imaging and the fact that no radiation is needed. The availability of MRI in clinical and preclinical settings allows for transferability of experimental protocols.

The detection of labelled cells on MR images relies on the change of relaxation parameters due to the magnetic moments of labelled cells, in particular a strong reduction in the spin-spin relaxation times, T_2 and T_2*[183-185]. A detailed explanation of MRI can be found in section 3, while aspects of cell labelling are explained in section 2.2.2. Furthermore examples for cell MR based cell tracking can be found in chapter 7. Shortening of T_2 and T_2* relaxation rates leads to hypointesity on T_2 and T_2* weighted spin- and gradient-echo images. Hence labelled cells appear as dark regions on such images.

MR imaging has been used in preclinical animal models to track cells injected into the myocardium after an infarct over time[10;186-188] and to evaluate host graft rejection of transplanted organs[189-191]. These studies showed the feasibility of cell tracking without negative effects on cell differentiation[88;99;107;108]. However, following cell delivery, it has been observed that hypointensity losses are slower than the loss of injected cells over time. This indicates that iron oxide remains at the site of injection after cells have died[102;186]. There is good evidence that macrophages take up magnetic particles from dead cells, which can lead to false positive signals[192-194]. Experimental studies suggested that the differentiation between live and dead necrotic cells containing iron oxide might be possible by combining T_2 and T_2* imaging[195]. Although this might help for certain cases it want be effective if the particles are rapidly internalised by macrophages. Tracking of magnetically labelled cells has been performed successfully in clinical studies[103;110;111] illustrating the translation potential. But images have to be analysed with care.

Magnetic resonance imaging has been frequently employed for cell tracking in the brain in pre-clinical and clinical settings[43;101;103]. MR based cell tracking in the brain has proven particular useful as it is currently the only technique which allows

long-term tracking. The limitations mentioned above apply for the brain as well. Stereotactic injection of labelled cells into the brain leads frequently to local haemorrhage formation in the area and along the injection canal[101;196;197]. This causes the formation of iron rich blood breakdown products such as hemosiderin which is difficult to distinguish form labelled cells. Nevertheless, magnetic cell tracking in the brain is frequently used and allows for the detection of single cells in high field pre-clinical scanners[198].

The clinical application of MR based magnetic cell tracking has demonstrated the safety of this technique as no negative side effects due to cell labelling have been reported. Cells seem to tolerate biodegradable iron oxide particles fairly well with almost no change in growth and differentiation potential (see section 2.2.2). However the major limitations of negative contrast (hypointensity), macrophage uptake of free label, label independence of cell status as well as label dilution and degradation by growing cells are significant[183;185;199]. Image hypointensity is particularly problematic for cell tracking in regions which show natural hypointensity such as tumours, abdominal regions and the lung. New developments in the use of ultra fast imaging sequences[200-203] as well as susceptibility gradient weighted reconstruction[204] might bring improvements in these areas. Label independence of cell status refers to the fact that MRI cannot be used to distinguish between live and dead cells or between differentiated and undifferentiated states. MR sensitive gene expression markers such as ferritin[205;206], lysine rich proteins[207;208] and others[209;210] are currently under development to address this issue. However, these techniques are not compatible with strong magnetic moments in cells. In order to assess the status of cells in the context of magnetic cell delivery additional imaging modalities are necessary. There are several expression vectors available for SPECT and PET imaging[211-213] which can be used to gain more information of the cell status. Attempts are under way to combine these imaging modalities in order to get high spatial resolution and soft tissue contrast from MRI and high specificity and the ability to detect molecular expression via SPECT or PET[214-216].

3 Magnetic resonance imaging

As indicated in chapters one and two cellular therapies would benefit from an increased understanding of the cell behaviour after delivery *in vivo*. MRI is particular suitable for that due to its non-reliance on radioactive tracers, high soft tissue contrast, clinical availability and the contrast from iron oxide particles used for magnetic delivery. The basic principles of MRI will be outlined in this Chapter. This will be followed by mentioning essential components of a magnetic resonance imaging system and their functions. Finally, some additional considerations for magnetic resonance based cell tracking will be given.

3.1 Basic principles

Magnetic resonance imaging (MRI) is based on the nuclear magnetic resonance phenomenon which was discovered in 1946 by Bloch and Purcell. They discovered that different atomic nuclei placed in a magnetic field absorb radio frequency (RF) energy at different frequencies, their respective resonance frequency.

MRI exploits quantum mechanical principles of atomic nuclei to generate images. Atomic nuclei have an angular moment $\boldsymbol{J}$ given as

$$\boldsymbol{J} = \hbar \boldsymbol{I} \quad , \qquad \text{Eq. 2.19}$$

where $\boldsymbol{I}$ is the spin of the nucleus. Nuclei with an odd number of protons or an even number of protons but an odd number of neutrons have a net magnetic moment:

$$\boldsymbol{\mu} = \gamma \boldsymbol{J} \quad , \qquad \text{Eq. 2.20}$$

with γ the gyromagentic ratio, a constant for a particular nuclei. Nuclei which do not have a net magnetic moment cannot be observed with MRI. Hydrogen has a high abundance in biological tissues and a high gyromagnetic ratio which makes it the primary nuclei observed in MRI. Protons undergo a Zeeman splitting into two energy levels when placed into a magnetic field B_0, with an energy difference of

$$\Delta E = \hbar \gamma B_0 \quad . \qquad \text{Eq. 2.21}$$

The two energy levels are aligned parallel or anti-parallel to the main field B_0 with populations of protons N following a Boltzmann distribution:

$$\mathrm{N_p}/N_a = e^{-\frac{\Delta E}{k_B T}} \quad , \qquad \text{Eq. 2.22}$$

with k_B the Boltzmann constant and the absolute temperature T.

The excitation of a proton from the low to the high energy state requires photons with the energy of ΔE (see Eq. 2.21), at a particular frequency, the Larmor frequency:

$$\nu_0 = \frac{\gamma B_0}{2\pi} \quad . \qquad \text{Eq. 2.23}$$

The magnetic moment of a proton ensemble can be described in classical terms. The nuclear magnetisation of the protons ($\boldsymbol{M}$) placed in a magnetic field is experiencing a torque (Eq. 2.11) and start to precess around B_0 at the Larmor frequency following

$$\frac{\mathrm{d}\mathbf{M}}{\mathrm{dt}} = \gamma \boldsymbol{M} \times \boldsymbol{B} \quad . \qquad \text{Eq. 2.24}$$

For an ensemble of protons at equilibrium, the difference between parallel and anti-parallel aligned protons is small. However, the application of a magnetic field perpendicular to B_0 oscillating at the Larmor frequency rotates the magnetisation vector of the assembly into the X-Y plane. In MRI systems the Z axis is aligned with B_0 (see Figure 2). The precession of the magnetisation in the X-Y plane can be detected via the induced current in a coil tuned to the Larmor frequency, the receiver coil. Once the magnetisation has been tilted away from the equilibrium i.e. by 90 degree into the X-Y plane, it will return to the equilibrium via the spin-lattice relaxation. The spin-lattice relaxation is the recovery of the Z component of the magnetisation vector as the system returns to reach its original magnetisation (M_0) given by

$$\mathrm{M_z}(t) = M_0\left(1 - exp\left(\frac{-t}{T_1}\right)\right) \quad , \qquad \text{Eq. 2.25}$$

with T_1 the spin-lattice relaxation time (This follows from the Bloch equations for a 90 degree RF pulse).

As the magnetic moment is tipped into the X-Y plane it will rotate around Z at the Larmor frequency. It is hence convenient to define a reference coordinate system (X'-Y'-Z) which rotates at the Larmor frequency around Z. In the X'-Y'-Z coordinate system, the transverse magnetisation is decaying from its maximum (M_0 , for a perfect 90 degree excitation) to zero. The transverse relaxation time T_2 specifies the mono-exponential decay of transverse magnetisation:

$$\mathrm{M_{X'Y'}}(t) = M_0 exp\left(\frac{-t}{T_2}\right) \quad . \qquad \text{Eq. 2.26}$$

T_2 decay is caused by magnetic interactions between spins which leads to loss of phase coherence. However, inhomogeneities in the B_0 field lead to increased decay rates. For gradient echo, the observed relaxation rate (T_2*) can be described as the combination of relaxation due to both non-recoverable (T_2) spin-spin and recoverable relaxation due to field inhomogeneities (T_{2i}):

$$\frac{1}{T_2^*} = \frac{1}{T_2} + \frac{1}{T_{2i}} \quad , \qquad \text{Eq. 2.27}$$

MRI exploits inherent relaxation time differences as well as differences in proton densities to generate image contrast. This is achieved by the use of different imaging sequences. Imaging sequences are timing protocols for the application of magnetic field gradients, RF pulses and signal recording.

Spatial localisation of MR signals is necessary to generate an image. The imaging technique MRI which allows that was developed independently by Mansfield and Lauterbur in 1973. This is achieved via slice selection, frequency encoding and phase encoding. As mentioned above the excitation of spins requires the application of an RF pulse at the Larmor frequency. The Larmor frequency is linearly dependent on the magnetic field strength. A combination of a particular shaped RF pulse (e.g. sinc or gaussian) with a linear field gradient can be used to limit the excitation of spins to a thin slab. Frequency and phase encoding are used for the spatial localisation of the signal to a single voxel of this slab. If a linear magnetic field gradient is applied at the time of the signal acquisition (during readout) along one axis, excited spins will possess a linear frequency dependence along that axis. For the orthogonal axis phase encoding is used. For that, a linear field gradient is applied before the readout starts. This leads to a phase difference in the rotating spins which is dependent on their position along the axis of the applied phase-encode gradient. The process is repeated with varying gradient strengths (or moments) in order to fill up a raw data matrix (in time-domain), known as k-space. Once the matrix has been filled a Fourier transformation (FT) can be performed to generate an image (frequency domain data).

The two simplest imaging sequences for MRI are the gradient echo and the spin echo sequence. Sequence diagrams for both of these imaging sequences are shown in Figure 1.

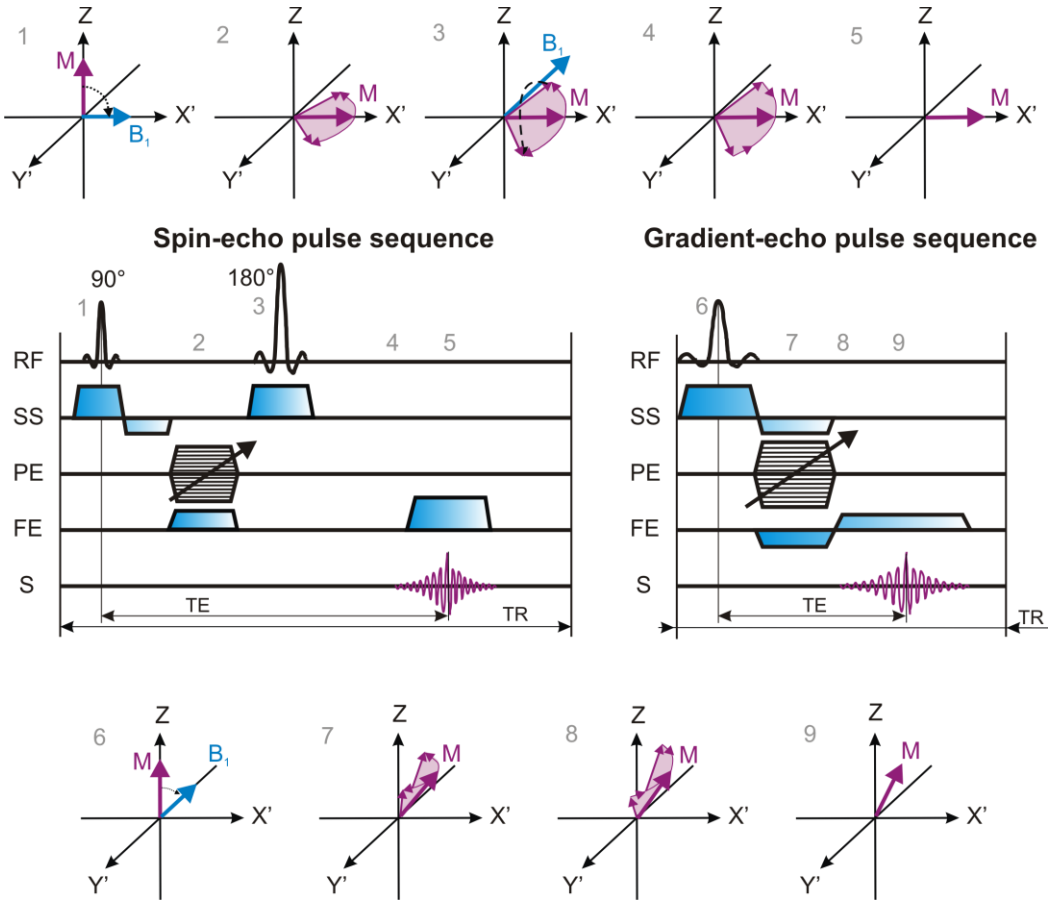

Figure 1 Spin echo and gradient echo imaging sequence. The first row gives a simplified graphical representation of the magnetisation vector (M) during the spin echo sequence in a rotating reference coordinate system. Appling a 90° RF pulse rotates the magnetisation vector into the transverse plane (X'-Y' plane) (1). After that, de-phasing of the magnetisation vector starts (2). The 180° pulse rotates the M-vector around (y normally) the x-axis (3). This reverses the de-phasing direction (4) and causes the echo to build up via re-phasing (5). T_1 decay would normally decrease the tip angle and bring the M-vector towards the z axis. This has been neglected for the images 1-9. The row below the pulse sequences shows effects of the gradient echo sequence on the M-vector. A RF pulse < 90° is applied (6). This tips the M-vector accordingly towards the X'-Y' plane. The phase encoding gradient is applied together with a reversed frequency encode gradient to induce de-phasing in the X'-Y' plane (7). Switching of the FE gradient into the opposite direction induces re-phasing (8) and hence induces the gradient echo signal (9) when the M-vector regains coherence. M: magnetisation vector, B_1: applied field induced by RF pulse, RF: radio frequency, SS: slice selection, PE: phase encoding, FE: frequency encoding, S: signal, TE: time until echo, TR: repetition time.

A pulse sequence diagram for a spin echo sequence is displayed on the left side of Figure 1 with a depiction of the magnetisation vector of a voxel in the top row. This depiction corresponds to an axial slice where SS=Z, PE=X and FE=Y. For simplicity reasons T_1 decay has been neglected in Figure 1. A 90° RF pulse is applied at the same time as the slice section gradient (SS) to excite an imaging slab. This rotates the magnetisation vector into the X'-Y' plane. Following slice selection, a phase encoding gradient is applied along the phase encode direction (PE). During that an additional gradient is applied along the frequency encode direction (FE) which de-phases spins aligning the start of the echo with edge of k-space. After de-phasing due to T_2 decay has occurred for half of the echo time (TE/2), a slice selective 180° RF pulse is applied together with a slice selection gradient to refocus the spins (e.g. flip the magnetisation along the X axis). This causes the spins to re-phase and to generate the spin echo. A frequency encode gradient is applied during the acquisition of the echo. The time needed for the execution of all of these steps, the time between two excitations is the repletion time TR. PE gradients are applied in a stepped fashion increasing from minus PE max to plus PE max with one PE step for each line of k-space. A spin echo sequence will lead to signal intensity S for one voxel following:

$$S = k\rho_P \left(1 - e^{-\frac{TR}{T_1}}\right) e^{-\frac{TE}{T_2}} \quad , \qquad \text{Eq. 2.28}$$

with a field strength and nuclei specific constant k and the density of the imaged nuclei, i.e. proton density ρ_P. The product of these two constants is proportional to M_0 in equations 2.24 and 2.25.

A gradient echo sequence diagram is shown on the right side of Figure 1 with a depiction of the magnetisation vector for one imaging voxel below. A slice selective RF pulse is applied together with a slice selection gradient. This tilts the magnetisation vector away from Z into the X'-Y' plane. The angle between Z and M is called the flip angle which is typically < 90°. A negative lob of the SS gradient is used to re-phase spins which were de-phased during slice section. Phase encoding is performed along one of the two remaining axis via the application of a phase encode gradient. As mentioned above phase encode gradients are increased stepwise at each TR for each k-space line. A gradient echo is generated after the application of a positive gradient which causes re-phasing of spins. This gradient echo occurs when the positive gradient moment (gradient amplitude * application time) is equal to the negative moment. The signal equation for gradient echo sequences is similar to the spin echo equation with

two differences: T_2* replaces T_2 as de-phasing due to field inhomogeneities are not re-phased (see equation 2.26) and typically a less than 90° flip angle will be used α :

$$S = k\rho_P \left(\sin\alpha \; e^{-\frac{TE}{T_2^*}}\right) \frac{\left(1-e^{-\frac{TR}{T_1}}\right)}{\left(1-\cos\alpha \, e^{-\frac{TR}{T_1}}\right)} \quad . \qquad \text{Eq. 2.29}$$

Image contrast on spin echo images can be influenced via the appropriate selection of TR and TE. For gradient echo images suitable TR, TE and flip angles need to be selected. However, if this intrinsic contrast is insufficient contrast agents can be used. Contrast agents are classified as T_1 or T_2/T_2* contrast agent depending on the relaxation mechanism they primarily influence. The most frequently used T_1 contrast agents are the paramagnetic ions gadolinium and manganese. They reduce spin-lattice relaxation times via chemical exchange between water molecules surrounding the ion and bulk water molecules. Superparamagnetic iron oxide particles (SPION) are the main T_2/T_2* contrast agents. The spin-spin relaxation time is reduced due to the magnetic field inhomogeneities produced by SPION.

3.2 Basic components of an MRI scanner

Modern MRI scanners consist of a superconducting magnet in a cryostat, gradient coils, radio frequency transmitter and receiver and a computer. These components are illustrated below. The function of individual components will be explained briefly in the following section.

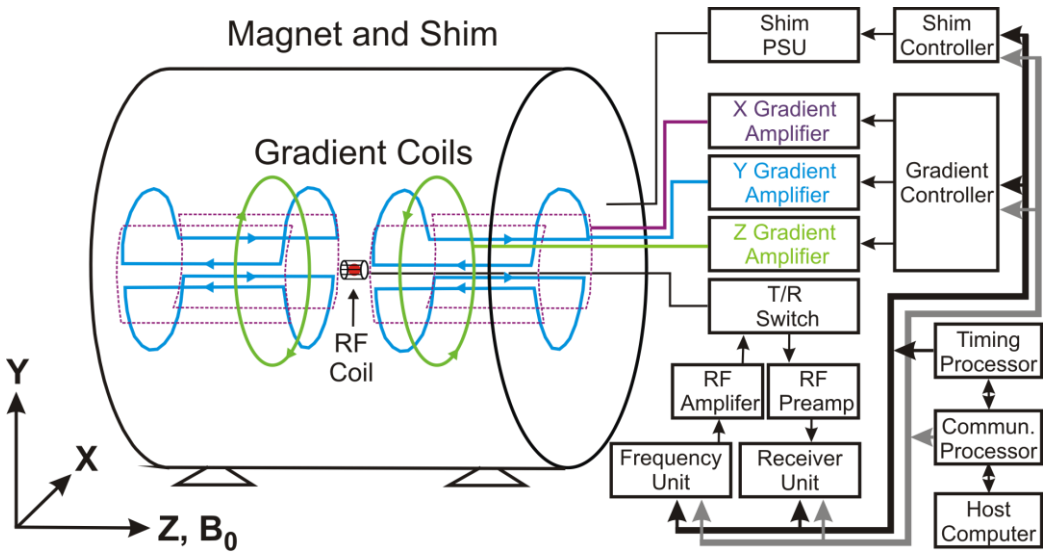

Figure 2: Schematic of an MRI scanner. The superconducting magnet and permanent shims are indicated by the outer cylinder. Gradient coils consist of two Golay coils for X and Y gradients and a Maxwell pair for Z gradients. Resistive shim coils are not drawn on the picture although their shim power supply unit (PSU) and control is indicated. A host computer provides an interface to prepare imaging sequences. Commands are sent via the communications processor to subunits. The gradient controller produces a gradient waveform which is amplified by gradient amplifiers. The frequency unit produces radio frequency waveforms which are amplified by the RF amplifier. An RF coil picks up induced currents from exited spins in the specimen (red sphere) which are amplified by the Preamps and digitised in the Receiver unit. The timing processer ensures accurate timing and synchronisation of all sub systems. Following the standard convention the positive Z axis points to the front of the scanner (right side of the image) with B0 parallel to Z. T/R: transmit/receive, commun.: communication

The purpose of the magnet is to provide a very homogeneous magnetic field to align the sample spins (spins in the context of MRI refer to proton spins of imaging nuclei, mainly hydrogen). As outlined in the previous chapter the precession frequency, the Larmor frequency is dependent on the magnetic field strength. This sets high uniformity requirements for the magnet (< 5 ppm). Typical field strengths of modern superconducting MRI magnets are 1.5-3 T clinically up to 9.4 T for research systems and up to 21 T for preclinical scanners. These superconductors (NbTi) are maintained in liquid Helium in a cryostat.

Gradient coils are resistive coils in the bore of the main magnet which generate linear magnetic field gradients over a central spherical space, the imaging sphere. A Maxwell pair is used to generate a liner gradient along the Z axis while Golay coils are used for linear gradients along X and Y. Golay coils for X are rotated by 90 degrees around Z with respect to Y.

A radio frequency coil is placed in the centre of the gradient coils and main magnet. Specimens are placed in the centre of volume coils as shown in Figure 2 or next to surface coils. RF coils are used for two purposes; first to transmit a RF wave to generate a rotating B_1 field and secondly to pick up induced currents from excited spins (the rotation of their nuclear magnetic moment in the X-Y plane).

Additional electronic components are needed for the control of an MRI scanner. A host computer is used as a user interface to select a particular imaging sequence and set imaging parameters. Appropriate commands are sent to subsystems via the communications processor. For example at the start of an imaging session the shim controller is used to set currents for active shim coils which are produced by the shim power supply unit (PSU). The execution of an imaging sequence typically requires the application of a particular RF wave and controlled field gradients. RF waves produced in the RF waveform generator (RF frequency unit) are amplified by the RF amplifier and sent to the RF coil via a transmit/receive switch. Gradient commands from the communications processor will be translated into particular gradient waveform, amplified and applied to the gradient coils. A certain time after the application of the RF excitation, the induced current in the RF coil will be amplified by the RF pre-amplifier and converted into a digital signal in the receiver unit. All of the above steps have to be performed at precise time points which are controlled via the timing processor. Digital time domain data is sent to an image processor which performs a Fourier transformation to generate an image.

3.3 Magnetic resonance imaging in the context of magnetic particles

The use of MRI for cell tracking has been discussed in section 2.2.4 this section will hence only briefly discuss the use of superparamagnetic iron oxide particles (SPION) as a T_2/T_2* contrast agent for other application.

The FDA approved the use of SPION for the detection of liver or spleen metastasis, magnetic resonance angiography and perfusion imaging[217]. However, the production of these contrast agents has been discontinued as they did not prove economically viable. There are new contrast agents currently in clinical trials aiming for the above mentioned applications (Supravist, Schering AG, Germany; Combidex, Advanced Magnetics Inc, MA).

Although there are interesting applications for these ferrofluids, the development of targeted contrast agents (molecular recognition) will open a new

range of applications. Preclinical studies have shown the potential of antibody conjugated SPION for cancer staging[218;219], assessment of inflammation in the brain[220;221], organ rejection[189;190], atherosclerotic plaque staging[222;223] and others. These contrast agents or molecular imaging agents will extend the MRI applications of SPION.

4 Delivery of magnetically labelled cells using an MRI scanner

As outlined in chapter two, magnetic targeting applications can be classified depending on the origin of the magnetic field gradient used leading to three major groups: permanent magnets, electromagnets and flux concentrators. An MRI scanner is essentially an arrangement of different electromagnets with amplifies and control modules. This chapter focuses on attempts to use the gradient coils of an MRI scanner for the steering of magnetically labelled cells.

4.1 Introduction

The success of cell therapies depends partially on the ability to deliver the cells to the site of injury. Targeted magnetic cell delivery is an emergent technique for localised cell transplantation therapy. The use of permanent magnets limits such a treatment to organs close to the body surface or an implanted magnetic source[113;117-119;146;224;225]. One method which has recently attracted attention is the use of magnetic resonance imaging (MRI) systems to steer ferromagnetic objects deep inside the body[128-130;226].

This is particularly appealing due to the high magnetic field strength, and the precise spatial and temporal control over magnetic field gradients provided by an MRI system. Combining this functionality with the conventional MRI use to generate high contrast soft tissue images may allow for interactive real time feedback for the spatial position of the cells, or at least immediate confirmation of targeting success, as these cells appear hypointense or dark on MR images. Although the use of a magnetic resonance system for targeting has been investigated for ferrofluids[128] and micro-particle delivery[129;130], it has not been attempted in the context of cell delivery.

The aim of this study was to investigate the feasibility of using a magnetic resonance scanner for targeting (MRT) to guide cells within a bifurcating vascular system. In particular, single bifurcation targeting efficiency was estimated, as this could be applied in a consecutive fashion at several branches directing a bolus of cells to a small region within the vascular network. In addition, the feasibility of an MRI system to visualise the effect of the targeting gradients on the cell distribution was investigated, as this would enable visualisation of cell distribution or the possible implementation of interactive control.

The hypotheses for these experiments were:

- MRI gradient coils can be used to steer magnetically labelled cells in a flow phantom.
- The difference in cell distribution due to magnetic steering can be detected via MRI.

4.2 Materials and Methods

4.2.1 Cell culture and cell labelling

Human mononuclear cells (MNCs) were collected by leukapheresis from peripheral blood of G-CSF-stimulated donors following the protocol approved by the department of health and the UCL ethics committee. Cells were washed twice with phosphate buffered saline (PBS), centrifuged for 10 min at 400 g, plated in Dulbecco's Modified Eagle Medium (DMEM) (Gibco, UK) and incubated at 37 °C and 5% CO_2 for 2 hours. After two hours non-adherent cells were washed away and the media replaced with fresh DMEM + 10% fetal bovine serum (FBS) (Invitrogen, UK). Mesenchymal stem cells were obtained from Tulane University, New Orleans, USA, and cultivated in α-MEM supplemented with 16% FBS (all Invitrogen, UK) at 37 °C and 5% CO_2.

Labelling experiments were conducted when 80% confluence was reached. For MNC labelling either 45 µL Endorem, or 50 µL BioMag solution (particles washed 3 times with fresh media) or 5 µL fluidMAG were added per mL culture media, and cells were cultivated for 24 h. Cells were detached with Trypsin-EDTA (0.25% in Hank's Buffered Salt Solution HBSS, Sigma Aldrich Ltd., England) and washed 3 times with PBS. Cell concentrations were estimated with a haemocytometer. MSCs were labelled for 24 hours by adding 5 µL fluidMAG solution per mL medium. After that cells were detached with Trypsin-EDTA and washed 6 times with PBS. MNCs and MSCs were re-suspended to $3x10^6$ cells per ml in PBS containing 5% serum for targeting experiments. Cell viability after labelling was assessed via trypan blue exclusion (Invitrogen, UK).

4.2.2 Cell viability

For the cell viability assay, 5000 MNCs were seeded per well into a 96-well plate. The plate was incubated at 37 °C and 5% CO_2. After two hours, media was replaced with fresh media containing varying amounts of the different SPION and incubated for 24 hours. The media was removed, the cells were washed once with 200 µL media per well, 200 µL fresh media + 20 µL MTS tetrazolium compound solution (CellTiter 96® Non-Radioactive Cell Proliferation Assay, Promega, UK) were added. Following 4 hours incubation the absorption for each well at 490 nm and 690 nm was measured with a micro-plate reader (Tecan, Switzerland). Three wells were measured for each concentration per plate with three replications for the plate.

4.2.3 Quantification of cell labelling

A series of dilutions of Endorem, fluidMAG and BioMag particles in water was prepared (120, 60, 30, 15, 7.5, 3.75, 1.88, 0.94 µg iron per mL). For each concentration, two 250 µL tubes (Eppendorf, Germany) were filled with 120 µL of diluted particle suspension and 120 µL of 2% low melting point agarose (Sigma-Aldrich, UK). These tubes were submerged in Fomblin® perfluoropolyether PFPE (Solvay Solexis, Italy). Imaging was performed using a 9.4T VNMRS horizontal bore scanner (Varian Inc., Palo Alto, CA) with a shielded gradient system (400 mT/m). A series of T_2-weighted images was acquired with a spin-echo sequence and the following parameters: TE 4.5-110 ms (18 steps exponentially distributed), TR 10 s, FOV 60x40 mm, slice thickness 1 mm, matrix 512x256.

Labelled cells were counted with a haemocytometer and diluted to $1x10^6$, $5x10^5$, $1x10^5$, $5x10^4$ and $1x10^4$ cells per mL in PBS. For each concentration, two 250 µL tubes were filled with 120 µL of diluted cell suspension and 120 µL of 2% low melting point agarose. T_2-weighted images were acquired using the same parameters as above.

The mean segmented signal intensity value was fitted to the spin echo signal equation (Eq. 2.28) using Matlab (MathWorks, Natick, MA) to estimate their T_2 values. A linear regression for $1/T_2$ (R_2) versus iron concentration was performed for the dilution series using the R software.

4.2.4 MRT of cells

A custom vascular bifurcation model was designed and manufactured from polycarbonate (AG prototypes, UK). The phantom consists of a cylindrical pipe with an internal diameter of 0.8mm and a 30° bifurcation (see Figure 3). The phantom was connected to an infusion pump (PHP2000 Harvard Instruments, UK) and placed into the centre of a 9.4 T MRI scanner (VNMRS, Varian Inc. Palo Alto, CA) equipped with a 60 mm bore size gradient set (rise time 5 T m^{-1} ms^{-1}, max. gradient strength 1 T/m).

The flow direction of the phantom was parallel to B_0 (Z). Cell suspension samples (0.8 mL of $3x10^6$ cells/mL) were infused at flow rates of 0.06 mL/min to 1.8 mL/min, leading to a mean velocity of 0.2 cm/s to 6 cm/s assuming parabolic laminar flow. During the infusion, gradients (amplitude + or -500 mT/m) were applied in the X

direction, perpendicular to the direction of flow. Due to hardware limitations the gradients were pulsed (2 ms on, 7 ms off using max. slew rate).

Cell suspensions leaving each bifurcation outlet tube (volume 0.4 mL each) were collected and cell concentrations were estimated using a haemocytometer. This was repeated three times for each gradient direction, labelling type and flow velocity.

In order to visualise the cell distribution with MRI, the flow was stopped and gradient echo images were acquired using a 3 cm surface coil (Varian Inc. Palo Alto, CA) with the following parameters; TE 1.24 ms, TR 100 ms, FA 30°, field of view 50x30 mm, matrix 192x128, NSA 50.

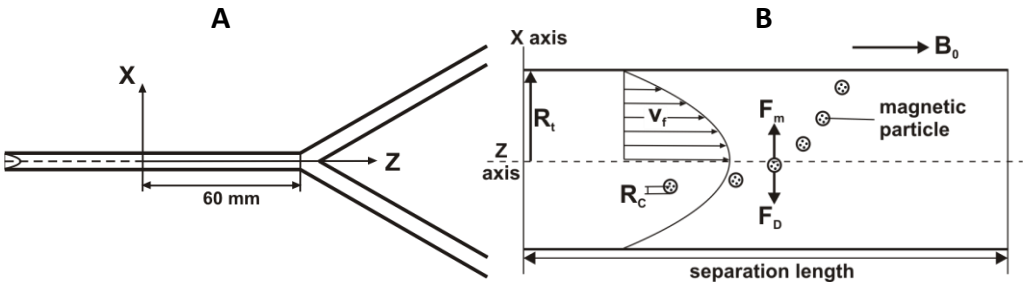

Figure 3: (A) Schematic drawing of the vascular bifurcation phantom: The tube diameter for this bifurcation is 0.8mm and the bifurcation angle 30°. The Z axis of the phantom is aligned with B_0 of the scanner. (B) shows the separation segment outlined in (A) with schematic representations of the flow profile and cells containing superparamagnetic iron oxide particles. The succession of a cell (shears) with internalised iron oxide particles (black dots) is a representation of the movement as one is attracted to the positive X axis due to the magnetic force acting on them.

4.3 Results

Figure 4 demonstrates the effect of incubation with different iron oxide concentrations on MNC viability for a 24 hour labelling period. No significant differences were found for the effect of Endorem and fluidMAG on cell viability, which reflects their comparable characteristics (diameter: 80-150 nm vs. 200 nm, dextran vs. starch coating). However, the labelling with BioMag particles resulted in a statistically significant decline in cell viability. This is most likely attributable to the size of these particles (diameter: 1.5 μm). For the purpose of this study, iron oxide concentrations that preserved at least 90% cell viability (Figure 4) were selected, as a compromise between iron labelling and number of available viable cells.

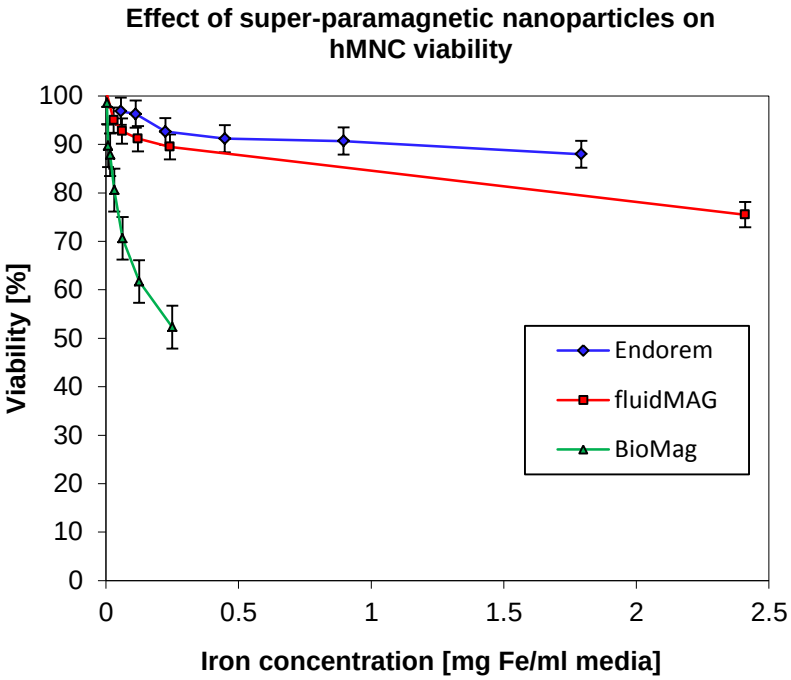

Figure 4: Effect of concentration of iron oxide in the culture media on cell viability. Nominal particle diameter for the super paramagnetic iron oxide particles are: Endorem 80-150 nm, fluidMAG NC/D 200 nm, BioMag 1.5 µm. Viability on the y-axis refers to metabolic activity normalised to unlabelled control cells. Diamond, squares, triangles: mean ± standard deviation (n=3x3 for each data point)

Iron oxide particles cause a signal loss on an MRI image that is dependent on the iron concentration and imaging parameters (see section 3.1). In order to estimate the internalised iron concentration a dilution series for each particle type and estimated MRI R_2 values (see Figure 5D). All three particle types showed a strongly linear correspondence to R_2 (R^2 0.993 - 0.998). Using these relationships, the amount of internalised iron for labelled MNCs was estimated to be 14 ± 7 pg/cell for Endorem, 68 ± 5 pg/cell for fluidMAG, and 292 ± 17 pg/cell for BioMag. In addition we have assessed fluidMAG labelled MSCs (225 ± 30 pg/cell), as these cells have recently been suggested as a possible lung cancer therapy.

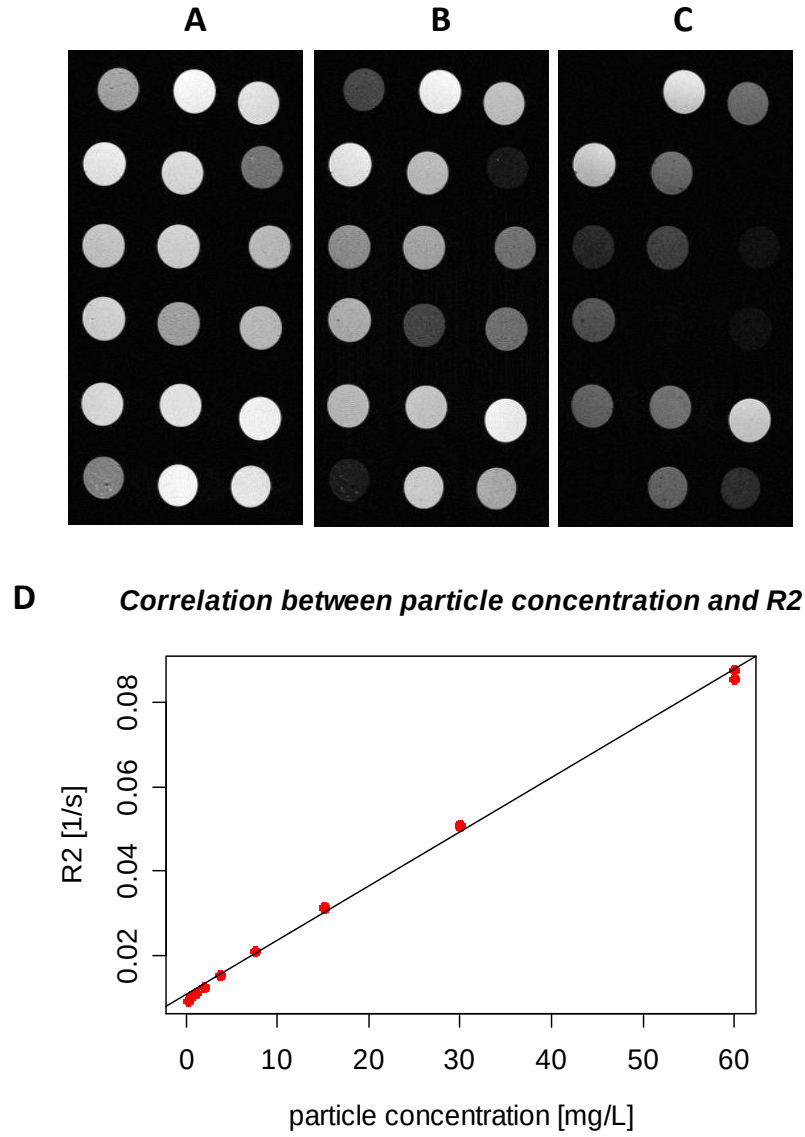

Figure 5: Example images of the T2 phantom, containing 18 Eppendorf tubes with different concentrations of iron oxide, randomly distributed in the phantom. Different iron concentrations led to signal intensities which are exponentially dependent on the echo time of the MRI sequence. Echo times are: 7.2 ms (A), 25 ms (B) and 84 ms (C). A series of such images is the basis for the linear regression. An example for such a regression of R_2 versus particle concentration for BioMag particles is shown in (D) (adjusted R^2 0.998).

To investigate the feasibility of MRT of cells, a small artery flow phantom was placed into the centre of our MRI system and connected to an infusion pump. A positive or negative magnetic field gradient (± 0.5 T/m) was applied along the X axis (see Figure 6), while cell suspensions were infused through the bifurcation. Figure 6 displays the targeting of cells labelled with BioMag particles at 1cm/s fluid velocity. With these settings, 75% of all cells were directed into one branch of the vascular bifurcation model. Furthermore, a positive and negative field gradient attracted the cells toward the left or right branch respectively. The term 'targeting efficiency' for this

and the next chapter is defined as the percentage of cells removed from exit tube A to exit tube B, where B is the targeted exit tube. In the aforementioned example the targeting efficiency was thus 50%.

The targeting efficiency of cell suspensions labelled with the three different iron oxide particles was investigated for a range of flow rates (0.2 – 6 cm/s, see Figure 7). Increased flow rates led to a decrease in targeting efficiency (e.g. MNCs labelled with BioMag; targeting efficiency 49%, 31%, 13%, 0.5% for 1, 2, 4 and 6 cm/s fluid velocity, respectively) as the magnetic force had less time to deflect cells before they reached the bifurcation point.

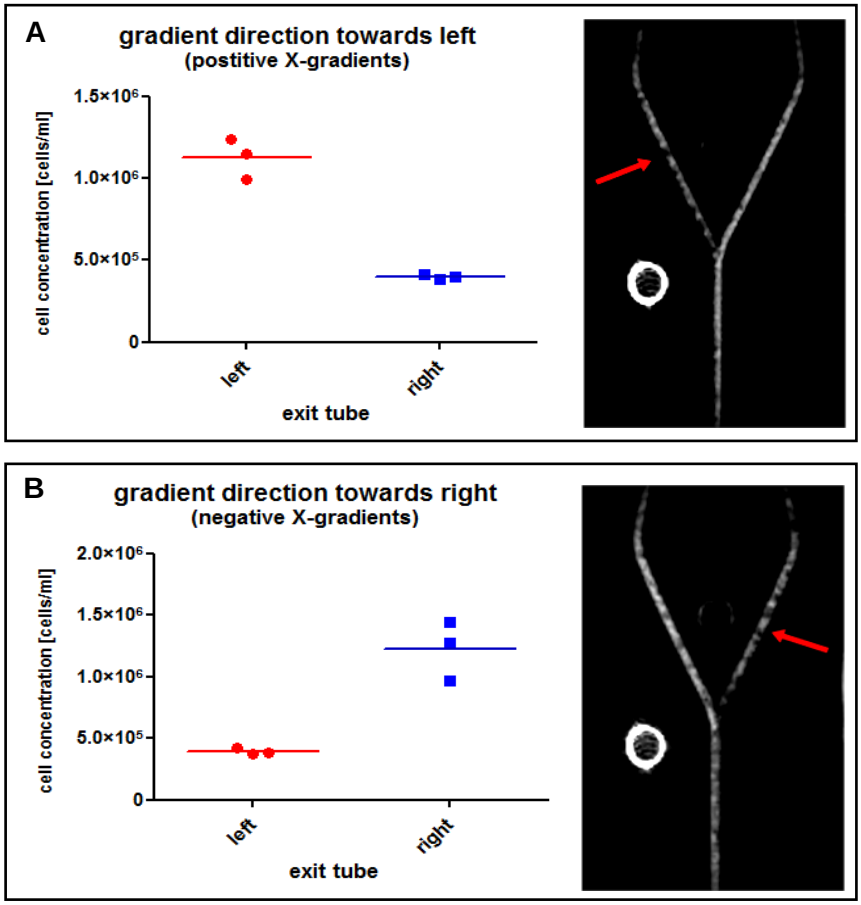

Figure 6: (A) and (B) show the cell concentrations at the exit tubes following application of positive (A) and negative (B) X gradients for cells labelled with BioMag particles at a flow rate of 1 cm/s. Gradient echo images show a reduced signal intensity in the exit branch to which the cells where directed (red arrow) (TE 1.24 ms, TR 100 ms, FA 30°, FOV 50x30 mm, matrix 192x128, NSA 50).

However, increasing the targeting efficiency beyond 50% proved difficult, as further reductions of the flow rate caused substantial agglomeration of cells at the bifurcation point of the phantom. This is illustrated in Figure 7 which shows that the

targeting efficiency for a given flow rate and illustrates its correlation with the amount of internalised iron oxide as equation 2.12 predicts. No statistically significant difference was found for the targeting efficiencies for MNCs labelled with BioMag and MSCs labelled with fluidMAG, which was expected as the amount of internalised iron was in a similar range (fluidMAG 225 ± 30 pg/cell and BioMag 292 ± 17 pg/cell).

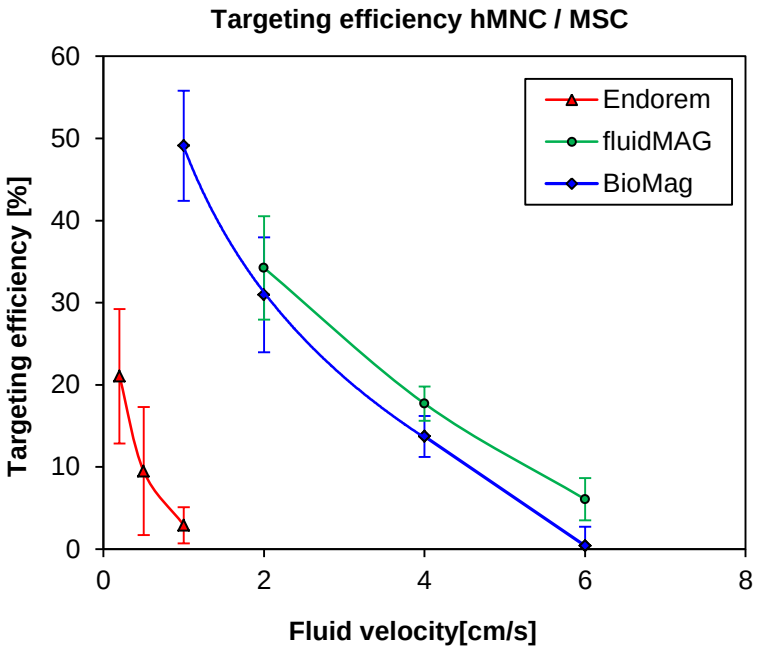

Figure 7: Targeting efficiency for human mononuclear cells (hMNCs) labelled either with Endorem (red triangles) or BioMag particles (blue diamonds) for different flow rates. The green circles show the targeting efficiency for MSCs labelled with fluidMAG particles. Each point on the graph corresponds to the average targeting efficiency for three experiments targeting the right and three experiments targeting the left tube (n=6). The lines connecting the markers are only for illustration purposes.

As previously mentioned, iron oxide particles cause a signal loss in T_2^* weighted MRI images. It was therefore investigated if the labelled cells could be visualised to monitor the cell distribution following MRT. Figure 6 demonstrates that deflected cells could be visualised as a reduction in signal intensity, which is due to the increase of iron oxide per unit volume.

Theoretical predictions of targeting efficiency based on Eq. 2.12 were always lower than experimental results. This is most likely due to iron oxide dipole-dipole interactions leading to cell aggregation, which have not been included in this calculation, but are likely to play a role during targeting. The importance of these interactions will be further investigated in chapter 5.

4.4 Discussion

Different types of commercially available SPION together with two different cell types, which have been previously utilised for cardiac and vascular repair[227-229] were tested for this study. Acceptable SPION labelling concentrations were selected upon their impact on cell viability while their internalisation was estimated via T_2 relaxometry. Endorem and fluidMAG labelling concentrations used in this study are comparable to others[46;100;108;230;231]. Particle internalisation based on this labelling concentrations was in good agreement with previously reported values [44;117;231]. From a magnetic targeting perspective, high iron content per cell is desirable as the magnetic force scales linearly with the amount of internalised iron oxide (see equation 2.12). However, it is clear that high particle concentrations in the culture media can reduce cell viability (see Figure 4) and optimisation of cell labelling (high cellular iron content without loss of cell integrity) is likely to be necessary for each application[117]. Finally, we observed that labelling MNCs with BioMag particles leads to a marked uptake of iron oxide, which we hypothesise would be favourable for cell targeting.

Targeting efficiencies of up to 50% were observed for low to modest flow rates. These efficiencies indicate that without further modification in terms of increased gradient strength or methods to enhance aggregation temporarily, potential in vivo applications would be limited to peripheral vessels with low flow rates. Additionally a temporary reduction of flow rates during delivery might be possible as previously used for the steering of a steel ball in a carotid artery[129]. Our phantom used linear flow while in vivo applications would be exposed to pulsatile non-linear flow profiles. This would reduce the targeting efficiency comparable to the averaged mean flow rate with further reduced for cell path changes due to turbulences. However, the diameter of our phantom is characteristic for small peripheral arteries where the amplitude of the pulsatile flow is already substantially reduced. Effects due to the non-Newtonian characteristics of blood should be small for the selected diameter. The separation distance used for our phantom is longer than expected for an *in vivo* application and would lead a reduction in targeting efficiency directly proportional to the separation length. Any in vivo application is likely to involve more than one bifurcation which would lead to logistic reduction in targeting efficiency dependent on the number of bifurcations through which the cells need to be steered. The potential

scalability of such a system will be discussed in the next chapter together with the parameters of a theoretical model.

Internalisation of large amounts of SPION is not only useful for targeting but obviously equally useful for cell tracking with MRI as it increases the magnetic susceptibility variations. This allows for cell tracking via MRI and potentially for a feedback control. However, a closed control loop might be difficult to achieve as the time window for the detection of cells would be very short (ms range).

The discrepancy between calculated and observed targeting efficiency indicates that cell aggregation is likely to take place and allows for more efficient targeting. This aggregation is likely to be mediated via dipole-dipole interactions whose importance has been demonstrated previously[128;232;233].

4.5 Conclusions

This study demonstrated the feasibility of cell targeting using an MRI scanner. In particular it showed that live human cells can be labelled with different SPION and targeted within a vascular bifurcation model using the magnetic field gradients of an MRI scanner. Depending on the amount of internalised iron oxide particles, targeting efficiencies of up to 50% could be achieved for modest flow rates.

In addition to that, this study showed that imaging of cell distributions following MRT is feasible, indicating the possibility for real-time image-guided targeting using an MRI system.

5 An analytical model for cell delivery in an MRI scanner

The experimental results shown in chapter 4 indicate that targeting efficiency for cell steering in a flow phantom with MRI gradients is strongly influenced by cell aggregation. This chapter aims to develop a simplified analytical model to predict targeting efficiencies and compare these predictions with experimental results. In order to validate the assumption of aggregation due to dipole-dipole interactions a confocal endoscope was used to image cell behaviour inside of the MRI scanner.

5.1 Introduction

This study investigates an important aspect of the magnetically assisted delivery process itself, namely the ability to understand and predict the direction of motion of magnetically labelled cells in the vasculature. For that a simple analytical model describing magnetic cell steering in an MRI scanner was derived. Some practical simplifications were introduced to assist in the cell tracking and steering process, including a weighting factor to account for both the cell distribution in a tube that is projected into a 2D plane, and the presence of prolate spheroids to account for cell aggregation. This model was compared against experimental results which highlighted the importance of cell aggregation at lower flow rates. In order to confirm these predictions we used confocal endoscopic imaging inside and outside of an MRI scanner to visualise cell distribution and aggregation.

The hypotheses for these experiments were:

- A simplified analytical model can be used to describe the cell steering efficiency for a flow phantom in an MRI scanner.
- Cell aggregation due to dipole-dipole interaction is a major factor leading to increased targeting efficiency.
- Cell aggregation can be confirmed experimentally via confocal endoscopy.

5.2 Materials and Methods

5.2.1 Theoretical model

The main driving force for cell movement inside of the MRI scanner is the field gradient produced by the coils used to generate the imaging gradients. The magnetic field $\boldsymbol{B}$ can be described using Maxwell's equations (see 2.1.1):

$$\nabla \cdot \boldsymbol{B} = 0 \text{ , and} \qquad \text{Eq. 5.1}$$

$$\nabla \times \boldsymbol{B} = \mu_0 \varepsilon_0 \frac{\partial \boldsymbol{E}}{\partial t} + \mu_0 \boldsymbol{J} \qquad \text{Eq. 5.2}$$

where μ_0 and ε_0 are the magnetic and electric permeabilities of free space, $\boldsymbol{E}$ the electric field and $\boldsymbol{J}$ the current density. The bore of an MRI scanner is a source free field which means that there are no electric fields or currents present. Accordingly equation 5.2 reduced to:

$$\nabla \times \mathbf{B} = 0 \text{ .} \qquad \text{Eq. 5.3}$$

Equations 1 and 3 can be rewritten in their component forms as:

$$\frac{\partial B_x}{\partial x} + \frac{\partial B_y}{\partial y} + \frac{\partial B_z}{\partial z} = 0 \text{ , and} \qquad \text{Eq. 5.4}$$

$$\left(\frac{\partial B_z}{\partial y} - \frac{\partial B_y}{\partial z}\right) i + \left(\frac{\partial B_z}{\partial x} - \frac{\partial B_x}{\partial z}\right) j + \left(\frac{\partial B_y}{\partial x} - \frac{\partial B_x}{\partial y}\right) k = 0 \text{ .}$$

$$\frac{\partial B_z}{\partial y} = \frac{\partial B_y}{\partial z} \qquad \text{Eq. 5.5a}$$

$$\frac{\partial B_z}{\partial x} = \frac{\partial B_x}{\partial z} \qquad \text{Eq. 5.5b}$$

$$\frac{\partial B_y}{\partial x} = \frac{\partial B_x}{\partial y} \qquad \text{Eq. 5.5c}$$

Equations 5.4 and 5.5 contain five independent derivatives. The first three of them can be selected as the linear field gradients which are derivatives of $\mathrm{B_z}$ as the main field is orientated along the z-axis in MR systems:

$$\mathrm{g_x} \equiv \frac{\partial \mathrm{B_z}}{\partial \mathrm{x}} \text{;} \qquad \mathrm{g_y} \equiv \frac{\partial \mathrm{B_z}}{\partial \mathrm{y}} \text{;} \qquad \mathrm{g_z} \equiv \frac{\partial \mathrm{B_z}}{\partial \mathrm{z}} \text{ .} \qquad \text{Eq. 5.6}$$

For a symmetrical z gradient ($\mathrm{g_z}$) in a cylindrical coordinate system $\partial \mathrm{B_x} / \partial \mathrm{x}$ and $\partial \mathrm{B_y} / \partial \mathrm{y}$ should be identical. We can therefore introduce a symmetry parameter α:

$$\alpha \equiv -\frac{\partial \mathrm{B_x}/\partial \mathrm{x}}{\mathrm{g_z}}; \qquad 1 - \alpha \equiv -\frac{\partial \mathrm{B_y}/\partial \mathrm{y}}{\mathrm{g_z}} \text{ .} \qquad \text{Eq. 5.7}$$

As the last independent variable we can chose equation 5.5c:

$$\beta \equiv \frac{\partial B_y}{\partial x} = \frac{\partial B_x}{\partial y}. \qquad \text{Eq.5.8}$$

All the partial derivatives described in Equations 5.4 and 5.5 can be expressed with the independent variables described in Equations 5.6, 5.7 and 5.8. The field produced by the gradient coils can then be expressed as:

$$\begin{bmatrix} B_x \\ B_y \\ B_z \end{bmatrix} = \begin{bmatrix} \frac{\partial B_x}{\partial x} & \frac{\partial B_x}{\partial y} & \frac{\partial B_x}{\partial z} \\ \frac{\partial B_y}{\partial x} & \frac{\partial B_y}{\partial y} & \frac{\partial B_y}{\partial z} \\ \frac{\partial B_z}{\partial x} & \frac{\partial B_z}{\partial y} & \frac{\partial B_z}{\partial z} \end{bmatrix} \begin{bmatrix} x \\ y \\ z \end{bmatrix} = \begin{bmatrix} -\alpha g_z & \beta & g_x \\ \beta & -(1-\alpha) g_z & g_y \\ g_x & g_y & g_z \end{bmatrix} \begin{bmatrix} x \\ y \\ z \end{bmatrix}. \qquad \text{Eq. 5.9}$$

For MRI gradient coils $\beta \approx 0$ and due to the cylindrical geometry $\alpha = 1/2$. Equation 5.9 can therefore be simplified to:

$$\begin{bmatrix} B_x \\ B_y \\ B_z \end{bmatrix} = \begin{bmatrix} -\frac{1}{2} g_z x + g_x z \\ -\frac{1}{2} g_z y + g_y z \\ g_z x + g_y y + g_z z \end{bmatrix}, \qquad \text{Eq. 5.10}$$

which is an especially convenient algebraic expression for the magnetic field in MRI systems [234], as it is common practice for scanner manufacturers to supply data on g_x, g_y, and g_z amongst the specifications of their instruments (for field maps see Figure 8).

In addition Equation 5.10 shows explicitly that gradients along the x- and y-axes are produced by the B_z field. Hence we can have a magnetic force along those axes despite the magnetisation of material introduced into the field of the scanner being solely along the z-axis.

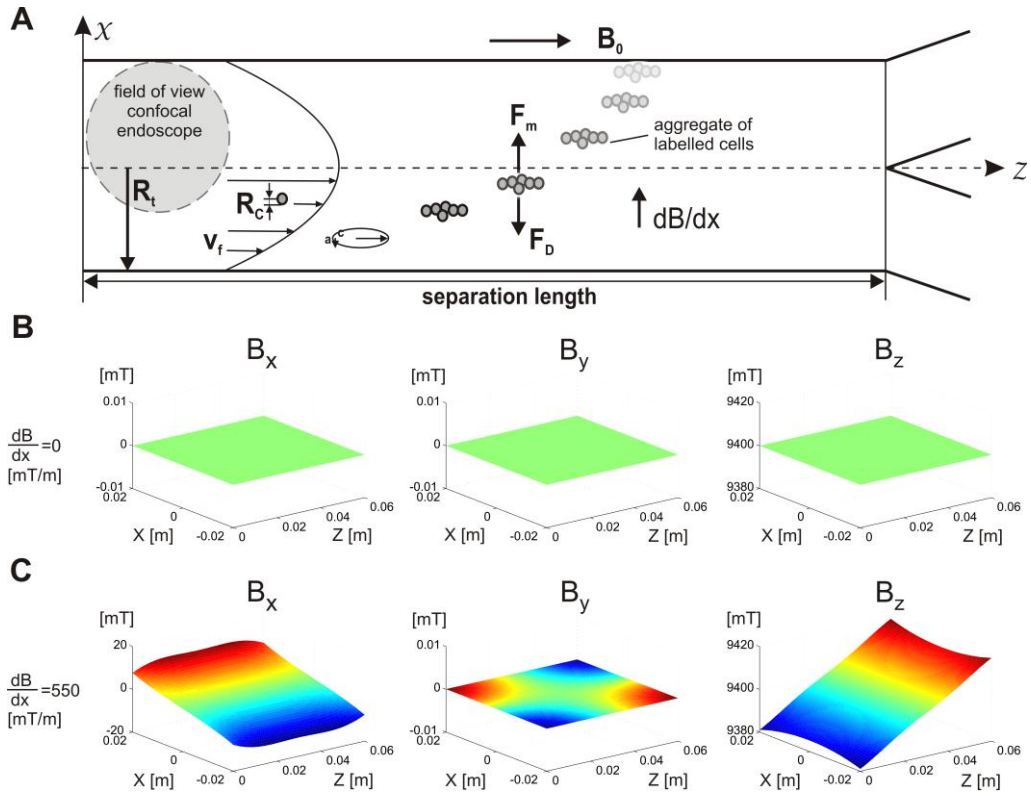

Figure 8: A shows a schematic drawing of the separation area of the vascular flow phantom. An aggregate of magnetically labelled cells is symbolised by grey circles and their path over time by the fading copies of this aggregate assuming a positive X gradient. A grey circle with a dashed line indicates the field of view of the confocal endoscope. B_0: orientation of the magnetic field in the MRI scanner, F_m: magnetic force, F_D: fluid drag force, R_C: radius of cells, R_t: radius of tube, v_f: fluid velocity, a: equatorial radius of prolate spheroid as a model for aggregated cells, c: polar radius of prolate spheroid. B shows three dimensional plots for the magnetic field components (B_x, B_y, B_z) in the MRI scanner without a magnetic field gradient while C shows plots for the magnetic field components in the MRI scanner with a field gradient of 500mT/m applied along the x-axis. (The same coordinate system as used for the model is used for the field plots.

The magnetic force acting on a particle is dependent on its magnetic susceptibility, the field strength and the gradients of the field, which can be expressed as:

$$\boldsymbol{F}_m = (\boldsymbol{m} \cdot \nabla)\, \boldsymbol{B} \text{ , and} \qquad \text{Eq. 5.11}$$

$$\boldsymbol{m} = \frac{V \Delta \chi \boldsymbol{B}}{\mu_0} \qquad \text{Eq. 5.12}$$

where V is the particle volume and $\Delta\chi$ is the magnetic susceptibility difference between the particle and its surrounding fluid.

This equation can be simplified for the case of magnetic resonance targeting (MRT) of cells since the magnetic particles will be fully magnetised due to the strong B_0 field of the scanner. We can therefore simplify equations 5.11 and 5.12 to:

$$\boldsymbol{F}_m = NV(\boldsymbol{M_s} \cdot \boldsymbol{\nabla})\boldsymbol{B} \qquad \text{Eq. 5.13}$$

where N is the number of magnetic particles in a cell and $\boldsymbol{M_s}$ is the saturation magnetisation for a magnetic particle. As the magnetisation of particles in an MRI scanner is mainly along the z-axis, the x and y magnetisation components can be neglected reducing Eq. 5.13 to:

$$[F_{m,x} \quad F_{m,y} \quad F_{m,z}]^T = NVM_z \left[\frac{\partial B_x}{\partial z} \quad \frac{\partial B_y}{\partial z} \quad \frac{\partial B_z}{\partial z}\right]^T \qquad \text{Eq. 5.14}$$

For our experiments only gradients across the x-axis were used (g_x). We can therefore reduce our mathematical model to two dimensions and simplify Eq. 14. An additional scalar needs to be added to account for the fact that imaging gradients can only be switched on for short times at high amplitudes and are therefore operated in an on/off fashion, referred to as the systems duty cycle (D_c). Using that and Equations 5b we can write the magnetic force along the x-direction as:

$$F_{m,x} = NVD_cM_s\frac{\partial B_z}{\partial x}\,. \qquad \text{E.q. 5.15}$$

The magnetic force is opposed by the drag force of the fluid which can be stated as Stokes drag force for low Reynolds numbers:

$$F_d = -6\pi\eta R_c\left(v_c - v_f\right), \qquad \text{E.q. 5.16}$$

where R_c is the cell radius, η the dynamic viscosity and $v_c - v_f$ is the difference between the cell velocity and the fluid velocity.

Cells are likely to aggregate in chain like structures. We can introduce a form factor K_n to extend Stokes drag to non spherical objects[235]:

$$F_d = -3\pi\eta d_n\left(v_c - v_f\right)K_n \text{ , and} \qquad \text{E.q. 5.17}$$

$$K_n = \left[\frac{1}{3} + \frac{2}{3}\,\frac{d_s}{d_n}\right]. \qquad \text{E.q. 5.18}$$

where d_n is the diameter of a sphere with the same projected area as the area of the object projected normal to its direction of motion while d_s is the diameter of a sphere with the same total surface area as the object. For a prolate spheroid Equation 5.18 can be written as:

$$K_n = \left[\frac{1}{3} + \frac{2}{3}\,\frac{a^2 + \frac{ac}{e}\sin^{-1}e}{2ac}\right] \text{ and } e = \sqrt{1 - \frac{a^2}{c^2}}\,, \qquad \text{E.q. 5.19}$$

where a is the equatorial radius and c the polar radius of a prolate spheroid (a<c) as shown in Figure 1.

We can use Eq. 5.17 to investigate the effect of cells arranged to prolate spheroids with different diameter to length ratios l_r on targeting efficiency:

$$l_r \equiv \frac{c}{a} \quad . \qquad \text{E.q. 5.20}$$

As the flow rates used for our experiments are all in the laminar flow region, the inflow profile can be described as:

$$v_f(x) = 2\overline{v_f}\left[1 - \left(\frac{x}{R_t}\right)^2\right], \qquad \text{E.q. 5.21}$$

with R_t as the tube radius and $\overline{v_f}$ the average fluid velocity in the tube. The trajectory of cells can be calculated by equating the magnetic and the drag force (see Figure 8). Note that as our model does not include inertial forces, the cells will immediately travel at the maximum velocity determined by the magnetic and drag forces

$$F_m + F_d = 0. \qquad \text{E.q. 5.22}$$

The cell velocity in the z-direction is determined by the fluid velocity, as there is no magnetic force acting in the z-direction. Therefore the solution for the particle trajectory along the x-axis will be independent of the solution for z. The substitution of Equations 5.15 and 5.17 into Equation 5.22 for x leads to:

$$\frac{dx}{dt} = \frac{NVD_c M_s \frac{\partial B_z}{\partial x}}{3\pi\eta d_n K_n}. \qquad \text{E.q. 5.23}$$

The velocity along the z-axis is given by Eq. 5.21. However as the cell changes its position along the x-axis the velocity changes we therefore have to take the position along x over time into account which leads to:

$$\frac{dz}{dt} = 2\overline{v_f}\left[1 - \left(\frac{x(t)}{R_t}\right)^2\right]. \qquad \text{E.q. 5.24}$$

Equations 5.23 and 5.24 lead to:

$$x(t) = x_0 + v_c t\,. \qquad \text{E.q. 5.25}$$

The velocity of cells due to the magnetic force is given as v_c:

$$v_c = \frac{NVD_c M_s \frac{\partial B_z}{\partial x}}{3\pi\eta d_n K_n}, \qquad \text{E.q. 5.26}$$

and the position along z as a function of time as:

$$z(t) = 2t\overline{v_f} - \frac{2t^3 v_c^2 \overline{v_f}}{3R_t^2} - \frac{2t^2 v_c \overline{v_f} x_0}{R_t^2} - \frac{2t\overline{v_f} x_0^2}{R_t^2}. \qquad \text{E.q. 5.27}$$

In order to calculate the targeting efficiency, the initial distribution of cells in the tube at the start of the separation length (z=0) needs to be taken into account. It is assumed that the cells are randomly distributed over the circular tube cross-section. If this distribution is projected into the plane we derive:

$$W(x) = 2R_t \sin\left(\cos^{-1}\frac{x}{R_t}\right), \qquad \text{E.q. 5.28}$$

where W is a weighting factor for the cell number distribution at the start of the separation area. The trajectories for cells can be calculated using Eqs. 5.25 and 5.27 (see Figure 9). If they are weighted with Eq. 5.28 the distribution at the start and end of the separation distance can also be calculated.

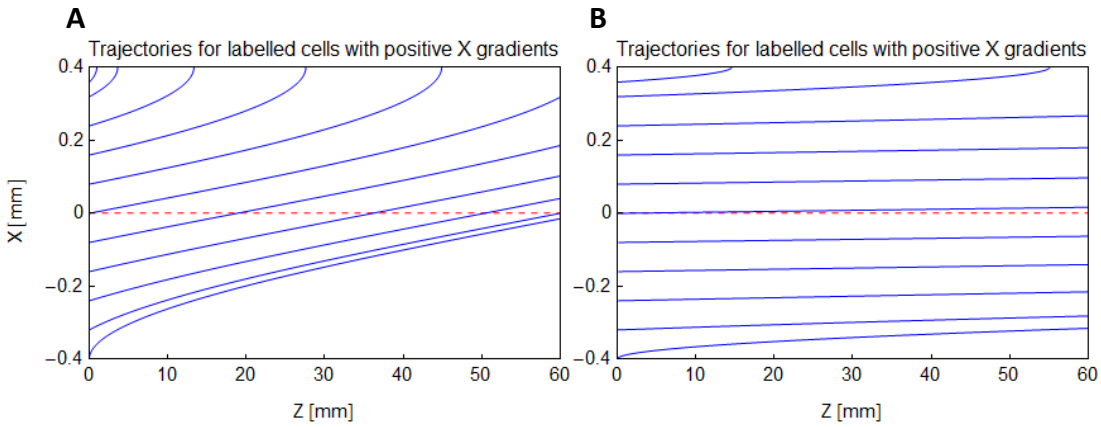

Figure 9: (A) shows the trajectories for case with 95% targeting efficiency while (B) shows trajectories for a case with 5% targeting efficiency.

It is assumed that cells which are above or below the z-axis at the end of the separation length z_0 (see Figure 8) will end up in their corresponding exit tubes. The targeting efficiency can hence be defined at that point as follows:

$$T_e = 2 * \left(\frac{N_{target\ tube}}{N_{total}} - 0.5\right), \qquad \text{E.q. 5.29}$$

where $N_{target\ tube}$ is the number of cells at the end of the tube to which the cells were targeted to and N_{total} is the total amount of cells in both tubes. The subtraction of 0.5 is accounting for the distribution without any steering gradients present, which is 0.5 for both exit tubes.

In order to estimate how much iron oxide needs to be internalised per cell to achieve a certain steering efficiency Eq. 5.28 needs to be integrated. For a selected targeting efficiency T_e, the fraction of $N_e = \frac{N_{target\ tube}}{N_{total}}$ cells have to end up in the targeted tube. We therefore integrate Eq. 5.28 from -R_t to x_{te} if the magnetic force points along the positive x-axis. In this case x_{te} indicates the position along the x-axis for

which the integral between it and R_t accounts for T_e of all cells. We can solve the following equation for x_{te}:

$$N_e R_t^2 \pi = R_t \left(x_{te} \sqrt{1 - \frac{x_{te}^2}{R_t^2}} + R_t \sin^{-1} \frac{x_{te}}{R_t} \right) + \frac{R_t^2 \pi}{2} \qquad \text{E.q. 5.30}$$

If we chose T_e to be 0.9, than form Eq. 5.28 it follows that N_e has to be 0.95.

In order to achieve the 0.9 targeting efficiency, a cell starting at x_{te} and z=0 has to reach $x = 0$ at the end of the separation length z_0. Equation 5.27 and 5.25 can be solved for t:

$$t = \frac{3R_t^2 z_0}{2\bar{v}_f (3R_t^2 - x_{te}^2)} . \qquad \text{E.q. 5.31}$$

From Equations 5.30 and 5.25, N_p can be calculated as well as the field gradient strength or duty cycle necessary to reach a given steering efficiency. For parameters used in the model see Table 1.

Table 1: Model parameters

Variable	Symbol	Value	Units
magnetic induction	B_0	9.4	T
gradient strength	g_x	0.5 (0.5-10)	T m^{-1}
saturation magnetisation	M_s	314 000	A m^{-1}
number of particles per cell	N	250	
tube radius	R_t	0.0004	m
cell radius	R_c	0.000005	m
average fluid velocity	$\bar{v}_f$	0.005-0.08	m s^{-1}
separation length	z_0	0.06	m
Duty cycle for steering gradients	D_c	2/7	
fluid viscosity	η	0.0016-0.0024	kg m^{-1} s^{-1}
diameter length ratio	l_r	5	
cells in one aggregate		1-80	

5.2.2 Magnetic resonance targeting of cells

Magnetic steering experiments were performed in the same ways in section 4.2.4 with minor differences outlined below. In order to investigate the effect of different viscosity on targeting efficiency by suspending cells in PBS containing 3% foetal bovine serum FBS or 50% FBS. Additionally the effect of increased cell concentrations was investigated by doubling the cell concentration.

5.2.3 Confocal endoscopy

Confocal endoscopic imaging was performed by Baptiste Allain (Centre for Medical Image Computation (CMIC), UCL). The Cellvizio (Mauna Kea Technologies, Paris, France), a fibered confocal microscope, was used for the acquisition of dynamic microscopic *in vitro* images of the fluorescent cells. An MR compatible (7 metre long) 600 micron diameter microprobe, comprising approximately 10,000 coherent optical fibres was scanned fibre by fibre via the MKT laser scanning unit behaving as the confocal pinhole and objective lens of a conventional near real-time confocal microscope for remote acquisitions at 12 frames per second.

The MR-compatible ProFlex S-microprobe was used which provided an image resolution of approximately 4 µm and a circular field of view with a diameter of 500 µm. The end of the optical fibre was placed into the middle of the inflow channel of the flow phantom where a hole was drilled to connect it to the fluid (see Figure 8 and Figure 11). The laser scanning unit emitted a laser beam at an excitation wavelength of 488 nm and collected the fluorescence signal in a bandwidth of 500 nm to 650 nm. Finally, ImageCell Software allowed for real-time visualisation of the microscopic images and for manual settings of the contrast.

5.3 Results

Figure 10A shows a comparison between experimental results and theoretical predictions for two different cell concentrations, together with the theoretical prediction without cell aggregation. This figure demonstrates that the theoretical prediction for single cells differs significantly from experimental results, indicating that aggregation could play an important role, which may explain the discrepancy with the experimental data. When cell aggregation was assumed, cells were modelled as prolate spheroids with a polar to equatorial diameter ratio of $l_r = 5$. Cell aggregation and aggregate shape were included in our model via Equations 15 and 18. The number of cells N in such an aggregate was derived via fitting the experimental data to the model while the diameter length ratio was estimated from confocal endoscopy data. For N with the range 60 to 80 coefficients of determination (R^2) were found to be between 0.93 and 0.97, showing a good agreement between the model and experimental data.

It should be stated that the numerical validity of the results is dependent on the validity of the model assumptions of no gravitational and inertial effects. Neither gravity nor inertia are likely to have a significant effect on our predictions, as sedimentation is slow and the cells pass through the flow phantom within a few seconds. Inertia is neglectable for small cells, especially when the magnetic force is applied for the entire time a cell spends in the flow phantom. The assumption of a random distribution for cells entering the separation area is harder to assess as a long tube is used to connect the phantom with the syringe pump. However, applying gradients along the positive or negative x-axis led to similar results indicating no initial bias. Finally the assumption of a laminar parabolic flow profile is justified for the fluid viscosities and flow rates used in our experiments

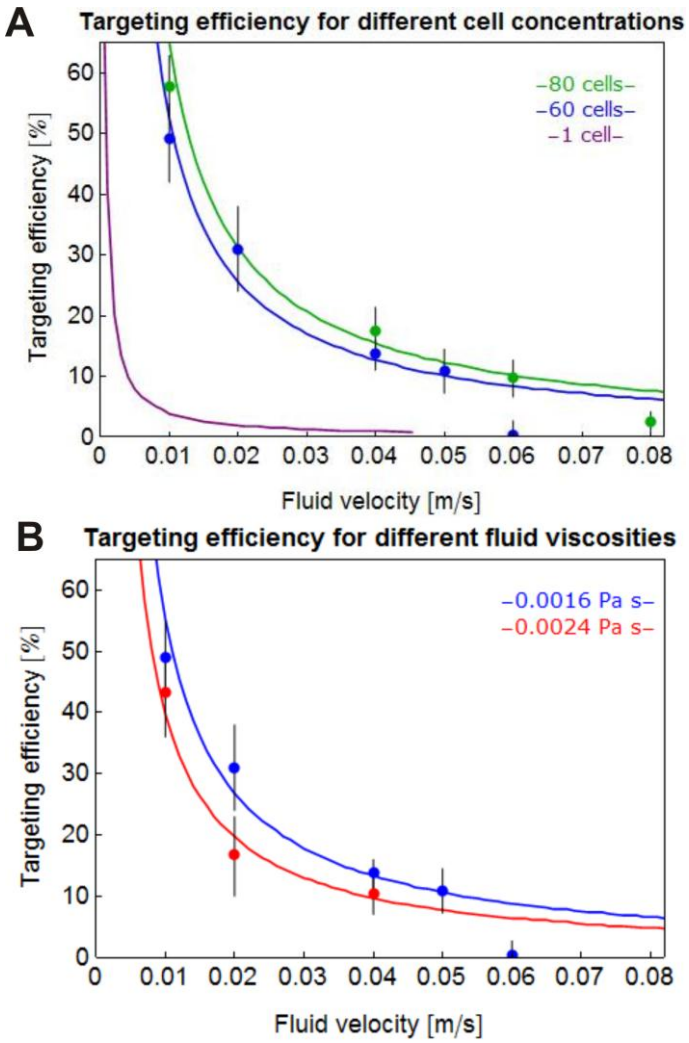

Figure 10: (A) Comparison of experimental results versus theoretical prediction for targeting efficiency. The green dots show the experimental results for a cell concentration of $4x10^6$ cells/ml while the blue dots correspond to $2x10^6$ cells/ml, vertical bars indicate the standard deviation. Theoretical predictions are shown as continuous lines; purple: no cell aggregation, blue: 60 cells aggregated with a prolate equatorial to polar diameter ratio of 5, green: 80 cells aggregated with the same diameter ratio. (B) The effect of different fluid viscosities on targeting efficiency. Blue and red dots show experimental results for PBS+3% serum and PBS+50% serum (roughly the viscosity of blood). The continuous lines show the theoretical predictions for a viscosity of 0.0016 Pa s and 0.0024 Pa s assuming no changes in aggregate size. Blue and red dots show the measured targeting efficiency (mean ± SD, n=6)

A minor increase in targeting efficiency was observed when the cell concentration was doubled. This indicates that aggregate sizes might not change much for the increased cell concentration. The theoretical model used a constant aggregate size which is likely to be incorrect particularly for higher flow rates where increased shear forces overcome magnetic dipole interactions and hence aggregation (see confocal results below). We therefore see a discrepancy between the model and

experimental data starting between 5 and 6 cm/s for $2x10^6$ cells/ml and 6 and 8 cm/s for $4x10^6$ cells/ml. Figure 10B shows experimental results and theoretical predictions for two different fluid viscosities. The increases in fluid viscosity led to a modest decrease in targeting efficiency. Changing the fluid viscosity does affect the drag force which needs to be overcome and to a lesser degree cell aggregation. Increasing the fluid viscosity to the viscosity of blood did only lead to a slight reduction in targeting efficiency (Figure 10B).

This can be seen in Figure 10B for which the aggregate size was kept at 60 cells with a diameter to length ratio of 5 and measured fluid viscosities were used to calculate theoretical targeting efficiencies. These predictions fit the experimental data assuming that the aggregate size does not change significantly.

A confocal endoscope was used to investigate cell aggregation. This system operates as a conventional confocal microscope as the coherent fibre bundle is rapidly scanned point by point, conducting light to and from the sample, acting as both the objective lens and the confocal pinhole. Figure 11 shows single frames from videos taken at different fluid velocities without a magnetic field present and with a homogenous magnetic field of 9.4T (bore of the MRI scanner). For fluid velocities of 1 cm/s and 2 cm/s (Figure 11A and B) cells travelled as aggregates in the magnetic field of the MRI scanner; these aggregates showed roughly elongated shapes containing between 20-80 cells. We estimated the diameter to length ratio of these aggregates to be around 5. For the same experiments conducted without a magnetic field (outside of the MRI scanner), no cell aggregation was observed.

When the fluid velocity was increased to 4 cm/s (Figure 11C) cells did not form large aggregates but rather chain-like aggregates with 2 to 10 cells arranged into a chain. The transition between large aggregates (several 10s of cells) and smaller chain like aggregates was observed at a fluid velocity of approximately 3 cm/s. It has to be accepted that the imaging fibre was introduced into the flow phantom (see Figure 11D) and may have caused some minor flow disturbances.

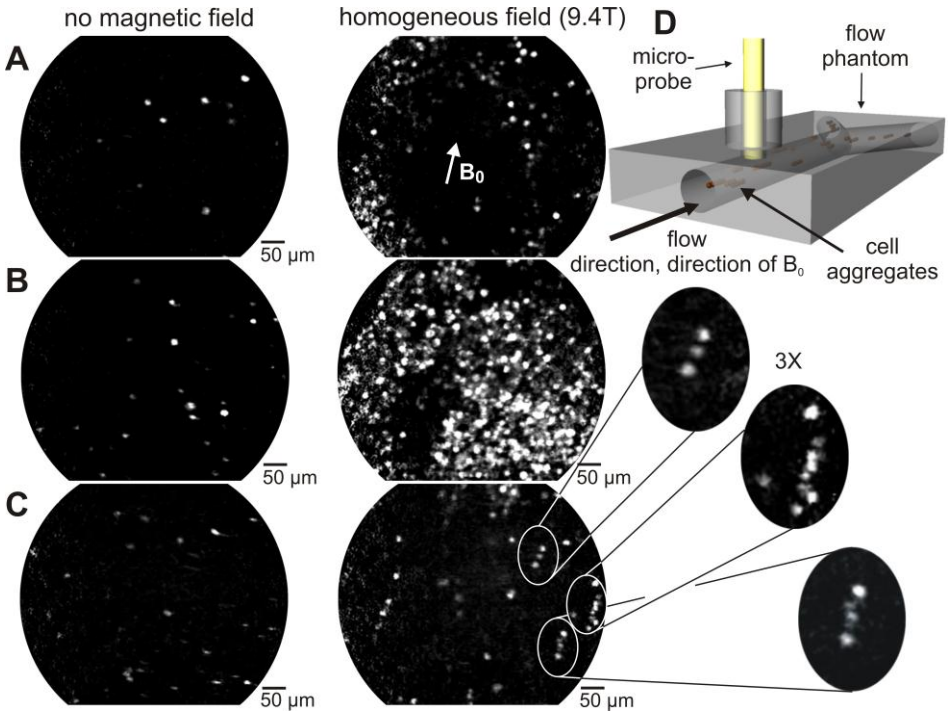

Figure 11: Singe frame images from confocal endoscopy videos acquired at a frame rate of 12 images per second for different fluid velocities without a magnetic field and in an homogeneous magnetic field of 9.4T (inside the bore of an MRI scanner). The left column corresponds to no magnetic field while the right column corresponds to 9.4T. A: flow rate of 1 cm/s, B: 2 cm/s, C: 4 cm/s. The scale bar in the lower right hand corner of each image indicates 50 µm while the field of view is 500 µm with a depth perception of about 100 µm. The arrow in the right column figure A indicates the orientation of the magnetic field for the whole right column. D shows a schematic drawing how the microprobe was introduced into the flow phantom and how chain like aggregates are aligned with the main field of the MRI scanner (B0). In the lower right hand corner chain like aggregates of cells are magnified by a factor of three (3X).

The mathematical model permits the investigation of the effects of different parameters on targeting efficiency (see section 5.2.1). Figure 12A for example shows the volume fraction that iron oxide particles would need to take up in a cell to reach a targeting efficiency of 90% for different gradient amplitudes. For this plot no cell aggregation was assumed.

Figure 12B shows the effect of the aggregate geometry on the targeting efficiency. As the magnetic force is a volumetric force and the drag force is dependent on the projection surface in flow direction, the deviation from a spherical object to an elongated one reduces the targeting efficiency. From the analysis of our videos we observed that the equatorial to polar diameter ratio is approximately five. If 40 cells in

one spherical aggregate are necessary to explain the experimental results shown by the blue line in Figure 10A, the number of cells in one aggregate with a diameter to length ratio of 5 will increase to 60. The diameter to length ratio of aggregates is dependent on the polydispersity of the solution. It might therefore be possible to add a small concentration of ferrofluid to increase the size of these aggregates and reduce their diameter to length ratio.

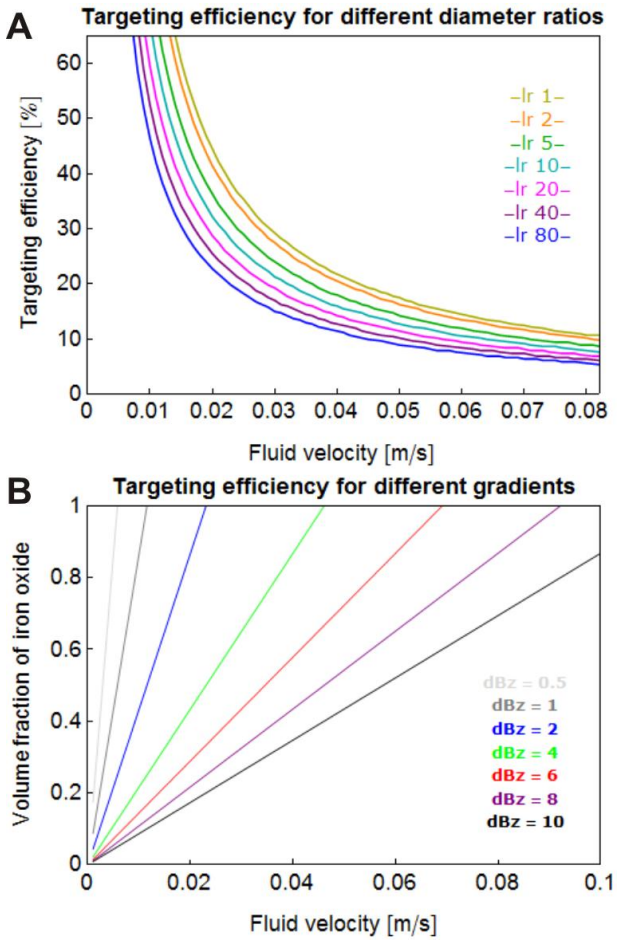

Figure 12: (A) The effect of different polar to equatorial diameter ratio on targeting efficiency assuming the total number of cells in an aggregate is constant. (B) Predictions for the volume fraction on iron oxide in cells necessary to reach a given targeting efficiency without cell aggregation for different gradients strengths at a duty cycle of 50%. gx: gradient strength T/m.

5.4 Discussion

The comparison between experimental results and theoretical predictions showed that aggregation is a likely candidate to explain the discrepancies between the two. Predictions fit the experimental data assuming that the aggregate size does not change significantly when viscosity and cell concentration are changed. The importance of magnetic dipole interactions for targeting applications have been

described previously [144;232;236]. Also there have been previous publications where a similar bifurcation has been modelled but in the context of permanent magnets and without cell aggregation [237;238]. However, in comparison to these studies we used cells with internalised particles and not magnetic particles alone. This changes aggregation behaviour as particles are kept at greater distances due to other cellular compartments and their membranes, while aggregated cells might stick together more readily depending on the cell line used. Forces which oppose aggregation of particles are electrostatic and van der Waals forces. These forces have a shorter range compared to magnetic dipole interactions and are shielded to a large extend by the cells. We should therefore expect slight differences between the aggregation behaviour of ferrofluids and cells even if the same iron concentration per unit suspension volume is used.

Mathieu et al. [232] showed that the average chain length of iron oxide particles without fluid flow at a concentration of 0.6 mg/ml and 0.4 T was about 31µm and for 1.13 mg/ml at a flow rate of < 1.2 cm/s in an 1.5 T MRI scanner approximately 650 µm. In our study, we reached an iron concentration, per unit suspension volume, of approximately 0.5 mg/ml in labelled cells and observe aggregates with a length of 150-250 µm. This difference could be attributed to the internalisation of particles by cells and the difference in fluid velocity, which may increase aggregation. We also observed that, cells with internalised particles showed different aggregation behaviour at lower flow rates while aggregation at higher flow rates follows a similar (chain) pattern as observed for ferrofluids. The aggregation behaviour observed for low flow rates might, in part, be caused by the strong field gradients at the bore of the magnet. These gradients will induce transverse motion which will increase the likelihood for aggregation as cells will come close enough to other cells to experience their magnetic dipole moment.

Cell aggregation is clearly an important factor for cell targeting using MRT and will always be present unless very dilute suspension is used or cells contain only a very low amount of iron oxide are used. The higher magnetophoretic velocity of aggregates allows for increased targeting efficiency at higher flow rates. This can be further enhanced by increasing the cell concentration in the injection solution. However, if small vessels are to be targeted, large aggregates might perturb blood flow leading to vessel occlusion. Although shear forces will increase in small capillaries, it is not certain if these forces will be big enough to disaggregate cells. However, the nanoparticles

used for these experiments are superparamagnetic and the removal of the subject from the strong field of the MRI scanner would lead to the decay of dipole interactions and thus the cells should be able to disperse. This should also be the case for ferrofluids. However, there is an additional risk that during the contact time between cells, some may have bound together too strongly to be dispersed by the fluid flow. This is of particular relevance for MRT, but it will also be of importance for magnetic targeting applications that use permanent or electro magnets. Further research will be needed to address this question.

The theoretical model shows that achieving high targeting efficiency at higher fluid velocities will be difficult. However, it will be necessary to achieve higher targeting efficiencies for such velocities if this is to be applied for bigger blood vessels. One option would be to increase the gradient strength of the system as indicated in Figure 12B. This can be achieved easily for small bore MRI systems but will be difficult for human MRI systems. Exploring possibilities to aggregate cells to bigger clumps for steering in big vessels might be a more favourable option to increase targeting efficiency. Another possibility might be to reduce the blood flow rate temporarily via the catheter used for cell delivery if that is acceptable from a medical perspective. Achieving high targeting efficiencies in major blood vessels is not only limited due to increase blood flow rates which reduce the available time to deflect a cell towards on exit branch of a bifurcation but also by turbulences in the fluid flow which might defect a cells to the opposite exit branch.

5.5 Conclusions

The model above describes the steering efficiency of magnetically labelled cells inside a small bifurcation in the context of MRT. Such a model could be used for the implementation of an active control strategy for cell delivery using MRT. This model takes cell aggregation into account and models these aggregates as prolate spheroids. Predicted targeting efficiencies agree with experimental results when cell aggregation is taken into account, highlighting the importance of cell aggregation in this context. This aggregation behaviour did not change much when cell concentration or fluid viscosity where changed in our model or experimental setup.

Aggregation of cells inside the MRI scanner was confirmed via confocal endoscopy. Confocal endoscopy showed aggregate sizes at lower flow rates which are

in the predicted range of our theoretical model. A transition from large aggregates containing up to 100 cells to small chain like aggregates with up to 10 cells at flow rates of > 4-6 cm/s was found.

6 Magnetic cell delivery to lower leg arteries

Chapters four and five were focused on the use of an electromagnet system (MRI scanner) for magnetic cell delivery. In contrast to these chapters, the current chapter will focus on the feasibility of magnetic cell delivery to human lower leg artery using permanent magnets. A range of potential magnet arrangements has been evaluated for a realistic vessel configuration using a finite element approach. The best performing magnet arrangement has been used for fluid dynamics simulation to investigate if labelled cells can be captured for flowing blood. Finally the behaviour of labelled vessel close to the arterial wall has been simulated using a fluid structure interaction model.

6.1 Introduction

The problem of restenosis and the potential of cellular therapies such as EPC delivery has been outlined in chapter one. Based on that premise this study will investigate the feasibility of magnetic cell delivery in that context theoretically. Despite the potential advantages of magnetic cell delivery, no clinical trials have been conducted so far. One of the key reasons for this lies in the nonlinearities of the scalability of magnetic delivery strategies. A common limitation of all strategies is the rapid decline in magnetic field and gradient strength with increasing distance from their source. Accordingly strong magnetic forces can easily be achieved in small animal models but are almost impossible to achieve for human dimensions.

This study starts with the hypothesis that optimisation and feasibility assessment of magnetic cell delivery should start with human dimensions followed by a scale-down to an appropriate animal model[239-241], such that the forces acting on cells are kept constant if possible. Following this hypothesis, the aim of this study is to investigate the theoretical feasibility of magnetic cell delivery to the arteries of the lower leg as a potential supplementary treatment after balloon angioplasty for PAD, in order to improve re-endothelialisation and increase vessel patency.

In this study MRI angiograms were acquired from healthy volunteers whose leg dimensions were selected to best reflect diabetic patients with PAD. The resulting angiograms were used to define the position of the three major vessels in the lower leg (peroneal, anterior and posterior tibial artery) and the skin in 3D. Three dimensional vessel positions were used for a finite element model (FEM) optimisation of a range of different magnet configurations in 3D. A computational model of the blood vessels, together with boundary conditions from magnetic resonance phase-contrast images were used for computational fluid dynamics (CFD) simulations. This allowed the comparison of the fluid and magnetic forces acting on labelled cells, allowing an estimation of the maximum distance for cells drifting near the vessel wall to be captured by the magnetic field. Moreover the best performing design was scaled down for a rabbit arterial injury model of the common carotid artery whilst maintaining a constant force acting on cells.

The hypotheses for these experiments were:

- Finite element models can be used to optimise potential magnet arrangements for a specific application.
- Computational fluid dynamics can be used for theoretically assessments of the feasibility to capturing cells from the blood stream under realistic flow conditions.
- A magnet arrangement optimised for human dimensions can be scaled down to the dimension of an animal model while keeping forces acting on cells essentially constant.

6.2 Materials and Methods

6.2.1 Dimensions of legs with PAD

In order to obtain an estimate for the dimensions of diabetic PAD legs the circumference of legs below the knee, at the maximum Gastrocemius (calf muscle) circumference and above the ankle, were measured following the protocol approved by the department of health and UCL ethics committee from twenty consecutive outpatients (59 ± 12 years, six female) who gave their consent. All of these patients had ulcers or gangrene and a history of diabetes mellitus. Informed written consent was obtained from three healthy volunteers (25 ± 4 years, two female) for MRI data acquisition to provide an anatomical model of the arteries in the lower leg. These MRI scans were acquired using a protocol approved by the department of health and UCL ethics committee.

6.2.2 Acquisition of human MR data

Human MRI data was acquired by Anthony Price (Robert Steiner MRI Unit, Imaging Sciences Department, Hammersmith Hospital Campus, Imperial College London) Magnetic resonance imaging was performed on a 3 T Philips scanner (Best, The Netherlands) using an 8-channel phased-array receive coil. Axial 2D time-of flight angiography images were acquired downstream of the branching of the peroneal and posterior tibial arteries. One hundred consecutive slices were acquired using the following parameters: field of view (FOV) 120x120 mm, slice thickness 2 mm, matrix size 160x160, flip angle (FA) 50°, echo time (TE) 4 ms, repetition time (TR) 21 ms, reconstructed to 0.25x0.25x2 mm. 2D phase contrast (velocity encoded) gradient echo images were acquired for the inflow and outflow slice of this volume. Twenty time frames were acquired to cover one cardiac cycle using echocardiography retrospective gating and the following imaging parameters: TR 12 ms, TE 7 ms, number of signal averages (NSA) 3, FA 10°, velocity encoding 80 cm/s, reconstructed to 0.5x0.5x2 mm.

6.2.3 Acquisition of rabbit MR data

A sacrificed rabbit (2 kg) was scanned using a 9.4T Agilant Technologies VNMRS scanner (Palo Alto, CA) in order to generate a data sate for scale down of the simulations to a suitable animal model. Consecutive axial gradient echo slices were acquired to cover the whole neck area with a 72 mm volume coil (Rapid Biomedical, Rimpar, Germany) using the following imaging parameters FOV 60x60 mm, slice thickness 1 mm, Matrix size 512x512, TR 1370 ms, TE 7 ms, NSA 8, FA 30°.

6.2.4 Magnet optimisation using finite element methods

Permanent magnets offer high field strength without the need for electric power or cooling. However, as there are many potential arrangements, a rational optimisation is necessary.

We used commercially available finite element modelling software Opera v12, TOSCA (Kidlington, UK) to calculate the magnetic field distribution in three dimensions for four basic geometries: Halbach cylinder (in this study always a hollow cylinder), linear Halbach array, equilateral triangular rod and magnetic rod (see Figure 13). In order to test for mesh independence of our finite element simulations, all element sizes were halved for one simulation for each geometry which led to an error in the magnetic force of < 0.7% on average.

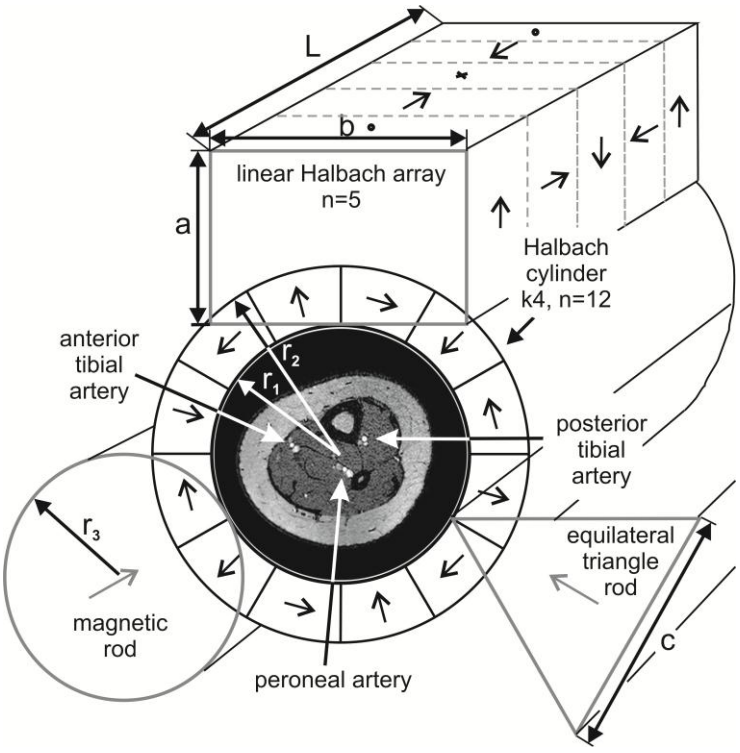

Figure 13: Geometrical arrangement of different magnet shapes around a human leg. A magnetic resonance image is shown in the centre of the Halbach cylinder to indicate the three major blood vessels of the lower leg. Open arrows indicated the magnetisation orientation of different elements. Note that only one of the basic geometries was used at one time for finite element simulations.

The Halbach cylinder is a one sided flux concentrator with continuously changing magnetisation direction[112] (φ) following,

$$\varphi = k\,\phi\,, \qquad \text{E.q. 6.1}$$

with k as a positive integer between 2 and 4 for internal flux concentration and ϕ the angel for the position around a circle. However, as this would be difficult to build, in practice Halbach cylinders are built out of segments with a constant magnetisation using equation 6.1 for the centre of each element. This leads to a reduction of the flux density[112] following

$$B(n) = B_c \frac{\sin(2\pi/n)}{2\pi/n}, \qquad \text{E.q. 6.2}$$

where B_c stands for the magnetisation of a Halbach cylinder with continuously changing magnetisation orientation and n for the number of elements.

A linear Halbach array is also a one-sided flux concentrator which follows the same principle as the Halbach cylinder (magnets with sinusoidal magnetisation produce single sided fields). The magnetisation orientation makes one full rotation along L (one wavelength) focusing all magnetisation on the lower side of the array.

For each of the four geometries tested, the magnets were arranged around an air cylinder (placeholder for a human leg) with a radius of r_1=80 mm and a length of L=200 mm (for a full list of model parameters see Table 2) while r_2, r_3, c and a (see Figure 13) were increased to calculate the magnetic field for an increasing magnet volume. An MRI angiogram of a leg was centred in the air volume to get blood vessel positions in 3D space. For each of the three vessels considered, magnetic forces acting on cells in the centre of them were calculated at 20 points along their centreline. Magnets arranged around the air cylinder were rotated 360° around its long axis in 36 steps. Forces acting on cells for 60 points (20 points, 3 blood vessels) of each rotation step were evaluated. The rotation which generated the highest force over all 60 points was selected and their average has been used for average force plots. Force calculations were performed using Matlab (R2010a, Natick, MA).

Table 2: Physical parameters used for this study

Parameter	Symbol	Value	Units
Length for magnets and vessel section	L	**200**, 40 (30)*	mm
Halbach cylinder inner radius	r_1	**80** (54-98), 25*	mm
Halbach cylinder outer radius	r_2	**140** (82-240), 29*	mm
Magnetic rod radius	r_3	**115** (18-226)*	mm
Linear Halbach array height	a	**259** (6-1005)*	mm
Linear Halbach array width	b	**160** (40-160)*	mm
Equilateral triangle side length	c	**309** (75-609)*	mm
Outer radius endplate	r_4	**130** (100-140)*	mm
Endplate angle	α	**45** (30-90)*	°
Endplate hight	h	**25** (5-50)*	mm
Residual flux density NdFeB†	B_r	1.36	T
Coercivity NdFeB†	H_c	1051	kA m^{-1}
Relative permeability NdFeB†	μ_r	1.04	-
Residual flux density sintered ferrite	B_r	0.37*	T
Coercivity sintered ferrite	H_c	240*	kA m^{-1}
Relative permeability sintered ferrite	μ_r	1.21*	-
SPION‡ crystal size	D	8.8	nm
Saturation magnetisation iron oxide	M_s	354	kA m^{-1}
Temperature	T	300	K
Magnetic permeability free space	μ_0	$4*\pi*10^{-7}$	H m^{-1}
Boltzmann constant	k_b	$1.38*10^{-23}$	J K^{-1}
Cell radius	R_c	10	µm
Cell density	φ_c	1100	kg m^{-3}
Young's modulus cells	-	10	kPa
Poisson ratio cells	-	0.45	-
Dynamic viscosity, fluid	η	0.0039	kg m s^{-1}
Fluid density	φ_f	1080	kg m^{-3}

* Bold numbers indicate dimensions which were used for the comparison of magnet arrangements with the same volume. Blue numbers indicate values used for the rabbit scale model. † NdFeB Neodymium Iron Boron, ‡ SPION superparamagnetic iron oxide nanoparticles

All of these geometries, except for the Halbach cylinders have a one sided distribution of magnet material. In order to investigate different arrangements of the basic geometries a magnet volume was selected (6600 cm^3) and kept constant while the number of basic geometric elements (linear arrays, rods, triangular rods) around the air cylinder was increased. For example 1, 2, 4, 6, 8, 10, 12 magnetic rods were equally spaced around the air cylinder while r_3 was decreased to keep the total magnet volume constant. The magnetisation was orientated towards the centre for n=1, following a dipole orientation for n>1 and following a quadrupole orientation for n>4 as given by,

$$\varphi = \left(1 + (p/2)\right)\phi\,, \qquad \text{E.q. 6.3}$$

with $p = 2$ for a dipole and $p = 4$ for a quadrupole.

For the Halbach cylinders, a k3 variety was used with decreasing n leading to a magnetic hollow cylinder with a single magnetisation orientation for $n = 1$. Magnetisation orientations for the linear Halbach array were kept constant, but a and b were adjusted in order to fit n linear arrays around the air cylinder.

To address the scalability of a Halbach cylinder k3 for a range of potential human leg diameters the ratio of r_1/r_2 was kept at 0.62 while r_1 was increased from 54 to 98 mm.

All of these simulations were done in 3D using the demagnetisation curve of commercially available Neodymium-Iron-Boron magnet standard grade 45SH (remanence magnetisation B_r=1.36 T, coercivity H_c=1051 kA/m, relative permeability μ_r=1.04)[1]

Finally simulations for the scale down of a Halbach cylinder k3 for a rabbit common carotid artery model, with r_1=25 mm and L=40 mm, were performed using the demagnetisation curve of commercially available magnetic sintered ferrite (B_r=0.37 T, H_c=240 kA/m, μ_r=1.21)[2].

6.2.5 Model construction for computational fluid dynamics

In this study, the geometry of the arterial system has been simplified from a three-dimensional tube to a two dimensional channel in order to reduce the computational cost of the simulations. The geometry has been taken as a channel section 2.2 mm in diameter (according to the MR angiogram); 200 mm in length and 0.11 mm in width (see Figure 21). The fluid has been modelled as incompressible Newtonian fluid with a density of 1080 kg m^{-3} and a viscosity of 0.0039 kg m s^{-1} (density and viscosity of blood). The volume was meshed using mixed tetrahedral and hexahedral elements (Figure 21) and was tested for mesh independence by applying a constant velocity boundary condition at the inlet of 0.25 m s^{-1} (maximum difference between inflow and outflow boundary value), 0 Pa pressure at the outlet and symmetry boundary conditions enforcing the two-dimensional flow. Velocity variations down the centre of the channel were assessed and the mesh was determined sufficiently fine when the maximum percentage difference between

[1] Neodymium-Iron-Boron Magnets. http://www.tdk.co.jp/tefe02/e331.pdf
[2] Sintered ferrite magnets. http://www.magnetsales.co.uk/sintered-ferrite.htm

successively finer meshes was found to be less than 1%. The final mesh consisted of 156155 nodes and 419191 elements.

Flow profiles were extracted from phase contrast images using the freely available software Segment version 1.8 R0462 (http://segment.heiberg.se)[242]. The average velocity recorded at both inlet and outlet was fitted to an 8th order Fourier series using MATLAB. These were then applied to the fluid domain as inlet and outlet velocity boundary for the channel.

For the rabbit common carotid artery, a channel diameter of 1.5 mm, a length of 30 mm and a width of 0.11mm were used. For the inflow boundary an interpolated spline fit was performed using MATLAB with the flow profile from Cui et al.[243] while the outflow pressure boundary was set to 0 Pa.

6.2.6 CFD simulations and post processing

Computational fluid dynamics modelling was performed by Kevin Lau (UCL mechanical engineering) using ANSYS CFX 11.0, a finite volume based computation fluid dynamic solver, which solves the unsteady equations for mass and momentum conservation of an incompressible fluid. The unsteady flow dynamics are solved by advancing the solution with time steps of 0.01 s. At each time step the residuals of the non-linear system are reduced till either the maximum of the residuals of both the velocities and pressures were less than 10^{-6} or 100 convergent iterations had been performed. In order to assess the periodicity of the solution, the boundary conditions were repeated for three cardiac cycles.

Post-processing of this data was performed using EnSight 9.1.2, which was used to model particle traces under the application of magnetic forces. Cells were simulated as massed particles (m_p), which experience drag ($\boldsymbol{F}_d$) and magnetic forces ($\boldsymbol{F}_m$);

$$\boldsymbol{F}_d = -6\pi\eta R_c\left(\boldsymbol{v}_c - \boldsymbol{v}_f\right) \quad , \qquad \text{E.q. 6.4}$$

$$\boldsymbol{F}_m = \frac{N\, V_m\, M_s\, L(H)}{\mu_0}\left(\frac{\boldsymbol{B}}{|\boldsymbol{B}|}\cdot\nabla\right)\boldsymbol{B} \quad , \qquad \text{E.q. 6.5}$$

$$m_p\frac{d\boldsymbol{v}}{dt} = \boldsymbol{F}_d + \boldsymbol{F}_m \quad . \qquad \text{E.q. 6.6}$$

Constant magnetic forces between 12 and 120 pN were applied corresponding to an iron load of 15 - 150 pg/cell. The path of each magnetically labelled cell was traced at

each time step, displaying how the particle path would evolve under both fluid and magnetic forces.

6.2.7 Behaviour of a cell close to the arterial wall

A fluid structure interaction model was used to model the behaviour of a cell near a vessel wall. As this requires both the structural deformation and fluid-structure interaction, the explicit finite element code LS-DYNA was used. Fluid structure interaction modelling was performed by Kevin Lau (UCL mechanical engineering). A cell was modelled as an isotropic elastic body with a density of 1100 kg m^{-3}, Young's modulus of 10 kPa and a Poisson ratio of 0.45. A commonly reported Young's modulus for human umbilical vein endothelia cells[244] was chosen as no data for EPCs could be found.

A uniform inlet velocity of 0.01 m s^{-1} was applied which corresponds to the maximum value of the velocity at the top of the fluid domain assuming that the full velocity profile in the channel is parabolic. The simulations were run until a linear velocity gradient was formed across the inlet. Magnetic forces were applied to the cell by applying a uniform and constant force to each node in the cell, pulling it towards the wall.

Fluid-structure interaction was performed using a penalty coupling method, whereby the force applied to both fluid and structural domains was determined by calculating the level of fluid penetration into the solid domain. The fluid model of LS-DYNA is a compressible model and was defined with the following parameters: density 1080 kg m^{-3}, dynamic viscosity 0.0039 Pa s and a bulk modulus of 22 GPa. The value of the bulk modulus directly controls the maximum timestep in explicit time integration, thus in order to obtain simulations that runs in reasonable time frames this value was reduced to 1% of its true value, which was found to have no effect by comparing the numerical solution to the analytical solution of channel flow.

6.3 Results

6.3.1 Magnet optimisation

The maximum calf muscle radius measured for our patient group was 98 mm (see Table 2). We therefore choose a radius of 80 mm for our initial comparison of different magnet arrangements, as these would accommodate 90% of our population. As our patient group is limited it may not reflect the real variability of PAD patients, we therefore investigated the scalability of a magnet (see Figure 19).

Table 3: Leg dimensions for a small group of patients with peripheral arterial disease

n=40	radius below	maximum	radius above	radius ankle
mean ± SD [mm]	59 ± 10	60 ± 11	38 ± 7	43 ± 5
min [mm]	37	46	25	35
max [mm]	91	99	59	59

Figure 14 shows the average magnetic force acting on cells in the anterior tibial artery, posterior tibial artery and peroneal artery, for six magnet arrangements, with increasing magnet volume. For magnet volumes below 1000 cm^3, the magnetic rod, the Halbach cylinder k3 and the linear Halbach array generate a similar force. However for larger magnet volumes the Halbach cylinder k3 generates a stronger magnetic force than any other arrangement, followed by the Halbach cylinder k2. No change in magnetic force was notable above 10000 cm^3 from the magnetic triangle, magnetic rod, linear Halbach array or Halbach cylinder k4.

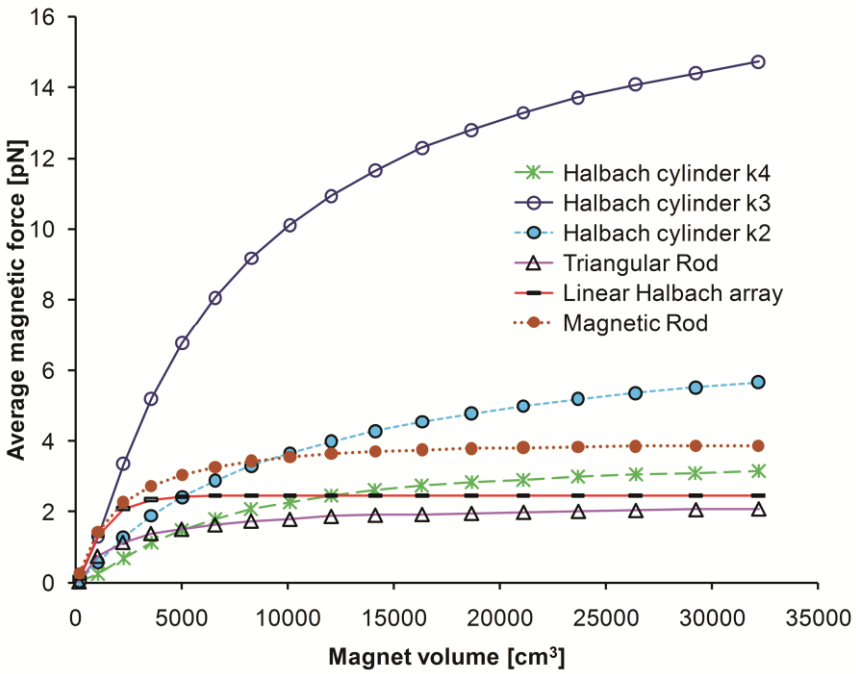

Figure 14: Average forces acting on magnetically labelled cells in the three major arteries of the human leg for different magnet arrangements with increasing magnet volume. All Halbach cylinders consisted of 12 elements while one magnetic rod and triangular magnetic rod were used. The linear Halbach array consisted of 5 elements.

Figure 15 shows the effect of multiple elements of basic magnet arrangements on the average magnetic force acting on a cell. The Halbach cylinder k3 again outperforms all other arrangements, provided it is constructed of more than six elements (see equation 6.1). For less than six elements, the magnetic rods are

superior, closely followed by linear Halbach arrays. A quadrupole arrangement (see equation 6.3) of magnetic rods comes closest to the Halbach cylinder k3 for more than six elements.

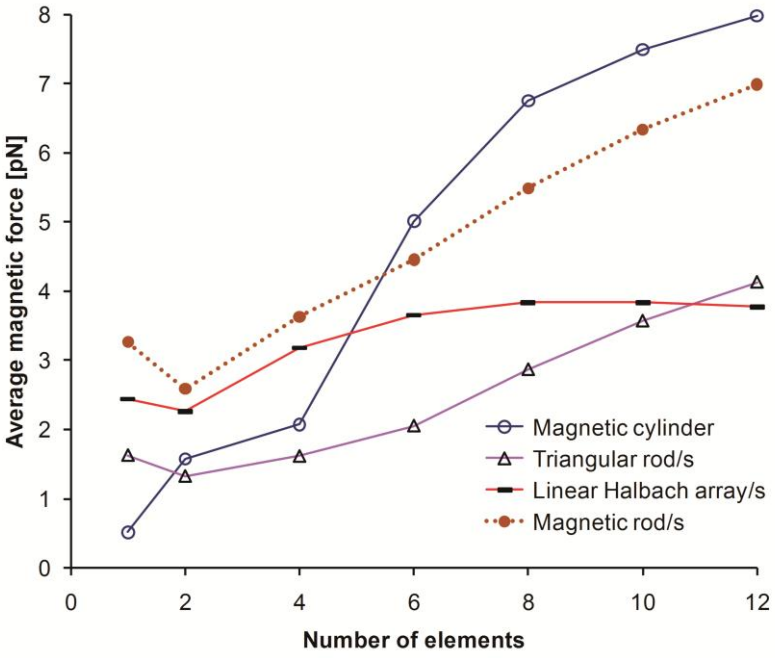

Figure 15: Average magnetic force produced by an increasing number of the basic geometrical magnet arrangements arranged symmetrically around the leg. The magnet volume is constant (6600 cm^3) for all of these arrangements. Note that for the Halbach cylinder the cylinder was not modified, only the number of elements it was divided into was changed. As outlined section 6.2.4 the magnetisation orientation of the Halbach cylinder follows k3 for more than 6 elements.

Figure 16 shows the force profile for a linear Halbach array and for the Halbach cylinders k3 and k4 across the centre of the air cylinder. Radial distances for blood vessels from the centre axis of the leg are shown as well to visualise the expected force for such radii. The mean distance between anterior tibial artery, posterior tibial artery, peroneal artery and the skin for three angiograms was 32 ± 7 mm. Note that the force produced by cylindrical magnet arrangements is rotationally symmetric while the force from the linear array continues to fall with increasing distance. The Halbach cylinder k3 produces a fairly constant force over a wide range of its internal radii due to its linear field gradient profile.

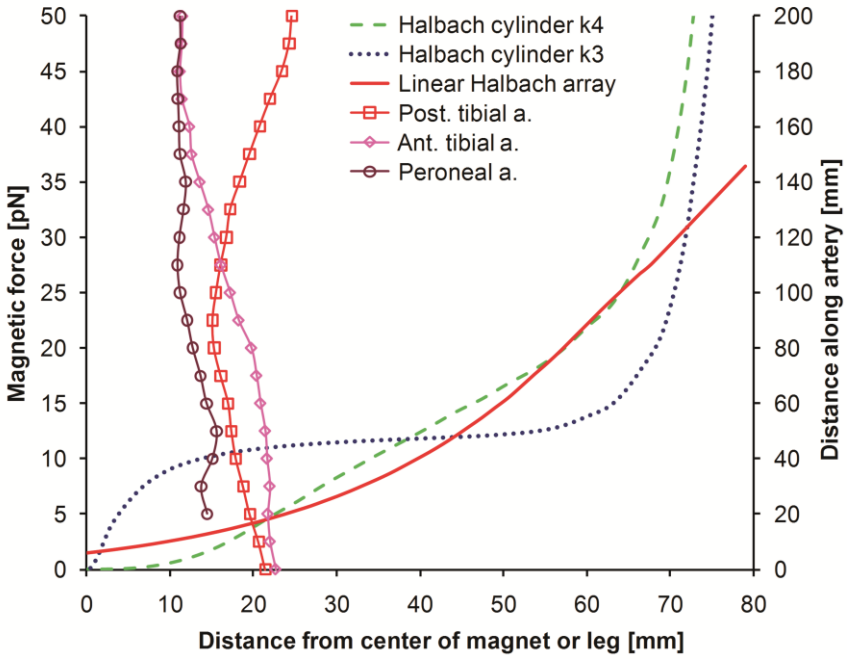

Figure 16: Example force profiles for different magnets using the same volume of magnetic material (6600 cm^3) All Halbach cylinders consist of 12 elements while the linear Halbach array consists of five elements. The radial position of the major lower leg blood vessels have been plotted to indicate their position within the magnet.

An infinite Halbach cylinder would have a perfectly symmetric field distribution. However, the finite length of real cylinders leads to flux loss at the ends and hence to decreased field and gradient strength. Figure 17 shows a comparison of different cylinder lengths for Halbach cylinders k3. Additionally the effect of endplates as outlined by Bjørk et al.[245] has been assessed. Vertical black lines have been drawn in Figure 18 to indicate the length of the blood vessel segments used for CFD simulations. All force profiles shown in this figure are for a line with a radius of 15 mm away from the centre. Increasing the cylinder length beyond the length of the vessel segment leads to considerable improvements in the homogeneity of the force. The use of endplates as indicated in Figure 18 has the benefit of minimising the use of magnetic material while increasing the force acting along the line. However, the linearity was not improved to the same degree as for the extended Halbach cylinders.

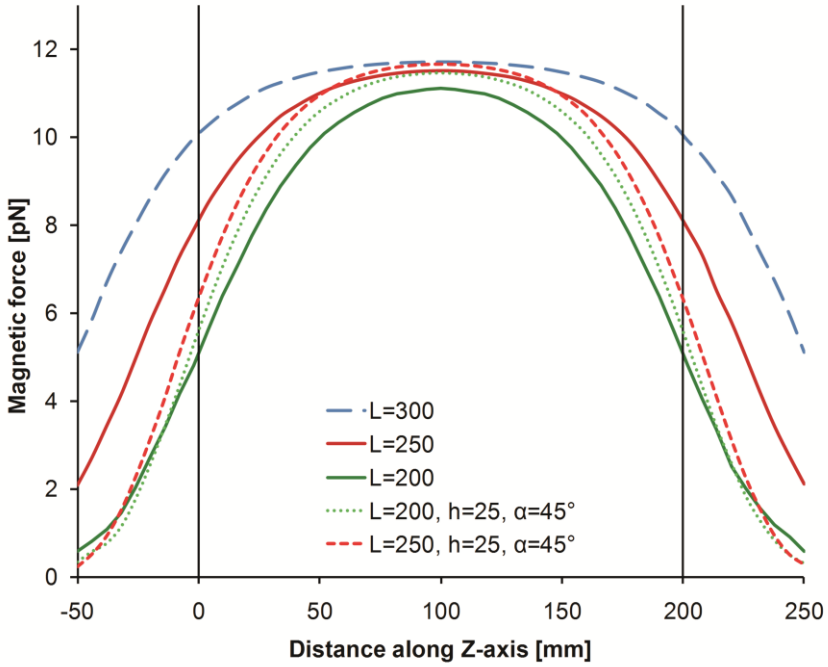

Figure 17: Linearity of the magnetic force along the z-axis of k3 Halbach cylinders with different lengths and endplates. The definition of the endplate height and the circumferential angle α are shown in Figure 18.

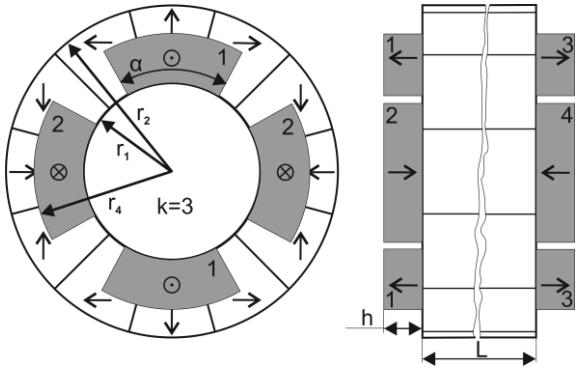

Figure 18: Geometrical arrangement of endplates on a Halbach cylinder k3. Endplates are made of the same magnetic material as the Halbach cylinder. Open arrows have been used to indicated the magnetisation orientation of the four endplates.

6.3.2 Scalability of magnetic forces

Two aspects of scalability are addressed in this study; changing the inner diameter of a Halbach cylinder k3 to accommodate different human leg diameters and secondly the scale down for an animal model.

Figure 19 shows the slow decline of the magnetic force as the inner radius is increased from 54 to 98 mm for Halbach cylinders k3 with a r_1/r_2 ratio of 0.62. Magnetic forces acting on cells for increasing leg diameters decrease from 14 pN to 6

pN. At the same time the necessary magnet volume increases from 4000 to 10000 cm^3.

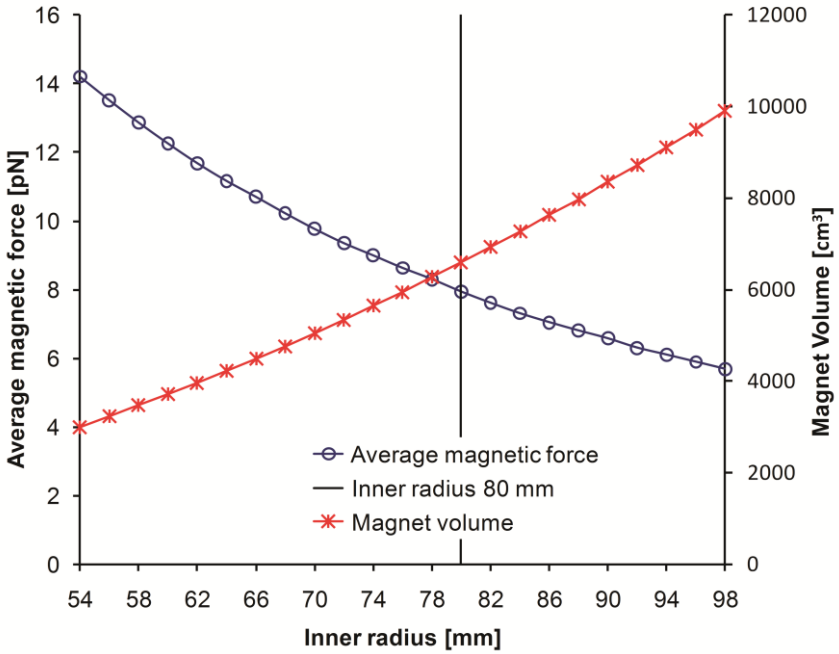

Figure 19: Average magnetic forces produced by Halbach cylinders k3 with different inner diameters illustrating the scalability for different human leg diameters. A constant ratio between inner and outer diameter of 0.62 was used for all Halbach cylinders. The black horizontal line indicates an inner radius of 80 mm corresponding to the sixth circle on the Halbach cylinder k3 line of Figure 14.

Figure 20 shows the force profiles along the radius for two Halbach cylinders k3. The first one has an inner radius of 80 mm and is made of neodymium iron boron while the second one has an inner radius of 25 mm and is made of sintered ferrite. The outer radius of the smaller cylinder has been adjusted in order to match the force acting on cells of the bigger cylinder. As the smaller cylinder is intended for a rabbit common carotid injury model, the radial distance of the right carotid from the neck centre line has been added. It can be appreciated that the forces acting on cells in the carotid artery would be similar to forces expected for the human lower leg arteries (see Figure 16).

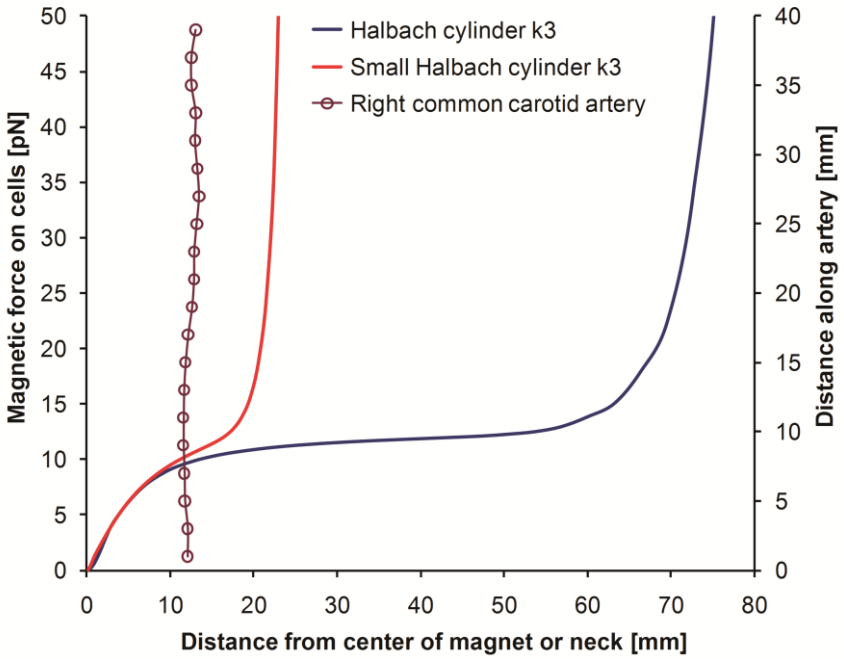

Figure 20: Force profile for a Halbach cylinder k3 and a scaled down version for a rabbit injury model. The radial position of the right common carotid artery has been plotted to indicate the force cells would experience along the centreline of the artery.

6.3.3 Magnetic attraction of cells to the arterial wall

Computational fluid dynamics modelling was used to investigate the behaviour of magnetically labelled cells in an artery with pulsatile flow and an external magnetic field. Figure 21 shows a small section of the mesh in the flow channel (approximation for the posterior tibial artery) and seed points which were used to release and track the movement of cells. Cells were seeded 20 mm inwards of the flow channel to avoid disturbances from the inlet.

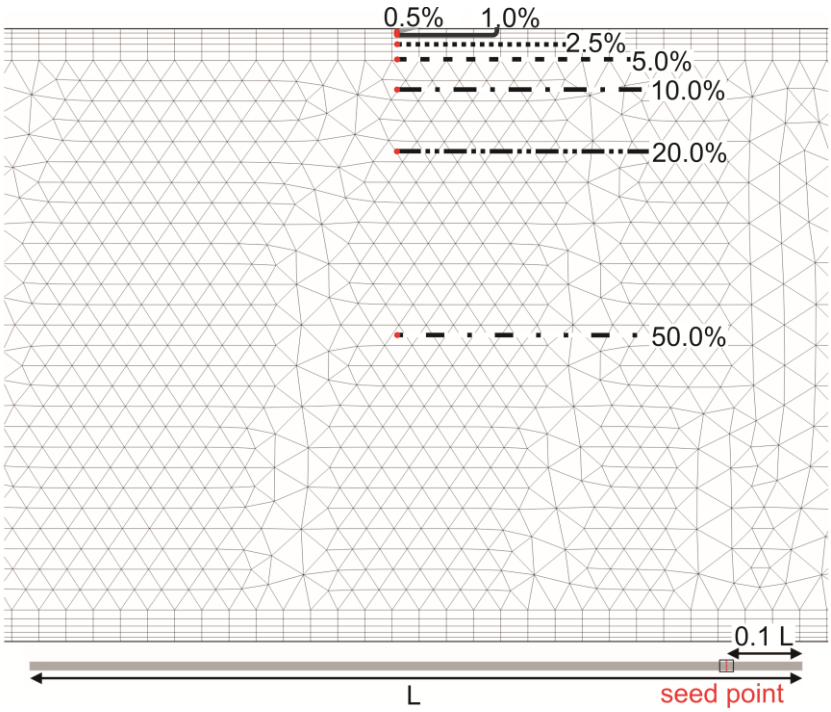

Figure 21: Close up of the meshed artery channel with the different cell seeding point indicated by red dots. The size of this section with respect to the whole artery channel is indicated by a black box at the bottom of the figure.

Figure 22A and C show the trajectories for cells experiencing a magnetic force of 48 pN (60 pg iron/cell) during maximum forward flow (A: towards foot) and backward flow (C; towards knee) respectively. Cells which are within 1% of the chamber radius from the wall will hit the wall, while cells released at 2.5% from the wall will not. Figure 22B and D show the trajectories for cells exposed to a magnetic force of 120 pN (150 pg iron/cell) along the x axis (up) as for A and C. Cells seeded at 0.5 and 1% from the wall contact the wall quickly (in one forward cycle) while cells seeded at 2.5% require both forward and backward cycles to contact the wall. For this case the total capture efficiency over one cardiac cycle would be 6.25% of all cells passing through the channel while a magnetic force of 12 pN per cell would lead to a capture efficiency of < 0.5%.

The plots in the centre between A-B and C-D show the flow profile for the inflow and outflow which have been used in these simulations; these were obtained from a 200 mm section of the posterior tibial artery from a single volunteer. Portions of these flow curves have been shaded to indicate the time points within a cardiac cycle for which the flow profiles are shown.

Capture efficiencies for magnetically labelled cells in the rabbit common carotid artery with an applied magnetic force of 12 pN and 120 pN per cell were < 0.5% and 100% over one cardiac cycle respectively (data not shown).

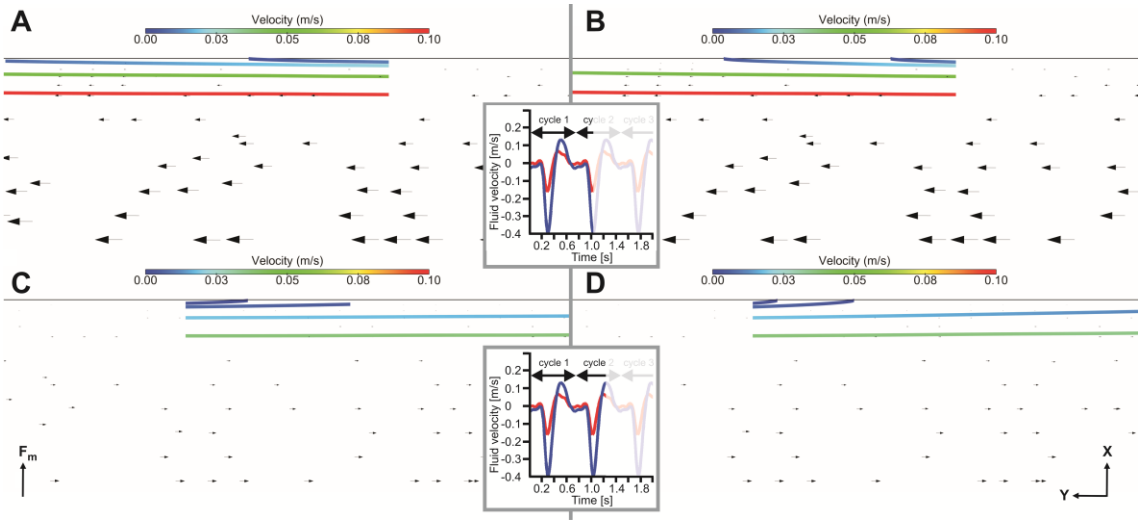

Figure 22: Trajectories for cells labelled with 60 pg iron per cell at the time of maximum forward flow A (towards the foot) and maximum backflow C are shown. Figure B and D show the trajectories for cells labelled with 150 pg iron per cell. The magnetic force is orientated up for all plots, as indicated by the arrow in the lower left corner. Other arrow heads indicate the velocity of the fluid, which are scaled in magnitude. The two plots in the middle show the inflow and outflow profile for a 200 mm anterior tibial artery section over three cardiac cycles, the current time point of the simulations indicated by the difference in shading. Plot A-B show the flow field 1 second after the first heart beat, whilst C-D show the flow field 1.3 second after the first heart beat.

6.3.4 Physical behaviour of a cell close to the arterial wall

Fluid-structure interaction simulations were performed to investigate the behaviour of a magnetically labelled cell close to the arterial wall as the resolution of the CFD simulations are insufficient to address this issue. A uniform magnetic force was applied on all nodes of the structural model of the cell while a constant boundary condition was applied for the fluid flow and allowed to evolve.

Figure 23 shows the mesh and the geometrical arrangement at the start of the simulation with the cell at 5 µm from the vessel wall. The magnetic force pulls the cell to the wall (contact occurs in < 0.05 ms) and together with fluid forces this leads to the flattening of the cell. Here friction between the cell surface and the wall has been neglected, which results in the cell rolling with minimal displacement along the channel (< 3 µm over 1 s). A snapshot for the fluid field at the rolling condition is shown in Figure 24.

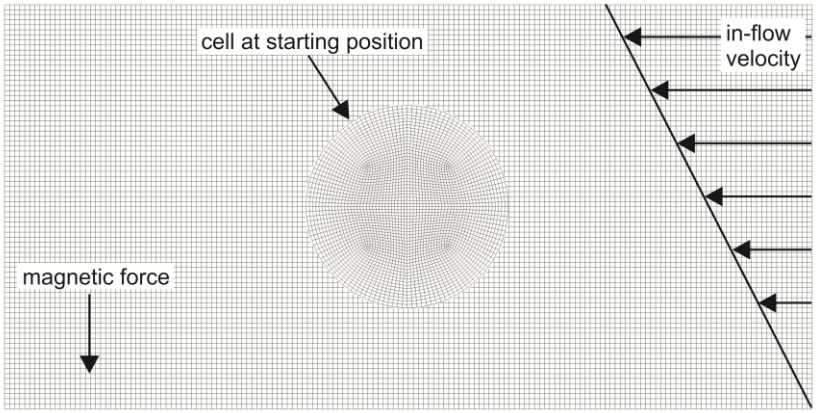

Figure 23: Finite element mesh of the cell (structure) and fluid used for fluid-structure interaction simulations. A constant fluid velocity is applied on the right side. Here the magnetic force is orientated downwards.

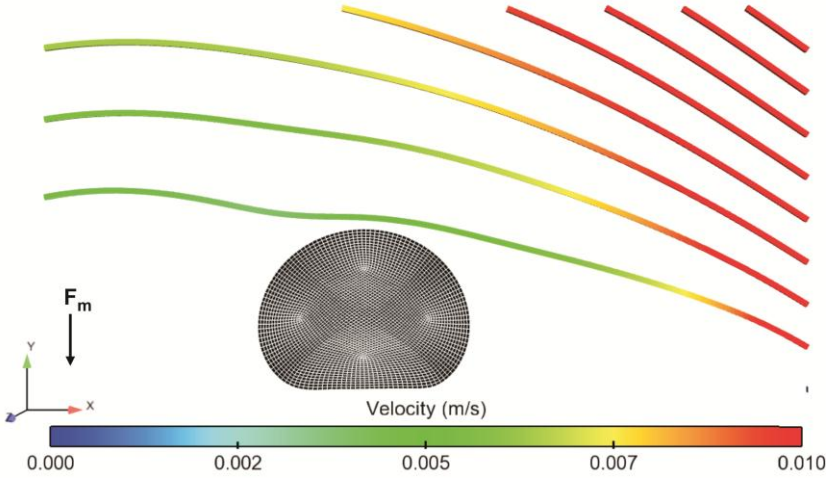

Figure 24: Fully develop fluid velocity field around the cell (0.4 sec after simulation start). The cell has been attracted to the wall and flattened by the magnetic force acting on the cell. The fluid forces result in the slow rolling of the cell during the simulation as the wall of the artery has been modelled as frictionless.

6.4 Discussion

Overcoming fluid forces is of major importance for most magnetic cell or drug targeting approaches. It is therefore important to optimise all important components involved such as cell labelling, magnet actuation device design and delivery protocol. Furthermore, any such study needs to follow a thorough parameter optimisation, which will be dependent on the geometry of the targeting tissue. While there is a lot of literature on particle optimisation[81;246-248] and cell loading[44;88], there is little material documenting magnet optimisation[112;245;249]. Additionally previous reports have only tested a small number of geometric arrangements.

The optimisations showed that for arteries in the legs, a Halbach cylinder k3 outperforms all other potential arrangements of permanent magnets. This would also be true for other arrangements where the arteries are not close to the skin. It is advantageous that Halbach cylinders produce fields with rotational symmetry as this makes positioning of the magnet straightforward. Linear field gradients produced by the Halbach cylinder k3 led to constant forces over a wide range where the magnetic particles are fully magnetised. However, this comes with the drawback that the force will fall to zero close to the centre. If a human leg is centred in a Halbach cylinder, the peroneal artery will be closest to the centre and can cross the centre line (data not shown). This is not desirable as cells might be washed away but clinical experience suggests that the reendothelialization of the posterior and anterior tibial artery is of greater importance[20]. Hence it might be acceptable to have some areas of the peroneal artery where magnetic cell delivery would be less efficient.

As mentioned above, fluid forces are a major obstacle for magnetic cell and drug targeting. Consequently, it is important to consider them during the optimisation process. CFD offers interesting opportunities to study magnetic targeting in fluids. This approach has previously been used for the targeting of magnetic particles in experimental arrangements[121;236;250], but has not been combined with patient derived geometry and blood flow data for the purpose of cell targeting. The CFD model in this study was built from MR data which allowed the theoretical assessment of cell targeting efficiency for the human lower leg arteries. For a healthy volunteer the fluid forces were dominant and led to a targeting efficiency of 6.25% for strongly labelled cells. Cells which were close to the vessel wall (< 0.5% of the radius) were attracted during peak flow even when they experienced only a magnetic force of 12 pN. Only first pass capturing has been considered as cells returning with the venous blood to the heart would are likely to be captured in the lung.

In patients with PAD, it is likely that the blood flow rates are lower due to their condition. Additionally cell aggregation due to dipole interactions at the magnetic flux density used is likely to increase targeting efficiency. Nevertheless the best delivery protocol might be to stop blood flow for 5 minutes while cells are delivered via a catheter which is being retracted. This would increase the targeting efficiency to almost 100%. The leg would be placed in the centre of the magnet during cell delivery and kept there for another 30 min to allow cell attachment to the artery; such an approach should be acceptable from a clinical perspective. This initial cessation of

blood flow would allow cells to be attracted to the vessel wall. On reperfusion, the low fluid velocities close the boundary permit the magnetic forces to overcome the drag force and thus prevent cells from washing away. Another point which needs to be considered is that due to the positions of the arteries relative to the centre of the Halbach cylinder, cells would be attracted to a half circle of the vessel wall covering about 50% of the vessel inner surface. Cells would have to spread out to cover the remaining area.

The strength of the magnetic forces generated is also dependent on the cell labelling. All magnet optimisations were performed assuming a cell loading of 15 pg iron per cell, which is an amount that has previously been achieved[117]. For some of the CFD simulations were performed with cells loaded with 150 pg iron. Labelling concentrations between 10-300 pg iron per cell have been reported previously[230] which indicates that such labelling efficiencies should be achievable. However this requires to be tested for the cell line under investigation.

In order to get a better idea of how cells might behave in the boundary layer of the vessel wall, a fluid-structure interaction approach was used. The simulation of a single elastic cell being attracted to a surface by magnetic forces acting on each vertices and fluid flow around the cell led to the flattening of the cell. This flattening together with the magnetic force was sufficient to prevent the cell from flowing away but it did not stop the cell from slowly rolling along. Such behaviour is not surprising as the vessel wall has been modelled as frictionless. However this abstract model highlights that a cell can be held at the vessel wall with magnetic forces generated by the selected magnet arrangement. Realistic wall friction and surface receptors on the cells themselves will likely generate friction and increase the strength of the cell attachment to the vessel wall impeding the cells from rolling along. The contact area between cell and vessel wall for the deformable cell would be 30 μm^2 while the contact area for the case of a rigid sphere is essentially a point, resulting in less friction and a less positive outcome in cell attachment.

One of the major problems for the development of magnetic targeting applications is the poor scalability of magnets. This is a consequence of the inverse square law behaviour of magnetic fields, which makes it easy to generate sufficient force at the scale of a small animal but very difficult to do this for a human. This problem has not been addressed sufficiently in the magnetic targeting literature as many experiments performed on small animals cannot be scaled up[114;122]. Nevertheless

if theoretical optimisations are first performed with realistic human geometry and blood flow data, a scale down can be possible. The best performing magnet design in this study could be scaled down for a rabbit arterial injury model such that the forces acting on the cells would be similar to those generated for human arteries. However, force linearity is limited to a smaller range and blood velocities can only be adjusted by selecting an appropriate artery. This choice is additionally restrained by biological considerations.

CFD simulations for the rabbit carotid artery showed that cell capture efficiencies under flow are higher than those estimated for human lower leg arteries. This is mainly due to the lower mean flow rate and the lower diameter. Even so, the scale down would still be valid as the blood flow would have to be stopped for five minutes in the rabbit also. As for the human case, cells would have reached the boundary layer in this time where the magnetic forces would dominate the fluid forces. In this boundary layer, the behaviour of cells would be similar for human and rabbit arteries.

6.5 Conclusions

For the best performing magnet arrangement (Halbach cylinder k3) in this study, the targeting efficiency for all cells passing through the posterior tibial artery during one heart beat was 6.25 % (first pass capture). However, if the flow is stopped for five minutes a targeting efficiency of close to 100% could be achieved as magnetic forces would be strong enough to attract and hold cells at the vessel wall potentially increasing cell efficacy. Finally, this magnet can be scaled down for a preclinical rabbit injury model without changing the magnetic force acting on the cell. This leads to similar behaviour in the boundary layer close to the vessel wall, thus enabling development and testing of clinically relevant magnetic cell targeting approaches in an animal model.

7 Magnetic cell tracking using MRI

The aim of this chapter is to illustrate the application of MRI for the tracking of magnetically labelled cells. Cell tracking using MRI can aim at tracking individual cells which are strongly labelled or populations of cells that are weakly labelled. Both of these applications will be illustrated by a tissue engineering example with a detection limit of less than 10 cells and an in vivo example with a detection limit of approximately 10,000 cells. The tissue engineering example refers to a project in collaboration with Richard Day (UCL Centre for Gastroenterology & Nutrition) for who I did only perform the MRI imaging and data analysis. Cell tracking in the rat heart was part of a project with Paolo De Coppi (Institute for Child Health (ICH) - Surgery Unit, UCL) to characterise the therapeutic potential of rat amniotic stem cells. For this project I performed cell labelling, surgery, MRI imaging and data analysis.

7.1 Introduction

Labelling cells with superparamagnetic particles increases their magnetic susceptibility. If these cells are placed into the magnetic field of an MRI scanner they become magnetised and induce local variations in magnetic flux density. Such variations in magnetic field homogeneity lead to increased spin-spin relaxation (see chapter 3) causing hypointensity on T_2 or T_2* weighted images.

Superparamagnetic particle suspensions (ferrofluids) have been approved as contrast agents for the detection of liver and kidney tumours. These contrast agents and other SPION have also been used to label cells for in vivo tracking after administration in animal models[92;174;185;186;189;195;198] and humans[103;110;111]. Such studies showed that cells containing or associated to (bound or absorbed to cell surface) a high amount of iron oxide 200-1000 pg a single cell can be detected on MRI images with suitable parameters in organs that have a low natural variation in magnetic susceptibility such as the brain[198]. Imaging voxels in such cases are typically in the 50 to 100 micrometer range for preclinical systems while cells have a diameter of approximately 10 micrometer. Detection of these small particles is possible because spin-spin relaxation is accelerated up to 100 micrometer away from a particle if the time to echo is sufficiently long (TE, an MRI sequence parameter, see chapter 3).

However, it is also possible to track cells in organs which are more difficult to image such as the moving heart. But for these cases the detection limit is in the range of 10 000 cells. This has been demonstrated in studies where weakly labelled cells (< 15 pg iron oxide per cell) have been tracked in the heart[10;188].

Another application for which MRI tracking of labelled cells has been proposed is the non-invasive assessment of tissue engineered products which contain magnetically labelled cells. An example for that is given by Perea et al.[143] in a study where magnetically labelled cells were seeded onto a vascular scaffold using an electromagnet. MRI was used as quality control for the uniformity of cell seeding. Another application showed the tracking of labelled cells in tissue engineered cartilage[251].

The first section of this study aims to investigate the feasibility of longitudinal tracking of labelled stem cells in the rat myocardium after myocardial infarction (MI). This is part of an on-going collaboration with Paolo De Coppi (Institute for Child Health (ICH) - Surgery Unit, UCL). De Coppi's laboratory is working on molecular mechanisms

of cardiac repair after myocardial infarction. As part of this collaboration I have performed the surgery to introduce myocardial infarction in rats as well as cell labelling, MRI imaging and data analysis. While the second section will test the feasibility to determine cell distributions after magnetic cell seeding on scaffold membranes and decellularised intestine samples. This is part of an on-going collaboration with Richard Day (UCL Centre for Gastroenterology & Nutrition). For this project I did only perform MRI imaging, data analysis and finite element analysis of magnetic fields.

The hypotheses for these experiments were:

- MRI can detect magnetically labelled cells in the rat myocardium and track them over time.
- MRI can be used for the non-invasive assessment of magnetically delivered cells on membrane and intestine scaffolds.

7.2 Materials and Methods

7.2.1 Labelling of rat amniotic fluid stem cells

Rat amniotic fluid stem cells (rAFSCs) were used for this study. AFSCs are sometimes referred to as amniotic MSCs and are similar to the cells used in chapter 4. Cells were cultured *in vitro* for 48 hours in Chang medium and then labeled with Endorem (Guerbet Laboratories Ltd, UK). Cells were incubated with Endorem SPION (20 µl/ml of cell medium) for 24 hours at 37°C and then detached using a 0.05-0.02% w/v trypsin sodium-EDTA solution. The labeling concentrations of SPION used were selected to preserve > 95% viability (data not shown). Cell viability after cell labeling was monitored via trypan blue exclusion. For cell delivery, $5x10^6$ Endorem-labeled rAFSCs were re-suspended in 100µl PBS 1X.

7.2.2 Rat myocardial infarction model and cell transplantation

The animal study was approved by the Ethics Committee of the University College London, UK. All surgical and pharmacological procedures were performed in accordance with the animals scientific procedure Act 1986 (Home Office UK). Procedures were carried out by myself PIL 70/21740 under the my project licence PPL 70/7114.

Wistar rats (Harlan Ltd., UK) weighing 250-300g, housed and maintained in a controlled environment, were randomly assigned to the cell injection with myocardial infarction (MI), cell injection without myocardial infarction (Sham) and a control group with myocardial infarction and PBS injection.

Animals, anesthetised with an intraperitoneal injection of 50 mg/kg body weight of ketamine hydrochloride (Vetalor, Parke Davis, NJ) were maintained on a heating blanket during surgery at 37°. An endotracheal tube was inserted into the trachea and artificial respiration with pure oxygen was provided via a Respirator (Harvard Apparatus Ltd., U.K.; 70 strokes/min, tidal volume 8-10 ml/kg). The myocardial infarction was performed as follows: the left pectoris major muscle and muscles below were dissected and a cardiac access procured via thoracotomy performed in the 3rd or 4th intercostal space. The pericardium was removed and the left anterior descending coronary artery was occluded (LAD ligation) close to its origin with a snare occluder (Mersilk suture 5-0, Ethicon, Johnson & Johnson Ltd. Kirktion, UK) for 30 minutes. For the Sham group, the suture was put around the LAD but the LAD was not occluded. The occlusion was removed and the myocardium re-perfused. After re-perfusion, labeled cells or PBS control was injected at three sites (33 µl per site) in

the border zone of the infarct using 31 gauge needles. In the sham group, injections were positioned similar to the MI group. Animals were then fully recovered and analgesic (buprenorphine, Vetergesic, 0.25mg/kg Alstoe Ltd, UK) was supplied via intraperitoneal injections.

7.2.3 Serial MRI of infarcted rat hearts

Animals were subjected to MRI imaging one, two and three weeks after surgery. Rats anesthetized with isoflurane 4% (in pure oxygen) and maintained at 2%, were placed together with a heating blanket supine on an animal holder. A respiration sensor and a cardiac phased array coil (Rapid Biomedical GmbH, Germany) were placed on the chest. Needle electrodes were inserted subcutaneously into the front limbs to record the electrocardiogram (ECG). For cardiac and respiratory gating a MR monitoring and gating system (SA Instruments Inc., NY) was used.

Cardiac imaging was performed with a 9.4T (400 MHz) horizontal bore system (Agilent Technologies, Palo Alto, CA) with a shielded gradient system (400 mT/m). A short axis image series perpendicular to the long axis orientation was acquired. In order to cover the whole left ventricle from apex to base 15 - 20 short axis slices were acquired without a gap. A segmented gradient echo sequence was used with the following imaging parameters; TE ~1.7 ms, TR ~7.5 ms, FA 15°, FOV 40x40 mm², slice thickness 1 mm, Matrix size 192x192. Twenty time frames were recorded for every cardiac cycle. A short axis slice was obtained in approximately 45 seconds leading to a total scan time for one heart of 10 to 15 minutes. Segment (http://segment.heiberg.se) was used to analyze the data and calculate the ejection fraction. The same sequence and settings were used for cell tracking but only a single frame at the end diastolic time point was acquired.

7.2.4 Labelling of cells and magnetic seeding with a Halbach cylinder

Labelling and magnetic seeding of cells was performed by Jordi Gonzales-Molina (Centre for Gastroenterology & Nutrition, UCL). Nuclepore polycarbonate membranes (Whatman, UK; 25 x 80 mm, 10 µm thick) were rolled and inserted into 50 ml Falcon tubes resulting in coverage of the lumenal surface of the tube. The membranes were then coated with 10 µg/ml fibronectin (Sigma-Aldrich).

A 20 ml cell suspension of $1x10^6$ L929 cells loaded with SPION after 24 hour pre-incubation in medium containing 125 µg/ml SPION (fluidMAG-UC/A anionic

charged SPION; 50 nm particles with a magnetite core suspended in water; Chemicell GmbH, Berlin, Germany) was added to the Falcon tubes containing the polycarbonate membranes. The tubes were placed vertically into the Halbach cylinder (see Figure 25) and incubated at 37°C for 2 hours.

For dynamic rotational cell seeding, $1x10^6$ SPION labelled L929 cells were added to 20 ml MEM in Falcon tubes containing fibronectin-coated polycarbonate membranes. The tubes were placed horizontally onto a support and incubated at 37 °C for 30 minutes before rotating 90° along the horizontal axis. The rotation process was repeated three times in total, resulting in a total incubation period of 2 hours.

After incubation, the polycarbonate membranes were gently washed once with 30 ml PBS to remove non-adherent cells and fixed with 2% formaldehyde in 0.1 M PBS (VWR International Ltd, Lutterworth, UK) for 10 minutes.

The feasibility of applying the Halbach cylinder device (see Figure 25) to the delivery of cells to gastrointestinal tissue was qualitatively evaluated using segments of porcine jejunum obtained from an abattoir. After cutting the specimen into 70 mm lengths, the mesentery was trimmed away and the lumen rinsed several times with PBS before being inverted to expose the mucosa. The mucosal surface was mechanically denuded by scraping with the edge of a glass microscope slide before rinsing with PBS. The jejuna segments were re-inverted before being positioned into 50 ml Falcon tubes with stents inserted 1 cm into the ends of each segment so that the lumen remained open.

The tubes were filled with 50 ml of complete medium containing a suspension of $1x10^6$ L929 cells pre-incubated with medium containing 125µg/ml SPION for 24 hours. The tubes were loaded into either the Halbach cylinder (see Figure 25) and incubated for 2 hours at 37°C 5% CO_2 or placed horizontally onto a support and incubated at 37°C for a total 2 hours, with 90° rotation every 30 minutes, as outlined above. After incubation, the culture medium was removed and the lumen of the jejunum gently washed once with PBS to remove unattached cells, followed by fixation in 2% formaldehyde solution for 24 hours.

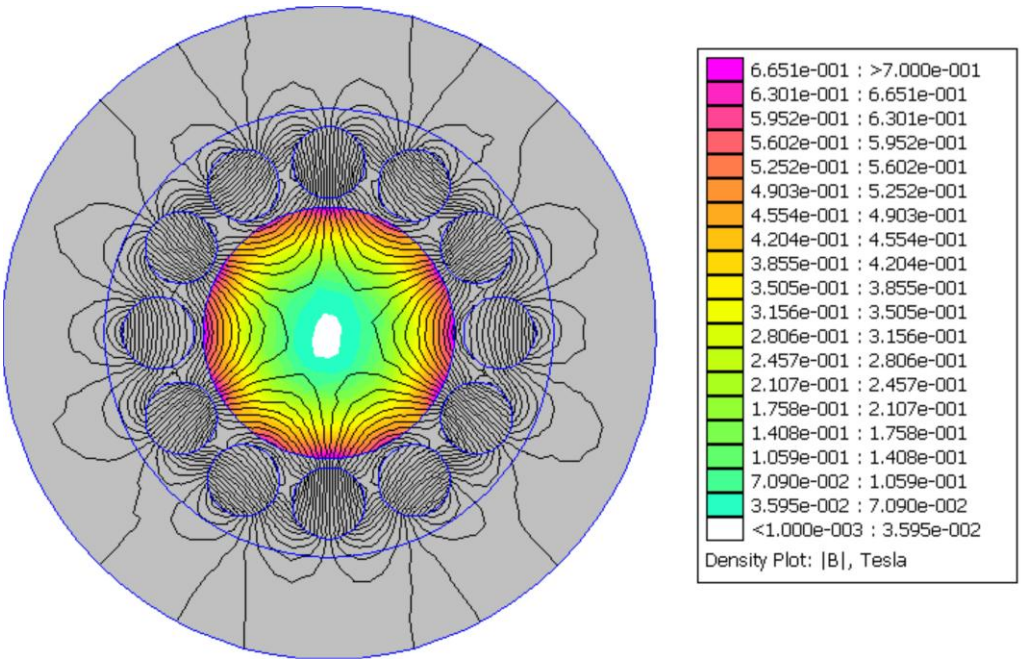

Figure 25: The magnetic seeding device consisted of a bespoke Halbach cylinder (k4 variety; 12 elements with 120 degree rotation steps for the magnetisation orientation; manufactured by Magnet Sales, Swindon, UK). A cylinder (internal dimensions: height: 85 mm, diameter: 30 mm) was machined from a solid block of aluminium to hold a 50 ml Falcon tube. 12 magnetic rods (neodymium-iron-boron magnet NdFeB N48M, remanence magnetisation 1.43 T, intrinsic coercivity 1120 kA/m length: 75 mm and diameter: 8 mm) were equally spaced around the wall of the cylinder.

7.2.5 Estimation of cell distribution after magnetic cell seeding

Magnetic resonance imaging (MRI) was used to qualitatively evaluate the distribution of SPION labelled cells on polycarbonate membranes and denuded jejunum samples (as an example for magnetic cell seeding to thick-walled tissue). The lumen of the tubes containing polycarbonate membranes or denuded jejunum was filled with 1% low melting point agarose (Fermentas Ltd., Hanover MD, USA) containing 8 mM of Gadolinium-DTPA (Magnevist, Bayer AG, Berlin, Germany).

Imaging was performed on a horizontal bore 9.4 T DirectDrive VNMRS system (Agilent Technologies, Palo Alto CA, USA) using a 35 mm quadrature birdcage volume coil (RAPID Biomedical GmbH, Würzburg Germany). For 3D imaging, a gradient-echo sequence with the following parameters was used: TE 6 ms, TR 25 ms, flip angle 60°, 3 averages, field of view 35x29x29 mm, matrix size 1000x828x828 leading to an isotropic voxel size of 35 µm.

Segmentations and 3D renderings were performed using Amira visualisation software (v5.2.2, Visage Imaging Inc., Andover MA, USA). The cross-section of the tubes was divided into four segments. For each of these segments, hypo-intense regions indicative of high iron content were segmented using thresholds. Volume rendering without smoothing was performed for all segments and the hypointensity volume was recorded.

7.3 Results

7.3.1 Longitudinal tracking of labelled cells in the infarcted myocardium

Imaging the heart poses additional difficulties as MRI is very sensitive to motion. In order to avoid motion artefact fast imaging sequences which are synchronised to the heart and breathing frequencies have to be used. This limits the amount of T_2 / T_2* weighting that can be used. However, labelled cells can be detected if a sufficient amount of cells is injected. Figure 26 A-C shows mid-ventricular images for a rat at one (A), two (B) and three (C) weeks after surgery. White arrows indicate the regions where cells were injected. Although there is a slight variation in the exact slice position the persistency of the hypointesnisty can be appreciated. Control images for a heart with PBS injection are shown for one (E) and three (F) weeks after surgery. The red arrow on image (F) indicates a potential limitation of this technique, hypointensity due to hemosiderin (a blood breakdown product). Hypointensites can be segmented with localised threshold to estimate the distribution volume of labelled cells and to visualise cell distribution (see Figure 26D).

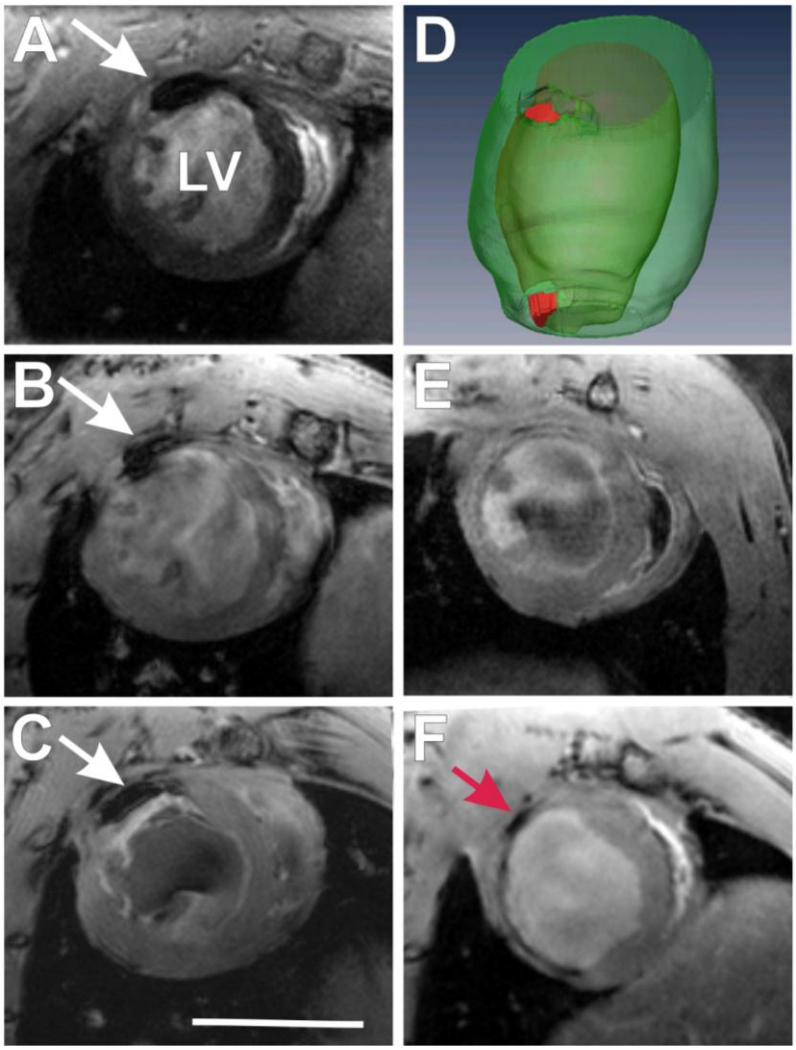

Figure 26: In vivo cardiac MRI images of infarcted hearts after cell transplantation. Images of magnetically labelled cells injected into the border region of the infarct in a rat heart. Images were acquired at one (A), two (B) and three (C) weeks after cell transplantation. The white arrows point towards the hypointensities caused by injected cells. The scale bare on panel (C) is one centimetre. Local thresholds have been used to segment the area containing cells to visualise their distribution in 3D (D). Control images for a heart with PBS injection are shown for one (E) and three (F) weeks after surgery. The red arrow on image (F) shows a hypointense region on a control image which is most likely due to blood breakdown products.

Serial imaging of transplanted cells allows for the assessment of cell migration and cell death. Figure 27 shows the changes in hypointensity volume over time. Hearts which did not have an infarct (Sham group) showed lower initial cell retention compared to hearts with infarcts (MI group). A general trend indicating a slow decline in signal void volume can be appreciated. This decline in hypointensity volume is similar for infarcted and non-infarcted hearts.

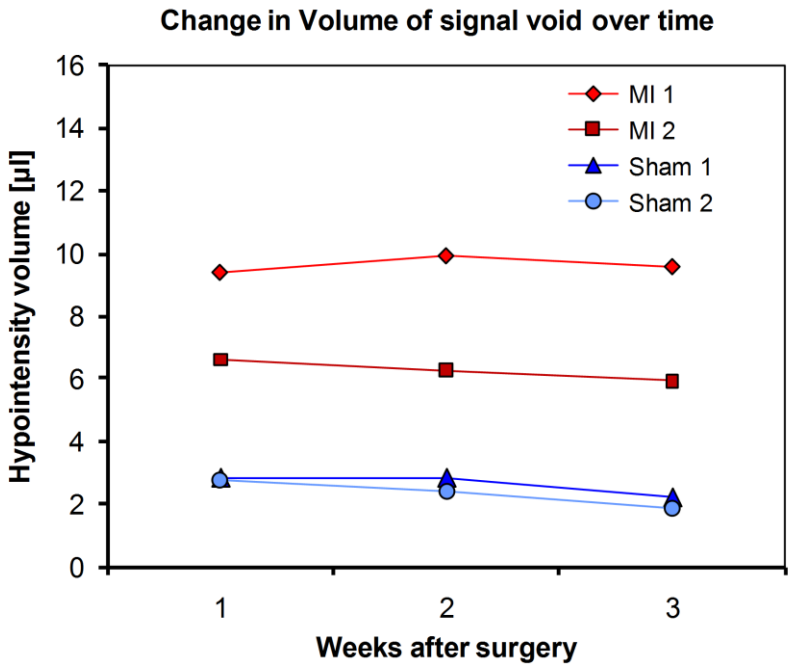

Figure 27: Signal void volume (volume of hypointensity over time) for hearts which received cell injections. Rats in the MI group had an infarct (> 20% loss in ejection fraction) while rats in the Sham group did not. Infarcted hearts retained more cells initially compared to Sham but the decline in the number of voxels with hypointensity is similar for both groups. Non error bare are shown for this pilot data as each data point is from a single measurements.

7.3.2 Cell distribution after magnetic cell seeding

For cell seeding with the Halbach cylinder, the signal void volume for different segments of the polycarbonate membrane was fairly similar, whereas in the dynamic rotational seeding group an accumulation in the segments initially facing down was observed (see Figure 28). Membranes with cells attached after delivery by dynamic rotational seeding revealed reductions in the amount of SPION labelled cells delivered in each quadrant corresponding with each subsequent rotation of the membrane. This pattern can be seen on MRI image slices but becomes more obvious for segmented 3D rendered volumes (see Figure 28 and Table 4).

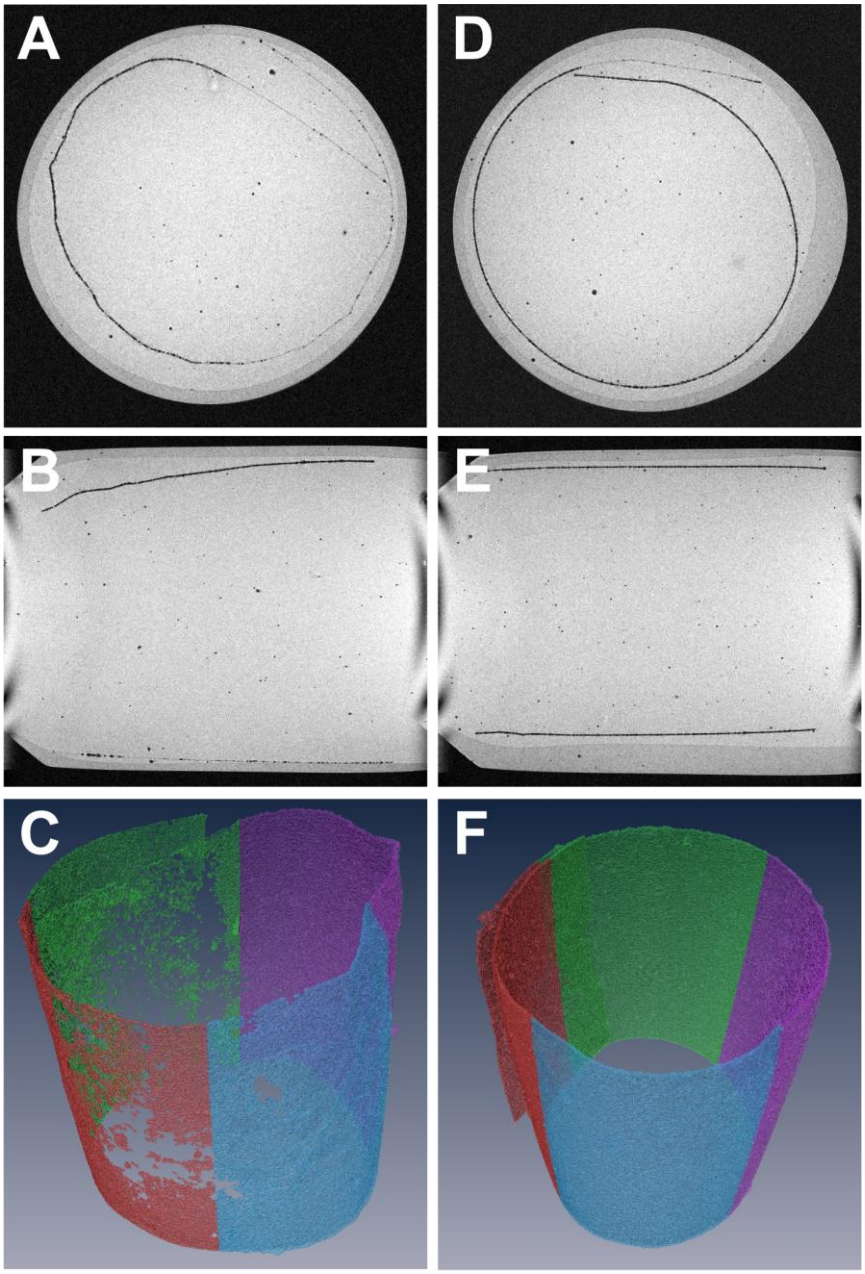

Figure 28: MRI images and pseudo coloured segmented 3D renderings of hypointensities. (A) and (B) are axial and coronal images of the polycarbonate membrane where cells have been seeded with the dynamic rotation approach. (C) shows a 3D rendering of the segmented hypointensities. The initial position for dynamic cell seeding was between the blue and the purple coloured segments. (D), (E) and (F) are the corresponding images for magnetic cell seeding with the Halbach cylinder.

The feasibility of using a Halbach cylinder to the delivery of cells to thick-walled tissue samples was assessed using denuded porcine jejuna. Qualitative assessment by MRI of the distribution of cells attached the tissue revealed a uniform pattern of distribution similar to that observed with the polycarbonate membranes, whereas a non-uniform distribution of cells was observed with the sample loaded by dynamic rotation cell seeding (see Figure 29 and Table 4)

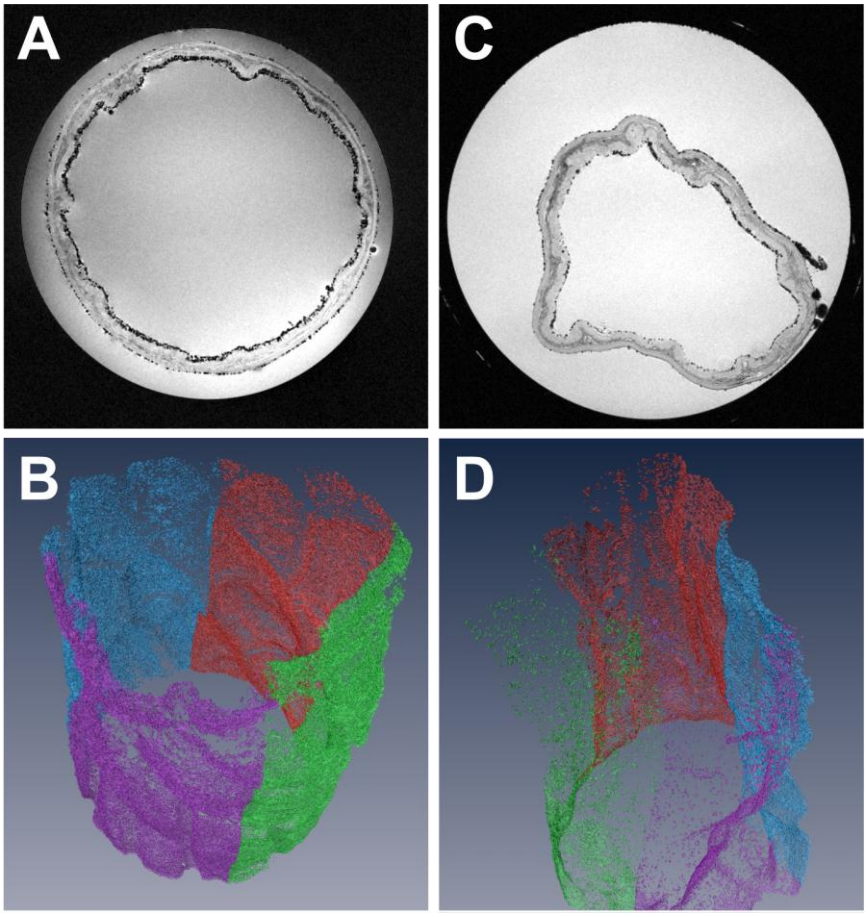

Figure 29: MRI images and 3D renderings of cells seeded onto porcine jejuna. (A) and (C) show axial images for magnetic seeding with a Halbach cylinder and dynamic rotation seeding respectively. (B) and (D) show the corresponding volume renderings of segmented hypointensities.

Table 4: Cell distribution after magnetic and dynamic rotational seeding

	% total SPION loaded cells/sector			
	Purple	Blue	Red	Green
Halbach cylinder membrane	25.8	23.2	25.0	26.0
Dynamic rotational seeding membrane	42.7	34.1	14.0	9.1
Halbach cylinder jejuna	24.6	20.7	27.0	27.7
Dynamic rotational seeding jejuna	13.4	47.0	28.2	11.4

7.4 Discussion

7.4.1 Cell tracking in the infarcted rat heart

The feasibility of magnetic cell tracking in the heart of small animals and humans has been demonstrated previously[10;186;202;220]. However, the image resolution of some of these studies was relatively low. Additionally only Stuckey et al.[220] performed volumetric analysis of the hypointensity regions. Such measurements can be used for a more precise initial assessment of the success of cell injections. It has

previously been reported that T_2 / T_2* weighted images overestimate the number of cells present in an area due to resident macrophages tacking up the SPION of dead cells[186;187;252]. Histological analysis at the end of this current study (outlined in section 7.2.2) found only a small amount of rat amniotic fluid stem cells. This indicates that the observed MRI signal may have originated primarily from macrophages that took up free iron oxide particles. However MRI is still useful to estimate the amount of cells initially delivered and retained. It is particularly important to relate therapeutic outcome to the amount of cells successfully delivered. For example, out of 4 sites in the rat heart into which cells have been injected, less than 3 sites seem to have retained cells directly after delivery[187]. This is due to the small myocardial wall in small animals which makes direct tissue injection difficult due to cardiac motion. In this study a lower initial retention efficiency of labelled cells was observed for sham operated hearts (see Figure 27) which is in agreement with previously published data[187]. This is most likely due to the higher interstitial pressure of actively contracting myocardium. Even if MRI overestimates the amount of cells present, it may still allow estimating the time course of cell clearance over longer time periods as shown in graft rejection models[189]. Also as mentioned in section 2.2.4, MRI offers the highest spatial resolution for cell detection and can be combined with a different imaging modalities, which allow for the direct assessment of cell viability such as PET, bioluminescence or near infrared imaging[173-175;177;179;181]. A major advantage of MRI is its non-invasive nature which allows for serial assessment of cardiac function[253-255] and cell locations. Additionally cardiac MRI is more accurate and has a higher reproducibility particular for infarcted hearts[256] as well as a higher spatial resolution for cell tracking compared to SPECT and PET[173;192;215].

The problem of false positive detection of labelled macrophages has received some attention and a combination of R_2 ($1/T_2$) and R_2* ($1/T_2$*) mapping has been proposed as a possibility to differentiate between particles internalised in labelled cells and free particles[195], although this has not been assessed for cardiac imaging. There have also been reports about biodegradable iron oxide particle aggregates which lead to significant relaxation changes due to reduced aggregate sizes[257]. It might be possible to exploit this if the linker between the particle can be made specific enough such that it is only degraded once internalised by macrophages. However, neither of these two options has been evaluated in the current study.

Another problem frequently encountered in the context of cell delivery is the detection of hypointensities due to blood breakdown products[196;197]. Differentiating between them and cells labelled with small amounts of SPION is particular challenging. Positive contrast sequences and susceptibility mapping might be able to resolve this[200;204]. However, it is to be seen if these approaches can be made fast and robust enough for cardiac imaging. MRI can also be used for the tracking of cells labelled with T_1 contrast agents[258]. However, these T_1 based contrast agents are generally not compatible with the T_2/T_2* effects of iron oxide particles used for magnetic delivery and are hence not discussed. The short echo times used in this study show that T_1 weighting would not produce positive contrast even if cells would contain a substantial amount of a T_1 contrast agent.

7.4.2 Cell tracking for tissue engineered scaffolds

Our study shows that MRI can be used for the non-destructive assessment of cell distributions in tissue engineered scaffolds with high spatial resolution. This potential for non-destructive quality control has been demonstrated previously[143;251]. However, these previous examples used fairly low resolutions and could not detect less than a few thousand cells in a voxel. The possibility of using MRI to detect single cells labelled with micron sized iron oxide particles has been demonstrated previously for carefully prepared agarose phantoms[259]. Our results show that small number of cells labelled with iron oxide nanoparticles can detected if the imaging time is sufficiently long. A potential advantage is that MRI could also be used to acquire additional information such as fibre orientation or elasticity provided the susceptibility artefacts due to labelled cells do not interfere in the same scan session. Estimating cell distribution in tissue engineered scaffolds is particular suitable when magnetic targeting or seeding has been used to position cells.

As outlined in the introductory section 2.2.4, a major disadvantage for MRI based cell tracking is the inability to assess cell viability and differentiation status. Although reporter genes for MRI detection of cell viability and differentiation have been developed[205;207;208], they are not widely used. This is mainly due to the difficulty of making these measurements stable enough to use them for routine assessment. Even if these problems were to be resolved these markers are not compatible with SPION needed for magnetic cell delivery. A potential alternative would be the use of a multimodal approach with SPION for spatial localisation and SPECT / PET or bioluminescence for sensitive detection of cell viability of differentiation status[214-216].

7.5 Conclusions

MRI is ideally suited for magnetic cell tracking particular after magnetic cell delivery. Its non-invasive nature allows for cell tracking over time and potential quality assessment of tissue engineered grafts. Aside from the need for further technical developments to make methods more robust, there is also a need to reduce false positive detection of blood related products; a major stepping stone for widespread use is the inability to assess cell viability. The only current solution for this problem is to use additional non-invasive imaging techniques.

8 Conclusions and future directions

Magnetic cell and drug delivery has the potential to become a useful technology to improve treatment efficacy. In order to realise this potential major hurdles need to be overcome. This includes technical limitations of insufficient forces deep inside the body for external magnets, availability of clinically approved magnetic particles and the safety and efficacy of the cell or drug based procedure.

Chapter 4 and 5 were focused on the potential of an MRI system for magnetic targeting. Potential advantages of such an approach are: full magnetisation of particles due to high field strength, high spatial and temporal control over magnetic field gradients allowing controlled steering of magnetic objects, visualisation of delivery success and the possibility for a closed control loop. Experimental results from chapters 4 and 5 indicate that cells can be steered in a flow phantom at modest flow rates and visualised via MRI. However, to illustrate the clinical potential of such an approach it will be necessary to achieve higher targeting efficiencies at high flow rates. The experimental results indicate that the major limitation is the weak magnetic force acting on cells. Another limitation is the difficulty to track diffusely distributed cells. This is particular problematic if active cell guidance has to be used to steer cells through several bifurcations. Of course that presupposes the means to accurately detect the cell bolus in a few milliseconds which will be difficult. As mentioned in chapter 5 cell aggregations can be an advantage as it increases the targeting efficiency. However, it could also lead to micro emboli, although there is no direct evidence for this as yet. The magnetic cell steering experiments conducted with MRT did not included assessments of potential long term effects on the growth and differentiation potential of cells. This is a limitation that needs to be addressed if this technique is to be used for therapeutic cell delivery.

Potential future steps for the development of MRI for magnetic delivery are: hardware modifications to increase the gradient amplitude, increasing dipole interaction forces to generate bigger aggregates, reducing the blood flow velocity, improving strategies to allow in vivo magnetofection via MRI, exploiting alternative delivery routes, improving the ability to detect labelled cells or drugs in short timeframes and assessment of potential long term effects on targeted cells.

The available gradient strength is one of the major variables determining targeting efficacy. Increasing the gradient strength on preclinical MRI systems is certainly feasible but it is questionable if such gradient strengths could be achieved for a clinical system. Additional consideration has to be given to the risk of peripheral nerve stimulation if high amplitude gradients are switched rapidly. One possibility to avoid this problem is the used of dedicated steering gradients which do not comply to the stringent criteria of MRI but are optimised for targeting and would hence not suffer duty cycle limitations. This would be feasible but would create difficulties if imaging is used intermittently to guide particles or cells along.

In order to use big aggregates due to dipole interaction to increase targeting efficiency, we will need a better understanding of the formation of these aggregates and their controlled breakdown. Experimental studies at high flux densities with different particle sizes, concentrations and shear rates should elucidate these questions. Aggregation of labelled cells or drugs could be useful provided that these aggregates can be broken down by increased shear rates of small blood vessels or actively via other means. In addition, the risk of micro emboli formation should be assessed in a suitable animal model.

Another option would be to reduce the blood flow temporarily to achieve higher targeting efficiencies if that is medically acceptable. This might be an easy way to increase targeting efficacy. However, it needs to be assessed together with the potential delivery device which would be used for such an application. There are also practical question of potential aggregation of cells in the delivery device particularly when it is introduced into the fringe field of an MRI scanner, as well as questions of increased risks to a patient from the movement into the MRI scanner with a delivery device placed in a blood vessel. Alternatively the delivery device might be introduced into the vasculature while the patient is in the MRI scanner similar to MR based vascular interventions.

The above mentioned points aim at increasing targeting efficiency. Alternatively it might be valuable to explore additional applications which would increase the value of such a technique. An obvious candidate that comes to mind is magnetofection as this would allow non-viral based gen delivery. For example DNA conjugated to iron oxide particles could be steered to a site of interest using the gradient coils. Following delivery a strong oscillating gradient could be applied in order to enhance magnetofection. The ability to perform non-viral DNA delivery would be of

considerable clinical interest provided sufficient targeting and transfection efficiencies could be achieved.

Finally alternative routes for drug delivery might be suitable for targeted delivery with an MRI system. The most obvious candidate for such an alternative is respiratory drug delivery. Aerosol containing magnetic particles can be made with sufficient droplet sizes to keep them suspended for several seconds. The low viscosity of air should than allow for more efficient steering compared to particles suspended in water. This alternative should be explored first in suitable flow phantoms and later in an animal model to show the feasibility of such an approach.

Chapter 6 focused on theoretical optimisations of a magnetic delivery strategy based on permanent magnets. It showed that theoretical models can be used to compare a range of potential devices and select the best performing one for a particular application. Additionally the question of scalability which is one of the major stepping stones for magnetic drug and cell delivery has been addressed for that particular example. Such theoretical approaches will of course need experimental validation but they should allow reducing the parameter space to a tractable size. Major limitations of the optimisations performed in Chapter 6 are the idealisation of the MRI derived blood vessel geometry, the small number of geometries, the exclusion of dipole-dipole interaction as well as hydrodynamic interactions and the lack of experimental validation.

The next steps with regard to the work presented in chapter 6 falls into two groups: improving the modelling approach to make it more comprehensive and secondly experimental validation of magnetic cell delivery in a suitable animal model.

The combination of FEM and CFD used for the study presented in Chapter 6 is suboptimal particular as it did not include dipole-dipole or hydrodynamic interactions. This is a major limitation particular if concentrated solutions of magnetic particles are to be simulated. There are examples in the literature which show the integration of dipole-dipole interactions into CFD models. Most of these approaches use discrete particle models which track each particle individually and estimate their interaction with surrounding particles at each time step. This is a possible way to extend the models used in chapter 6. However, discrete particle models are computationally very expensive and are hence limited to a few hundred to thousand particles. An alternative to this approach might be the use of multi scale models where a micro

scale model is used to derive particle behaviour. Results from such a model could be used to model particle aggregation in the CFD model as the density of a two component fluid. Aside from these points the existing models could be used to evaluate the potential of magnetic drug delivery to the injured vessel which might be useful as an addition or alternative to cell delivery. It might also be of interested to perform patient-specific modelling to estimate cell and drug delivery efficiency for a clinically relevant patient population.

As mentioned previously theoretical models do need validation. The next step for magnetic cell delivery to arteries with a Halbach cylinder is hence to test this approach in an animal model. A rabbit denudation model would be particular suitable for that as it is a suitable model for restenosis after angioplasty. A scaled down magnet should be manufactured and compared against the FEM simulation results. A suitable cell type such as EPCs or MSCs which has the potential to reendothelialise the blood vessel after injury need to be selected and a labelling protocol needs to be optimised. Following that labelled cells should be delivered with a delivery protocol that is feasible for humans. Delivery success and cell distribution should be assessed after delivery. Cell distribution and delivery success can be estimated via different means but it would be good to test if MRI can be used as it is clinically applicable. These early time point assessments are important but the most important outcome measure for such a study has to be the degree of restenosis after a sufficient time period for example 1 month after cell delivery. This assessment should include the use of techniques that can be used clinically.

Experimental studies could also be conducted for the use of a Halbach cylinder for magnetic drug delivery to lower leg arteries after angioplasty. For this experiment magnetic particles with a long blood half life time should be loaded with a suitable drug such as paclitaxe. Depending on side effects and targeting efficiencies multiple drug administration might be feasible. Here the final outcome measure should again be the degree of restenosis. Alternatively the delivery of pro angiogenic drugs to improve the blood supply in ischemic limbs could be tested.

The main limitation of the experiments conducted for MRI based cell tracking in the ifarcted rat heart are the small number of animals used and the lack of a non-invasive method for the assessment of cell viability. Additionally the MRI detection limit for cells delivery into the heart has not been assessed comprehensively. An experimental study should be performed which uses an expression based cell viability

marker together with iron oxide nanoparticles. With this combination the status of injected cells should be assessed over a typically period for cardiac remodelling (> 6 weeks in rats). Such a study could also be used to evaluate the potential of R_2 and R_2* maps to differentiate between free and internalised particles. It would also be of interest to evaluate potential interference of magnetically labelled cells in the heart with commonly used cardiac MRI protocols for the clinical assessment of infracted hears such as late Gadolinium enhancement, myocardial strain imaging or stress imaging.

Major limitations of MRI based cell tracking in tissue engineered scaffolds are the small number of samples assessed, insufficient assessment of detection limit and potential error due to cell aggregation and the used of an additional modality to assess cell viability. Similar to the cardiac example the assessment of cell viability and potentially differentiation status would be of particular interest. Depending on the geometry of the scaffolds a range of non invasive imaging modalities could be used for that purpose. A combination of such a modality with MRI in the light of potential clinical constrains should be tested to estimate the detection limit and variability of such a combined approach.

References

1. Rosamond W, Flegal K, Friday G, Furie K, Go A, Greenlund K, et al. Heart Disease and Stroke Statistics--2007 Update: A Report From the American Heart Association Statistics Committee and Stroke Statistics Subcommittee. Circulation **115**, e69-171 (2007)

2. Kehat I, Khimovich L, Caspi O, Gepstein A, Shofti R, Arbel G, et al. Electromechanical integration of cardiomyocytes derived from human embryonic stem cells. Nat Biotech **22**, 1282-9 (2004)

3. Xue T, Cho HC, Akar FG, Tsang SY, Jones SP, Marban E, et al. Functional Integration of Electrically Active Cardiac Derivatives From Genetically Engineered Human Embryonic Stem Cells With Quiescent Recipient Ventricular Cardiomyocytes: Insights Into the Development of Cell-Based Pacemakers. Circulation **111**, 11-20 (2005)

4. Caspi O, Huber I, Kehat I, Habib M, Arbel G, Gepstein A, et al. Transplantation of Human Embryonic Stem Cell-Derived Cardiomyocytes Improves Myocardial Performance in Infarcted Rat Hearts. Journal of the American College of Cardiology **50**, 1884-93 (2007)

5. Laflamme MA, Chen KY, Naumova AV, Muskheli V, Fugate JA, Dupras SK, et al. Cardiomyocytes derived from human embryonic stem cells in pro-survival factors enhance function of infarcted rat hearts. Nat Biotech **25**, 1015-24 (2007)

6. van Laake LW, Passier R, Doevendans PA, Mummery CL. Human Embryonic Stem Cell-Derived Cardiomyocytes and Cardiac Repair in Rodents. Circ Res **102**, 1008-10 (2008)

7. Rubart M, Pasumarthi KBS, Nakajima H, Soonpaa MH, Nakajima HO, Field LJ. Physiological Coupling of Donor and Host Cardiomyocytes After Cellular Transplantation. Circ Res **92**, 1217-24 (2003)

8. Orlic D, Kajstura J, Chimenti S, Jakoniuk I, Anderson SM, Li B, et al. Bone marrow cells regenerate infarcted myocardium. Nature **410**, 701-5 (2001)

9. Yoshioka T, Ageyama N, Shibata H, Yasu T, Misawa Y, Takeuchi K, et al. Repair of Infarcted Myocardium Mediated by Transplanted Bone Marrowâ€"Derived CD34+ Stem Cells in a Nonhuman Primate Model. Stem Cells **23**, 355-64 (2005)

10. Amsalem Y, Mardor Y, Feinberg MS, Landa N, Miller L, Daniels D, et al. Iron-Oxide Labeling and Outcome of Transplanted Mesenchymal Stem Cells in the Infarcted Myocardium. Circulation **116**, I-38 (2007)

11. Gnecchi M, He H, Liang OD, Melo LG, Morello F, Mu H, et al. Paracrine action accounts for marked protection of ischemic heart by Akt-modified mesenchymal stem cells. Nature Medicine **11**, 367-8 (2005)

12. Abdel-Latif A, Bolli R, Tleyjeh IM, Montori VM, Perin EC, Hornung CA, et al. Adult Bone Marrow-Derived Cells for Cardiac Repair: A Systematic Review and Meta-analysis. Arch Intern Med **167**, 989-97 (2007)

13. Chen S, Liu Z, Tian N, Zhang J, Yei F, Duan B, et al. Intracoronary transplantation of autologous bone marrow mesenchymal stem cells for ischemic cardiomyopathy due to

isolated chronic occluded left anterior descending artery. J Invasive Cardiol **18**, 552-6 (2006)

14. Hou D, Youssef EA-S, Brinton TJ, Zhang P, Rogers P, Price ET, et al. Radiolabeled Cell Distribution After Intramyocardial, Intracoronary, and Interstitial Retrograde Coronary Venous Delivery: Implications for Current Clinical Trials. Circulation **112**, I-150 (2005)

15. Cheng K, Li TS, Malliaras K, Davis D, Zhang Y, Marban E. Magnetic Targeting Enhances Engraftment and Functional Benefit of Iron-Labeled Cardiosphere-Derived Cells in Myocardial Infarction. Circ Res , CIRCRESAHA (2010)

16. Smart N, Bollini S, Dube KN, Vieira JM, Zhou B, Davidson S, et al. De novo cardiomyocytes from within the activated adult heart after injury. Nature **474**, 640-4 (2011)

17. Hirsch AT, Criqui MH, Treat-Jacobson D, Regensteiner JG, Creager MA, Olin JW, et al. Peripheral Arterial Disease Detection, Awareness, and Treatment in Primary Care. JAMA **286**, 1317-24 (2001)

18. American Heart Association. Heart Disease and Stroke Statistics-2004 **Dallas**, (2004)

19. Becker GJ, McClenny TE, Kovacs ME, Raabe RD, Katzen BT. The importance of increasing public and physician awareness of peripheral arterial disease. J Vasc Interv Radiol **13**, 7-11 (2002)

20. Graziani L, Piaggesi A. Indications and clinical outcomes for below knee endovascular therapy: Review article. Cathet Cardiovasc Intervent **75**, 433-43 (2010)

21. White CJ, Gray WA. Endovascular Therapies for Peripheral Arterial Disease: An Evidence-Based Review. Circulation **116**, 2203-15 (2007)

22. Hoffmann R, Mintz GS, Dussaillant GR, Popma JJ, Pichard AD, Satler LF, et al. Patterns and Mechanisms of In-Stent Restenosis: A Serial Intravascular Ultrasound Study. Circulation **94**, 1247-54 (1996)

23. Kornowski R, Hong MK, Tio FO, Bramwell O, Wu H, Leon MB. In-Stent Restenosis: Contributions of Inflammatory Responses and Arterial Injury to Neointimal Hyperplasia. J Am Coll Cardiol **31**, 224-30 (1998)

24. Heldman AW, Cheng L, Jenkins GM, Heller PF, Kim DW, Ware M, Jr., et al. Paclitaxel Stent Coating Inhibits Neointimal Hyperplasia at 4 Weeks in a Porcine Model of Coronary Restenosis. Circulation **103**, 2289-95 (2001)

25. Kong D, Melo LG, Mangi AA, Zhang L, Lopez-Ilasaca M, Perrella MA, et al. Enhanced Inhibition of Neointimal Hyperplasia by Genetically Engineered Endothelial Progenitor Cells. Circulation **109**, 1769-75 (2004)

26. Werner N, Junk S, Laufs U, Link A, Walenta K, Bohm M, et al. Intravenous Transfusion of Endothelial Progenitor Cells Reduces Neointima Formation After Vascular Injury. Circ Res **93**, e17-e24 (2003)

27. Windecker S, Mayer I, De Pasquale G, Maier W, Dirsch O, De Groot P, et al. Stent Coating With Titanium-Nitride-Oxide for Reduction of Neointimal Hyperplasia. Circulation **104**, 928-33 (2001)

28. Aoki J, Serruys PW, van Beusekom H, Ong ATL, McFadden EP, Sianos G, et al. Endothelial Progenitor Cell Capture by Stents Coated With Antibody Against CD34: The HEALING-FIM (Healthy Endothelial Accelerated Lining Inhibits Neointimal Growth-First In Man) Registry. J Am Coll Cardiol **45**, 1574-9 (2005)

29. Lagerqvist B, James SK, Stenestrand U, LindbÃ¤ck J, Nilsson T, Wallentin L. Long-Term Outcomes with Drug-Eluting Stents versus Bare-Metal Stents in Sweden. New England Journal of Medicine **356**, 1009-19 (2007)

30. Asahara T, Murohara T, Sullivan A, Silver M, van der Zee R, Li T, et al. Isolation of Putative Progenitor Endothelial Cells for Angiogenesis. Science **275**, 964-6 (1997)

31. Waksman R, Baffour R, Pakala R, Scheinowitz M, Hellinga D, Seabron R, et al. Effects of exogenous peripheral-blood-derived endothelial progenitor cells or unfractionated bone-marrow-derived cells on neointimal formation and inflammation in cholesterol-fed, balloon-denuded, and radiated iliac arteries of inbred rabbits. Cardiovascular Revascularization Medicine **10**, 110-6 (2004)

32. Antonia G, Cristiana DC, Giulio P, Paolo B, Maurizio CC. Regenerative Therapy in Peripheral Artery Disease. Cardiovascular Therapeutics **27**, 289-304 (2009)

33. Kajiguchi M, Kondo T, Izawa H, Kobayashi M, Yamamoto K, Shintani S, et al. Safety and efficacy of autologous progenitor cell transplantation for therapeutic angiogenesis in patients with critical limb ischemia. Circ J **71**, 196-201 (2007)

34. Pelliccia F, Cianfrocca C, Rosano G, Mercuro G, Speciale G, Pasceri V. Role of Endothelial Progenitor Cells in Restenosis and Progression of Coronary Atherosclerosis After Percutaneous Coronary Intervention: A Prospective Study. J Am Coll Cardiol Intv **3**, 78-86 (2010)

35. Hanahan D, Weinberg RA. Hallmarks of Cancer: The Next Generation. Cell 144[5], 646-674. 4-3-2011.

36. Baker DEC, Harrison NJ, Maltby E, Smith K, Moore HD, Shaw PJ, et al. Adaptation to culture of human embryonic stem cells and oncogenesis in vivo. Nat Biotech **25**, 207-15 (2007)

37. Mayshar Y, Ben-David U, Lavon N, Biancotti JC, Yakir B, Clark AT, et al. Identification and Classification of Chromosomal Aberrations in Human Induced Pluripotent Stem Cells. Cell stem cell **7**, 521-531. 8-10-2010.

38. Sareen D, McMillan E, Ebert AD, Shelley BC, Johnson JA, Meisner LF, et al. Chromosome 7 and 19 Trisomy in Cultured Human Neural Progenitor Cells. PLoS ONE **4**, e7630 (2009)

39. Amariglio N, Hirshberg A, Scheithauer BW, Cohen Y, Loewenthal R, Trakhtenbrot L, et al. Donor-Derived Brain Tumor Following Neural Stem Cell Transplantation in an Ataxia Telangiectasia Patient. PLoS Med **6**, e1000029 (2009)

40. Papapetrou EP, Lee G, Malani N, Setty M, Riviere I, Tirunagari LMS, et al. Genomic safe harbors permit high [beta]-globin transgene expression in thalassemia induced pluripotent stem cells. Nat Biotech **29**, 73-8 (2011)

41. Pankhurst QA, Connolly J, Jones SK, Dobson J. Applications of magnetic nanoparticles in biomedicine. Journal of Physics D: Applied Physics **36**, R167-R181 (2003)

42. Krishnan KM. Biomedical Nanomagnetics: A Spin Through Possibilities in Imaging, Diagnostics, and Therapy. Magnetics, IEEE Transactions on **46**, 2523-58 (2010)

43. Bulte JWM, Douglas T, Witwer B, Zhang SC, Strable E, Lewis BK, et al. Magnetodendrimers allow endosomal magnetic labeling and in vivo tracking of stem cells. Nat Biotech **19**, 1141-7 (2001)

44. Erik MS. Antibody-mediated cell labeling of peripheral T cells with micron-sized iron oxide particles (MPIOs) allows single cell detection by MRI. Contrast Media & Molecular Imaging **2**, 147-53 (2007)

45. McAteer MA, Schneider JE, Ali ZA, Warrick N, Bursill CA, von zur Muhlen C, et al. Magnetic Resonance Imaging of Endothelial Adhesion Molecules in Mouse Atherosclerosis Using Dual-Targeted Microparticles of Iron Oxide. Arterioscler Thromb Vasc Biol **28**, 77-83 (2008)

46. Wilhelm C, Gazeau F. Universal cell labelling with anionic magnetic nanoparticles. Biomaterials **29**, 3161-74 (2008)

47. Weissleder R, Stark DD, Engelstad BL, Bacon BR, Compton CC, White DL, et al. Superparamagnetic iron oxide: pharmacokinetics and toxicity. Am J Roentgenol **152**, 167-73 (1989)

48. MELVILLE D, PAUL F, ROATH S. Direct magnetic separation of red cells from whole blood. Nature **255**, 706 (1975)

49. Takayasu M, Kelland DR, Minervini JV. Continuous magnetic separation of blood components from whole blood. Applied Superconductivity, IEEE Transactions on **10**, 927-30 (2000)

50. Bahaj AS, James PAB, Moeschler FD. Low magnetic-field separation system for metal-loaded magnetotactic bacteria. Journal of Magnetism and Magnetic Materials **177-181**, 1453-4 (1998)

51. Frankel RB, Blakemore RP, Mackay AL. Precipitation of Fe3O4 in Magnetotactic Bacteria. Philosophical Transactions of the Royal Society of London Series B, Biological Sciences **304**, 567-74 (1984)

52. Owen CS, Lindsay JG. Ferritin as a label for high-gradient magnetic separation. Biophysical Journal **42**, 145-50 (1983)

53. Zborowski M, Fuh CB, Green R, Baldwin NJ, Reddy S, Douglas T, et al. Immunomagnetic isolation of magnetoferritin-labeled cells in a modified ferrograph. Cytometry **24**, 251-9 (1996)

54. Berensmeier S. Magnetic particles for the separation and purification of nucleic acids. Applied Microbiology and Biotechnology **73**, 495-504 (2006)

55. Chalmers JJ, Zborowski M, Sun L, Moore L. Flow Through, Immunomagnetic Cell Separation. Biotechnol Progress **14**, 141-8 (1998)

56. Grützkau A, Radbruch A. Small but mighty: How the MACS-technology based on nanosized superparamagnetic particles has helped to analyze the immune system within the last 20 years. Cytometry **77A**, 643-7 (2010)

57. Hornig-Do HT, G³nther G, Bust M, Lehnartz P, Bosio A, Wiesner RJ. Isolation of functional pure mitochondria by superparamagnetic microbeads. Analytical Biochemistry **389**, 1-5 (2009)

58. Laitinen A, Laine J. Isolation of Mesenchymal Stem Cells from Human Cord Blood. Current Protocols in Stem Cell Biology. John Wiley & Sons, Inc.; 2007.

59. Madonna AJ, Basile F, Furlong E, Voorhees KJ. Detection of bacteria from biological mixtures using immunomagnetic separation combined with matrix-assisted laser desorption/ionization time-of-flight mass spectrometry. Rapid Commun Mass Spectrom **15**, 1068-74 (2001)

60. Pamme N, Wilhelm C. Continuous sorting of magnetic cells via on-chip free-flow magnetophoresis. Lab Chip **6**, 974-80 (2006)

61. Safarik I, Safarikova M. Use of magnetic techniques for the isolation of cells. J Chromatogr B Biomed Sci Appl **722**, 33-53 (1999)

62. Sieben S, Bergemann C, L³bbe A, Brockmann B, Rescheleit D. Comparison of different particles and methods for magnetic isolation of circulating tumor cells. Journal of Magnetism and Magnetic Materials **225**, 175-9 (2001)

63. Wang Y, Ravindranath S, Irudayaraj J. Separation and detection of multiple pathogens in a food matrix by magnetic SERS nanoprobes. Analytical and Bioanalytical Chemistry **399**, 1271-8 (2011)

64. Bucak S, Jones DA, Laibinis PE, Hatton TA. Protein Separations Using Colloidal Magnetic Nanoparticles. Biotechnol Progress **19**, 477-84 (2003)

65. Safarik I, Safarikova M. Magnetic techniques for the isolation and purification of proteins and peptides. Biomagn Res Technol **2**, 7 (2004)

66. Monceyron C, Grinde B. Detection of hepatitis A virus in clinical and environmental samples by immunomagnetic separation and PCR. Journal of Virological Methods **46**, 157-66 (1994)

67. Veyret R, Elaissari A, Marianneau P, SALL AA, Delair T. Magnetic colloids for the generic capture of viruses. Analytical Biochemistry **346**, 59-68 (2005)

68. Doyle PS, Bibette J+, Bancaud Al, Viovy JL. Self-Assembled Magnetic Matrices for DNA Separation Chips. Science **295**, 2237 (2002)

69. Alderton RP, Eccleston LM, Howe RP, Read CA, Reeve MA, Beck S. Magnetic bead purification of M13 DNA sequencing templates. Analytical Biochemistry **201**, 166-9 (1992)

70. Bitton G, Mitchell R. The removal of Escherichia coli-bacteriophage T7 by magnetic filtration. Water Research **8**, 549-51 (1974)

71. Said TM, Agarwal A, Zborowski M, Grunewald S, Glander HJ, Paasch U. Utility of Magnetic Cell Separation as a Molecular Sperm Preparation Technique. J Androl **29**, 134-42 (2008)

72. Islam D, Lindberg AA. Detection of Shigella dysenteriae type 1 and Shigella flexneri in feces by immunomagnetic isolation and polymerase chain reaction. J Clin Microbiol **30**, 2801-6 (1992)

73. Ito A, Shinkai M, Honda H, Kobayashi T. Medical application of functionalized magnetic nanoparticles. Journal of Bioscience and Bioengineering **100**, 1-11 (2005)

74. Mornet S, Vasseur S, Grasset F, Duguet E. Magnetic nanoparticle design for medical diagnosis and therapy. J Mater Chem **14**, 2161-75 (2004)

75. Kodituwakku AP, Jessup C, Zola H, Roberton DM. Isolation of antigen-specific B cells. Immunol Cell Biol **81**, 163-70 (2003)

76. Miltenyi S, MÃ¼ller W, Weichel W, Radbruch A. High gradient magnetic cell separation with MACS. Cytometry **11**, 231-8 (1990)

77. Zborowski M. Commercial magnetic cell separation instruments and reagents. In: and MZ, editor. Laboratory Techniques in Biochemistry and Molecular Biology Magnetic Cell Separation. Volume 32 ed. Elsevier; 2007. p. 265-92.

78. Zborowski M, Sun L, Moore LR, Stephen Williams P, Chalmers JJ. Continuous cell separation using novel magnetic quadrupole flow sorter. Journal of Magnetism and Magnetic Materials **194**, 224-30 (1999)

79. Terranova BE, Burns MA. Continuous cell suspension processing using magnetically stabilized fluidized beds. Biotechnol Bioeng **37**, 110-20 (1991)

80. Allen TM, Cullis PR. Drug Delivery Systems: Entering the Mainstream. Science **303**, 1818-22 (2004)

81. Jon D. Magnetic nanoparticles for drug delivery. Drug Development Research **67**, 55-60 (2006)

82. Neuberger T, Sch÷pf B, Hofmann H, Hofmann M, von Rechenberg B. Superparamagnetic nanoparticles for biomedical applications: Possibilities and limitations of a new drug delivery system. Journal of Magnetism and Magnetic Materials **293**, 483-96 (2005)

83. Luebbe AS, Alexiou C, Bergmann C. Clinical Applications of Magnetic Drug Targeting. Journal of Surgical Research **95**, 200-6 (2001)

84. Lubbe AS, Bergemann C, Riess H, Schriever F, Reichardt P, Possinger K, et al. Clinical Experiences with Magnetic Drug Targeting: A Phase I Study with 4'-Epidoxorubicin in 14 Patients with Advanced Solid Tumors. Cancer Res **56**, 4686-93 (1996)

85. Babincová M, Cicmanec P, Altanerovβ V, Altaner C, Babinec P. AC-magnetic field controlled drug release from magnetoliposomes: design of a method for site-specific chemotherapy. Bioelectrochemistry **55**, 17-9 (2002)

86. Hu SH, Liu TY, Huang HY, Liu DM, Chen SY. Magnetic-Sensitive Silica Nanospheres for Controlled Drug Release. Langmuir **24**, 239-44 (2007)

87. Meyer DE, Shin BC, Kong GA, Dewhirst MW, Chilkoti A. Drug targeting using thermally responsive polymers and local hyperthermia. J Control Release **74**, 213-24 (2001)

88. Ali S.Arbab G. Labeling of cells with ferumoxides-protamine sulfate complexes does not inhibit function or differentiation capacity of hematopoietic or mesenchymal stem cells. NMR in Biomedicine **18**, 553-9 (2005)

89. Thorek DLJ, Tsourkas A. Size, charge and concentration dependent uptake of iron oxide particles by non-phagocytic cells. Biomaterials **29**, 3583-90 (2008)

90. Rejman J, Oberle V, Zuhorn IS, Hoekstra D. Size-dependent internalization of particles via the pathways of clathrin- and caveolae-mediated endocytosis. Biochemical Journal **337**, 159-69 (4 A.D.)

91. Arbab AS, Yocum GT, Kalish H, Jordan EK, Anderson SA, Khakoo AY, et al. Efficient magnetic cell labeling with protamine sulfate complexed to ferumoxides for cellular MRI. Blood **104**, 1217-23 (2004)

92. Frank JA, Miller BR, Arbab AS, Zywicke HA, Jordan EK, Lewis BK, et al. Clinically Applicable Labeling of Mammalian and Stem Cells by Combining Superparamagnetic Iron Oxides and Transfection Agents1. Radiology **228**, 480-7 (2003)

93. Berry CC, Charles S, Wells S, Dalby MJ, Curtis ASG. The influence of transferrin stabilised magnetic nanoparticles on human dermal fibroblasts in culture. International Journal of Pharmaceutics **269**, 211-25 (2004)

94. Ahrens ET, Feili-Hariri M, Xu H, Genove G, Morel PA. Receptor-mediated endocytosis of iron-oxide particles provides efficient labeling of dendritic cells for in vivo MR imaging. Magnetic Resonance in Medicine **49**, 1006-13 (2003)

95. Tai JH, Foster P, Rosales A, Feng B, Hasilo C, Martinez V, et al. Imaging Islets Labeled With Magnetic Nanoparticles at 1.5 Tesla. Diabetes **55**, 2931-8 (2006)

96. Plank C, Scherer F, Schillinger U, Bergemann C, Anton M. Magnetofection: Enhancing and Targeting Gene Delivery with Superparamagnetic Nanoparticles and Magnetic Fields. Journal of Liposome Research **13**, 29-32 (2003)

97. Pouliquen D, Le Jeune JJ, Perdrisot R, Ermias A, Jallet P. Iron oxide nanoparticles for use as an MRI contrast agent: Pharmacokinetics and metabolism. Magnetic Resonance Imaging **9**, 275-83 (1991)

98. Jain TK, Reddy MK, Morales MA, Leslie-Pelecky DL, Labhasetwar V. Biodistribution, Clearance, and Biocompatibility of Iron Oxide Magnetic Nanoparticles in Rats. Molecular Pharmaceutics **5**, 316-27 (2008)

99. Balakumaran A, Pawelczyk E, Ren J, Sworder B, Chaudhry A, Sabatino M, et al. Superparamagnetic iron oxide nanoparticles labeling of bone marrow stromal (mesenchymal) cells does not affect their "stemness". PLoS ONE **5**, e11462 (2010)

100. Neri M, Maderna C, Cavazzin C, idda-Vigoriti V, Politi LS, Scotti G, et al. Efficient In Vitro Labeling of Human Neural Precursor Cells with Superparamagnetic Iron Oxide Particles: Relevance for In Vivo Cell Tracking. Stem Cells **26**, 505-16 (2008)

101. Stroh A, Faber C, Neuberger T, Lorenz P, Sieland K, Jakob PM, et al. In vivo detection limits of magnetically labeled embryonic stem cells in the rat brain using high-field (17.6 T) magnetic resonance imaging. NeuroImage **24**, 635-45 (2005)

102. Terrovitis J, Stuber M, Youssef A, Preece S, Leppo M, Kizana E, et al. Magnetic Resonance Imaging Overestimates Ferumoxide-Labeled Stem Cell Survival After Transplantation in the Heart. Circulation **117**, 1555-62 (2008)

103. Zhu J, Zhou L, XingWu F. Tracking Neural Stem Cells in Patients with Brain Trauma. N Engl J Med **355**, 2376-8 (2006)

104. Kostura L, Kraitchman DL, Mackay AM, Pittenger MF, Bulte JWM. Feridex labeling of mesenchymal stem cells inhibits chondrogenesis but not adipogenesis or osteogenesis. NMR in Biomedicine **17**, 513-7 (2004)

105. Wilhelm C, Bal L, Smirnov P, Galy-Fauroux I, Clθment O, Gazeau F, et al. Magnetic control of vascular network formation with magnetically labeled endothelial progenitor cells. Biomaterials **28**, 3797-806 (2007)

106. Pislaru SV, Harbuzariu A, Gulati R, Witt T, Sandhu NP, Simari RD, et al. Magnetically Targeted Endothelial Cell Localization in Stented Vessels. J Am Coll Cardiol , j (2006)

107. Kedziorek DA, Muja N, Walczak P, Ruiz-Cabello J, Gilad AA, Jie CC, et al. Gene expression profiling reveals early cellular responses to intracellular magnetic labeling with superparamagnetic iron oxide nanoparticles. Magnetic Resonance in Medicine **63**, 1031-43 (2010)

108. Farrell E, Wielopolski P, Pavljasevic P, van Tiel S, Jahr H, Verhaar J, et al. Effects of iron oxide incorporation for long term cell tracking on MSC differentiation in vitro and in vivo. Biochemical and Biophysical Research Communications **369**, 1076-81 (2008)

109. Bhabra G, Sood A, Fisher B, Cartwright L, Saunders M, Evans WH, et al. Nanoparticles can cause DNA damage across a cellular barrier. Nat Nanotechnol **4(12),** 876-83 (2009)

110. de Vries IJ, Lesterhuis WJ, Barentsz JO, Verdijk P, van Krieken JH, Boerman OC, et al. Magnetic resonance tracking of dendritic cells in melanoma patients for monitoring of cellular therapy. Nat Biotech **23**, 1407-13 (2005)

111. Karussis D, Karageorgiou C, Vaknin-Dembinsky A, Gowda-Kurkalli B, Gomori JM, Kassis I, et al. Safety and Immunological Effects of Mesenchymal Stem Cell Transplantation in Patients With Multiple Sclerosis and Amyotrophic Lateral Sclerosis. Arch Neurol **67**, 1187-94 (2010)

112. Halbach K. Design of permanent multipole magnets with oriented rare earth cobalt material. Nuclear Instruments and Methods **169**, 1-10 (1980)

113. Alexiou C, Jurgons R, Schmid RJ, Bergemann C, Henke J, Erhardt W, et al. Magnetic Drug Targeting-Biodistribution of the Magnetic Carrier and the Chemotherapeutic agent Mitoxantrone after Locoregional Cancer Treatment. Journal of Drug Targeting **11**, 139-49 (2003)

114. Chen H, Kaminski MD, Pytel P, Macdonald L, Rosengart AJ. Capture of magnetic carriers within large arteries using external magnetic fields. Journal of Drug Targeting **16**, 262-8 (2008)

115. Fortin-Ripoche JP, Martina MS, Gazeau F, Menager C, Wilhelm C, Bacri JC, et al. Magnetic Targeting of Magnetoliposomes to Solid Tumors with MR Imaging Monitoring in Mice: Feasibility. Radiology **239**, 415-24 (2006)

116. Hirota Y, Akiyama Y, Izumi Y, Nishijima S. Fundamental study for development magnetic drug delivery system. Physica C: Superconductivity **469**, 1853-6 (2009)

117. Kyrtatos PG, Lehtolainen P, Junemann-Ramirez M, Garcia-Prieto A, Price AN, Martin JF, et al. Magnetic Tagging Increases Delivery of Circulating Progenitors in Vascular Injury. JACC: Cardiovascular Interventions **2**, 794-802 (2009)

118. Lübbe AS, Bergemann C, Huhnt W, Fricke T, Riess H, Brock JW, et al. Preclinical Experiences with Magnetic Drug Targeting: Tolerance and Efficacy. Cancer Res **56**, 4694-701 (1996)

119. Hofmann A, Wenzel D, Becher UM, Freitag DF, Klein AM, Eberbeck D, et al. Combined targeting of lentiviral vectors and positioning of transduced cells by magnetic nanoparticles. Proceedings of the National Academy of Sciences **106**, 44-9 (2009)

120. Kubo T, Sugita T, Shimose S, Nitta Y, Ikuta Y, Murakami T. Targeted delivery of anticancer drugs with intravenously administered magnetic liposomes in osteosarcoma-bearing hamsters. Int J Oncol **17**, 309-15 (2000)

121. Ally J, Martin B, Behrad Khamesee M, Roa W, Amirfazli A. Magnetic targeting of aerosol particles for cancer therapy. Journal of Magnetism and Magnetic Materials **293**, 442-9 (2005)

122. Dames P, Gleich B, Flemmer A, Hajek K, Seidl N, Wiekhorst F, et al. Targeted delivery of magnetic aerosol droplets to the lung. Nat Nano **2**, 495-9 (2007)

123. Huang Z, Pei N, Wang Y, Xie X, Sun A, Shen L, et al. Deep magnetic capture of magnetically loaded cells for spatially targeted therapeutics. Biomaterials **31,** 2130-40 (2010)

124. Kobayashi T, Ochi M, Yanada S, Ishikawa M, Adachi N, Deie M, et al. A Novel Cell Delivery System Using Magnetically Labeled Mesenchymal Stem Cells and an External Magnetic Device for Clinical Cartilage Repair. Arthroscopy: The Journal of Arthroscopic & Related Surgery **24**, 69-76 (2008)

125. Shapiro B, Probst R, Potts HE, Diver DE, Lubbe AS. Control to Concentrate Drug-Coated Magnetic Particles to Deep-Tissue Tumors for Targeted Cancer Chemotherapy. Proceedings of the46th IEEE Conference on Decision and ControlNew Orleans, LA, USA, Dec 12-14, 2007 , (2007)

126. Takeda Si, Mishima F, Fujimoto S, Izumi Y, Nishijima S. Development of magnetically targeted drug delivery system using superconducting magnet. Journal of Magnetism and Magnetic Materials **311**, 367-71 (2007)

127. Mishima F, Takeda S, Izumi Y, Nishijima S. Development of Magnetic Field Control for Magnetically Targeted Drug Delivery System Using a Superconducting Magnet. Applied Superconductivity, IEEE Transactions on **17**, 2303-6 (2007)

128. Darton NJ, Sederman AJ, Ionescu A, Ducati C, Darton RC, Gladden LF, et al. Manipulation and tracking of superparamagnetic nanoparticles using MRI. Nanotechnology **19**, 395102 (2008)

129. Martel S, Mathieu JB, Felfoul O, Chanu A, Aboussouan E, Tamaz S, et al. Automatic navigation of an untethered device in the artery of a living animal using a conventional clinical magnetic resonance imaging system. Applied Physics Letters **90**, 114105-3 (2007)

130. Mathieu JB, Martel S. Magnetic microparticle steering within the constraints of an MRI system: proof of concept of a novel targeting approach. Biomedical Microdevices **9**, 801-8 (2007)

131. Chorny M, Fishbein I, Yellen BB, Alferiev IS, Bakay M, Ganta S, et al. Targeting stents with local delivery of paclitaxel-loaded magnetic nanoparticles using uniform fields. Proceedings of the National Academy of Sciences **107**, 8346-51 (2010)

132. Forbes ZG, Yellen BB, Halverson DS, Fridman G, Barbee KA, Friedman G. Validation of High Gradient Magnetic Field Based Drug Delivery to Magnetizable Implants Under Flow. Biomedical Engineering, IEEE Transactions on **55**, 643-9 (2008)

133. Polyak B, Friedman G. Magnetic targeting for site-specific drug delivery: applications and clinical potential. Expert Opinion on Drug Delivery **6**, 53-70 (2009)

134. Ritter JA, Ebner AD, Daniel KD, Stewart KL. Application of high gradient magnetic separation principles to magnetic drug targeting. Journal of Magnetism and Magnetic Materials **280**, 184-201 (2004)

135. Rotariu O, Iacob G, Strachan NJC, Chiriac H. Simulating the Embolization of Blood Vessels Using Magnetic Microparticles and Acupuncture Needle in a Magnetic Field. Biotechnol Progress **20**, 299-305 (2004)

136. Avilés MO, Ebner AD, Ritter JA. Ferromagnetic seeding for the magnetic targeting of drugs and radiation in capillary beds. Journal of Magnetism and Magnetic Materials **310**, 131-44 (2007)

137. Häfeli UO, Sweeney SM, Beresford BA, Humm JL, Macklis RM. Effective targeting of magnetic radioactive 90Y-microspheres to tumor cells by an externally applied magnetic field. Preliminary in vitro and in vivo results. Nuclear Medicine and Biology **22**, 147-55 (1995)

138. Dobson J. Gene therapy progress and prospects: magnetic nanoparticle-based gene delivery. Gene Ther **13**, 283-7 (2006)

139. Plank C, Anton M, Rudolph C, Rosenecker J, Kr+Âtz F. Enhancing and targeting nucleic acid delivery by magnetic force. Expert Opinion on Biological Therapy **3**, 745-58 (2003)

140. Scherer F, Anton M, Schillinger U, Henke J, Bergemann C, Kruger A, et al. Magnetofection: enhancing and targeting gene delivery by magnetic force in vitro and in vivo. Gene Ther **9**, 102-9 (2002)

141. Pouponneau P, Leroux JC, Soulez G, Gaboury L, Martel S. Co-encapsulation of magnetic nanoparticles and doxorubicin into biodegradable microcarriers for deep tissue targeting by vascular MRI navigation. Biomaterials **32**, 3481-6 (2011)

142. Dobson J. Remote control of cellular behaviour with magnetic nanoparticles. Nat Nano **3**, 139-43 (2008)

143. H.Perea, J.Aigner, J.T.Heverhagen, U.Hopfner, E.Wintermantel. Vascular tissue engineering with magnetic nanoparticles: seeing deeper. Journal of Tissue Engineering and Regenerative Medicine **1**, 318-21 (2007)

144. Cregg PJ, Murphy K, Mardinoglu A. Inclusion of magnetic dipole-dipole and hydrodynamic interactions in implant-assisted magnetic drug targeting. Journal of Magnetism and Magnetic Materials **321**, 3893-8 (2009)

145. Furlani EJ, Furlani EP. A Model for Predicting Magnetic Targeting of Multifunctional Particles in the Microvasculature. 1-12-2006. Institue for Lasers, Photonics and Biophotonics University at Buffalo, Buffalo, NY, 14260.
Ref Type: Serial (Book,Monograph)

146. Häfeli UO, Gilmour K, Zhou A, Lee S, Hayden ME. Modeling of magnetic bandages for drug targeting: Button vs. Halbach arrays. Journal of Magnetism and Magnetic Materials **311**, 323-9 (2007)

147. Burgess P, Hutt PB, Farokhzad OC, Langer R, Minick S, Zale S. On firm ground: IP protection of therapeutic nanoparticles. Nat Biotech **28**, 1267-70 (2010)

148. Rosensweig RE. Heating magnetic fluid with alternating magnetic field. Journal of Magnetism and Magnetic Materials **252**, 370-4 (2002)

149. Brezovich A. Low frequency hyperthermia: capacitive and ferromagnetic thermoseed methods. Medical physics Monograph, Medical physics; 1988.

150. Balivada S, Rachakatla R, Wang H, Samarakoon T, Dani R, Pyle M, et al. A/C magnetic hyperthermia of melanoma mediated by iron oxide core/shell magnetic nanoparticles: a mouse study. BMC Cancer **10**, 119 (2010)

151. Hergt R, Hiergeist R, Hilger I, Kaiser WA, Lapatnikov Y, Margel S, et al. Maghemite nanoparticles with very high AC-losses for application in RF-magnetic hyperthermia. Journal of Magnetism and Magnetic Materials **270**, 345-57 (2004)

152. Jordan A, Scholz R, Maier-Hauff K, Johannsen M, Wust P, Nadobny J, et al. Presentation of a new magnetic field therapy system for the treatment of human solid tumors with magnetic fluid hyperthermia. Journal of Magnetism and Magnetic Materials **225**, 118-26 (2001)

153. Kallumadil M, Tada M, Nakagawa T, Abe M, Southern P, Pankhurst QA. Suitability of commercial colloids for magnetic hyperthermia. Journal of Magnetism and Magnetic Materials **321**, 1509-13 (2009)

154. Tanaka K, Ito A, Kobayashi T, Kawamura T, Shimada S, Matsumoto K, et al. Heat immunotherapy using magnetic nanoparticles and dendritic cells for T-lymphoma. Journal of Bioscience and Bioengineering **100**, 112-5 (2005)

155. Fortin JP, Wilhelm C, Servais J, Ménager C, Bacri JC, Gazeau F. Size-Sorted Anionic Iron Oxide Nanomagnets as Colloidal Mediators for Magnetic Hyperthermia. J Am Chem Soc **129**, 2628-35 (2007)

156. Colognato R, Bonelli A, Ponti J, Farina M, Bergamaschi E, Sabbioni E, et al. Comparative genotoxicity of cobalt nanoparticles and ions on human peripheral leukocytes in vitro. Mutagenesis **23**, 377-82 (2008)

157. Kim JS, Yoon TJ, Yu KN, Kim BG, Park SJ, Kim HW, et al. Toxicity and Tissue Distribution of Magnetic Nanoparticles in Mice. Toxicological Sciences **89**, 338-47 (2006)

158. Faraji AH, Wipf P. Nanoparticles in cellular drug delivery. Bioorganic & Medicinal Chemistry **17**, 2950-62 (2009)

159. Jain TK, Reddy MK, Morales MA, Leslie-Pelecky DL, Labhasetwar V. Biodistribution, Clearance, and Biocompatibility of Iron Oxide Magnetic Nanoparticles in Rats. Molecular Pharmaceutics **5**, 316-27 (2008)

160. Toma A, Otsuji E, Kuriu Y, Okamoto K, Ichikawa D, Hagiwara A, et al. Monoclonal antibody A7-superparamagnetic iron oxide as contrast agent of MR imaging of rectal carcinoma. Br J Cancer **93**, 131-6 (2005)

161. Holash J, Maisonpierre PC, Compton D, Boland P, Alexander CR, Zagzag D, et al. Vessel Cooption, Regression, and Growth in Tumors Mediated by Angiopoietins and VEGF. Science **284**, 1994-8 (1999)

162. Tanaka S, Kitamura T, Fujita M, Nakanishi K, Okuda S. Color Doppler flow imaging of liver tumors. Am J Roentgenol **154**, 509-14 (1990)

163. Reya T, Morrison SJ, Clarke MF, Weissman IL. Stem cells, cancer, and cancer stem cells. Nature **414**, 105-11 (2001)

164. Gerner EW, Schneider MJ. Induced thermal resistance in HeLa cells. Nature **256**, 500-2 (1975)

165. Henle KJ. Sensitization to hyperthermia below 43 degrees C induced in Chinese hamster ovary cells by step-down heating. J Natl Cancer Inst **64**, 1479-83 (1980)

166. Leopold KA, Dewhirst M, Samulski T, Harrelson J, Tucker JA, George SL, et al. Relationships among tumor temperature, treatment time, and histopathological outcome using preoperative hyperthermia with radiation in soft tissue sarcomas. International Journal of Radiation Oncology*Biology*Physics **22**, 989-98 (1992)

167. Jones EL, Oleson JR, Prosnitz LR, Samulski TV, Vujaskovic Z, Yu D, et al. Randomized Trial of Hyperthermia and Radiation for Superficial Tumors. Journal of Clinical Oncology **23**, 3079-85 (2005)

168. Ito A, Tanaka K, Kondo K, Shinkai M, Honda H, Matsumoto K, et al. Tumor regression by combined immunotherapy and hyperthermia using magnetic nanoparticles in an experimental subcutaneous murine melanoma. Cancer Science **94**, 308-13 (2003)

169. Ito A, Kuga Y, Honda H, Kikkawa H, Horiuchi A, Watanabe Y, et al. Magnetite nanoparticle-loaded anti-HER2 immunoliposomes for combination of antibody therapy with hyperthermia. Cancer Letters **212**, 167-75 (2004)

170. Gonzales M, Krishnan KM. Synthesis of magnetoliposomes with monodisperse iron oxide nanocrystal cores for hyperthermia. Journal of Magnetism and Magnetic Materials **293**, 265-70 (2005)

171. Callera F, de Melo CuMTP. Magnetic Resonance Tracking of Magnetically Labeled Autologous Bone Marrow CD34+ Cells Transplanted into the Spinal Cord via Lumbar Puncture Technique in Patients with Chronic Spinal Cord Injury: CD34+ Cells' Migration into the Injured Site. Stem Cells and Development **16**, 461-6 (2007)

172. Barbosa da Fonseca LM, Battistella V, de Freitas GR, Gutfilen B, dos Santos Goldenberg RC, Maiolino A, et al. Early Tissue Distribution of Bone Marrow Mononuclear Cells After Intra-Arterial Delivery in a Patient With Chronic Stroke. Circulation **120**, 539-41 (2009)

173. Chin BB, Nakamoto Y, Bulte JW, Pittenger MF, Wahl R, Kraitchman DL. 111In oxine labelled mesenchymal stem cell SPECT after intravenous administration in myocardial infarction. Nucl Med Commun **24**, 1149-54 (2003)

174. Hofmann M, Wollert KC, Meyer GP, Menke A, Arseniev L, Hertenstein B, et al. Monitoring of Bone Marrow Cell Homing Into the Infarcted Human Myocardium. Circulation **111**, 2198-202 (2005)

175. Kang WJ, Kang HJ, Kim HS, Chung JK, Lee MC, Lee DS. Tissue Distribution of 18F-FDG-Labeled Peripheral Hematopoietic Stem Cells After Intracoronary Administration in Patients with Myocardial Infarction. Journal of Nuclear Medicine **47**, 1295-301 (2006)

176. Freed CR, Greene PE, Breeze RE, Tsai WY, DuMouchel W, Kao R, et al. Transplantation of Embryonic Dopamine Neurons for Severe Parkinson's Disease. New England Journal of Medicine **344**, 710-9 (2001)

177. Cao F, Lin S, Xie X, Ray P, Patel M, Zhang X, et al. In Vivo Visualization of Embryonic Stem Cell Survival, Proliferation, and Migration After Cardiac Delivery. Circulation **113**, 1005-14 (2006)

178. Contag CH, Bachmann MH. Advances in in vivo bioluminescence imaging of gene expression. Annu Rev Biomed Eng **4**, 235-60 (2002)

179. Edinger M, Cao YA, Verneris MR, Bachmann MH, Contag CH, Negrin RS. Revealing lymphoma growth and the efficacy of immune cell therapies using in vivo bioluminescence imaging. Blood **101**, 640-8 (2003)

180. Aikawa E, Nahrendorf M, Sosnovik D, Lok VM, Jaffer FA, Aikawa M, et al. Multimodality Molecular Imaging Identifies Proteolytic and Osteogenic Activities in Early Aortic Valve Disease. Circulation **115**, 377-86 (2007)

181. Evgenov NV, Medarova Z, Dai G, Bonner-Weir S, Moore A. In vivo imaging of islet transplantation. Nat Med **12**, 144-8 (2006)

182. Fowler M, Virostko J, Chen Z, Poffenberger G, Radhika A, Brissova M, et al. Assessment of Pancreatic Islet Mass after Islet Transplantation Using In Vivo Bioluminescence Imaging. Transplantation **79**, (2005)

183. Bulte JWM, Kraitchman DL. Iron oxide MR contrast agents for molecular and cellular imaging. NMR in Biomedicine **17**, 484-99 (2004)

184. Koenig SH, Kellar KE. Theory of 1/T1 and 1/T2 NMRD profiles of solutions of magnetic nanoparticles. Magnetic Resonance in Medicine **34**, 227-33 (1995)

185. Rogers WJ, Meyer CH, Kramer CM. Technology Insight: in vivo cell tracking by use of MRI. Nat Clin Pract Cardiovasc Med **3**, 554-62 (2006)

186. E.M.Winter, B.Hogers, van dG, Gittenberger-de G, R.E.Poelmann, van dW. Cell tracking using iron oxide fails to distinguish dead from living transplanted cells in the infarcted heart. Magnetic Resonance in Medicine **63**, 817-21 (2010)

187. Daniel JS, Carolyn AC, Enca M, Damian JT, Corinne W, Paul JC, et al. Iron Particles for Noninvasive Monitoring of Bone Marrow Stromal Cell Engraftment into, and Isolation of Viable Engrafted Donor Cells from, the Heart. Stem Cells **24**, 1968-75 (2006)

188. Kraitchman DL, Heldman AW, Atalar E, Amado LC, Martin BJ, Pittenger MF, et al. In Vivo Magnetic Resonance Imaging of Mesenchymal Stem Cells in Myocardial Infarction. Circulation **107**, 2290-3 (2003)

189. Kanno S, Wu YJL, Lee PC, Dodd SJ, Williams M, Griffith BP, et al. Macrophage Accumulation Associated With Rat Cardiac Allograft Rejection Detected by Magnetic Resonance Imaging With Ultrasmall Superparamagnetic Iron Oxide Particles. Circulation **104**, 934-8 (2001)

190. Ye Q, Yang D, Williams M, Williams DS, Pluempitiwiriyawej C, Moura JM, et al. In vivo detection of acute rat renal allograft rejection by MRI with USPIO particles. Kidney Int **61**, 1124-35 (2002)

191. Zhang Y, Dodd SJ, Hendrich KS, Williams M, Ho C. Magnetic resonance imaging detection of rat renal transplant rejection by monitoring macrophage infiltration. Kidney Int **58**, 1300-10 (2000)

192. Higuchi T, Anton M, Dumler K, Seidl S, Pelisek J, Saraste A, et al. Combined Reporter Gene PET and Iron Oxide MRI for Monitoring Survival and Localization of Transplanted Cells in the Rat Heart. Journal of Nuclear Medicine **50**, 1088-94 (2009)

193. Pawelczyk E, Arbab AS, Chaudhry A, Balakumaran A, Robey PG, Frank JA. In Vitro Model of Bromodeoxyuridine or Iron Oxide Nanoparticle Uptake by Activated Macrophages from Labeled Stem Cells: Implications for Cellular Therapy. Stem Cells **26**, 1366-75 (2008)

194. Pawelczyk E, Jordan EK, Balakumaran A, Chaudhry A, Gormley N, Smith M, et al. In Vivo Transfer of Intracellular Labels from Locally Implanted Bone Marrow Stromal Cells to Resident Tissue Macrophages. PLoS ONE **4**, e6712 (2009)

195. Kuhlpeter R, Dahnke H, Matuszewski L, Persigehl T, von Wallbrunn A, Allkemper T, et al. R2 and R2* Mapping for Sensing Cell-bound Superparamagnetic Nanoparticles: In Vitro and Murine in Vivo Testing. Radiology **245**, 449-57 (2007)

196. Rigol M, Solanes N, Roqué M, Farré J, Batlle M, Roura S, et al. Hemosiderin Deposits Confounds Tracking of Iron-Oxide-Labeled Stem Cells: An Experimental Study. Transplantation Proceedings **40**, 3619-22 (2008)

197. van den Bos EJ, Baks T, Moelker AD, Kerver W, van Geuns RJ, van der Giessen WJ, et al. Magnetic resonance imaging of haemorrhage within reperfused myocardial infarcts:

possible interference with iron oxide-labelled cell tracking? European Heart Journal **27**, 1620-6 (2006)

198. Shapiro EM, Sharer K, Skrtic S, Koretsky AP. In vivo detection of single cells by MRI. Magnetic Resonance in Medicine **55**, 242-9 (2006)

199. Walczak P, Kedziorek DA, Gilad AA, Barnett BP, Bulte JWM. Applicability and limitations of MR tracking of neural stem cells with asymmetric cell division and rapid turnover: The case of the Shiverer dysmyelinated mouse brain. Magnetic Resonance in Medicine **58**, 261-9 (2007)

200. Cunningham CH, Arai T, Yang PC, McConnell MV, Pauly JM, Conolly SM. Positive contrast magnetic resonance imaging of cells labeled with magnetic nanoparticles. Magnetic Resonance in Medicine **53**, 999-1005 (2005)

201. Girard OM, Du J, Agemy L, Sugahara KN, Kotamraju VR, Ruoslahti E, et al. Optimization of iron oxide nanoparticle detection using ultrashort echo time pulse sequences: Comparison of T1, T2*, and synergistic T1 and T2* contrast mechanisms. Magnetic Resonance in Medicine **65**, 1649-60 (2011)

202. Mani V, Adler E, Briley-Saebo KC, Bystrup A, Fuster V, Keller G, et al. Serial in vivo positive contrast MRI of iron oxide-labeled embryonic stem cell-derived cardiac precursor cells in a mouse model of myocardial infarction. Magnetic Resonance in Medicine **60**, 73-81 (2008)

203. Suzuki Y, Cunningham CH, Noguchi Ki, Chen IY, Weissman IL, Yeung AC, et al. In vivo serial evaluation of superparamagnetic iron-oxide labeled stem cells by off-resonance positive contrast. Magnetic Resonance in Medicine **60**, 1269-75 (2008)

204. Dahnke H, Liu W, Herzka D, Frank JA, Schaeffter T. Susceptibility gradient mapping (SGM): A new postprocessing method for positive contrast generation applied to superparamagnetic iron oxide particle (SPIO)-labeled cells. Magnetic Resonance in Medicine **60**, 595-603 (2008)

205. Cohen B, Ziv K, Plaks V, Israely T, Kalchenko V, Harmelin A, et al. MRI detection of transcriptional regulation of gene expression in transgenic mice. Nat Med **13**, 498-503 (2007)

206. Deans AE, Wadghiri YZ, Bernas LM, Yu X, Rutt BK, Turnbull DH. Cellular MRI contrast via coexpression of transferrin receptor and ferritin. Magnetic Resonance in Medicine **56**, 51-9 (2006)

207. Gilad AA, McMahon MT, Walczak P, Winnard PT, Raman V, van Laarhoven HWM, et al. Artificial reporter gene providing MRI contrast based on proton exchange. Nat Biotech **25**, 217-9 (2007)

208. Liu G, Bulte JW, Gilad AA. CEST MRI reporter genes. Methods Mol Biol **711**, 271-80 (2011)

209. Louie AY, Huber MM, Ahrens ET, Rothbacher U, Moats R, Jacobs RE, et al. In vivo visualization of gene expression using magnetic resonance imaging. Nat Biotech **18**, 321-5 (2000)

210. Pérez-Torres CJ, Massaad CA, Hilsenbeck SG, Serrano F, Pautler RG. In vitro and in vivo magnetic resonance imaging (MRI) detection of GFP through magnetization transfer contrast (MTC). NeuroImage **50**, 375-82 (2010)

211. Gambhir SS, Barrio JR, Herschman HR, Phelps ME. Assays for noninvasive imaging of reporter gene expression. Nuclear Medicine and Biology **26**, 481-90 (1999)

212. Gambhir SS, Barrio JR, Wu L, Iyer M, Namavari M, Satyamurthy N, et al. Imaging of Adenoviral-Directed Herpes Simplex Virus Type 1 Thymidine Kinase Reporter Gene Expression in Mice with Radiolabeled Ganciclovir. Journal of Nuclear Medicine **39**, 2003-11 (1998)

213. Hara T, Kosaka N, Kishi H. Development of 18F-Fluoroethylcholine for Cancer Imaging with PET: Synthesis, Biochemistry, and Prostate Cancer Imaging. Journal of Nuclear Medicine **43**, 187-99 (2002)

214. Schlemmer HP, Pichler BJ, Schmand M, Burbar Z, Michel C, Ladebeck R, et al. Simultaneous MR/PET Imaging of the Human Brain: Feasibility Study1. Radiology **248**, 1028-35 (2008)

215. Wehrl H, Judenhofer M, Wiehr S, Pichler B. Pre-clinical PET/MR: technological advances and new perspectives in biomedical research. European Journal of Nuclear Medicine and Molecular Imaging **36**, 56-68 (2009)

216. Weissleder R, Pittet MJ. Imaging in the era of molecular oncology. Nature **452**, 580-9 (2008)

217. Wang YX, Hussain SM, Krestin GP. Superparamagnetic iron oxide contrast agents: physicochemical characteristics and applications in MR imaging. Eur Radiol **11**, 2319-31 (2001)

218. Artemov D, Mori N, Okollie B, Bhujwalla ZM. MR molecular imaging of the Her-2/neu receptor in breast cancer cells using targeted iron oxide nanoparticles. Magnetic Resonance in Medicine **49**, 403-8 (2003)

219. Lee JH, Huh YM, Jun Yw, Seo Jw, Jang Jt, Song HT, et al. Artificially engineered magnetic nanoparticles for ultra-sensitive molecular imaging. Nat Med **13**, 95-9 (2007)

220. Sibson NR, Blamire AM, Bernades-Silva M, Laurent S, Boutry SA, Muller RN, et al. MRI detection of early endothelial activation in brain inflammation. Magnetic Resonance in Medicine **51**, 248-52 (2004)

221. McAteer MA, Sibson NR, von zur Muhlen C, Schneider JE, Lowe AS, Warrick N, et al. In vivo magnetic resonance imaging of acute brain inflammation using microparticles of iron oxide. Nat Med **13**, 1253-8 (2007)

222. Winter PM, Morawski AM, Caruthers SD, Fuhrhop RW, Zhang H, Williams TA, et al. Molecular Imaging of Angiogenesis in Early-Stage Atherosclerosis With {alpha}v{beta}3-Integrin-Targeted Nanoparticles. Circulation **108**, 2270-4 (2003)

223. Kooi ME, Cappendijk VC, Cleutjens KBJM, Kessels AGH, Kitslaar PJEH, Borgers M, et al. Accumulation of Ultrasmall Superparamagnetic Particles of Iron Oxide in Human Atherosclerotic Plaques Can Be Detected by In Vivo Magnetic Resonance Imaging. Circulation **107**, 2453-8 (2003)

224. Avilés MO, Ebner AD, Ritter JA. Implant assisted-magnetic drug targeting: Comparison of in vitro experiments with theory. Journal of Magnetism and Magnetic Materials **320**, 2704-13 (2008)

225. Polyak B, Fishbein I, Chorny M, Alferiev I, Williams D, Yellen B, et al. High field gradient targeting of magnetic nanoparticle-loaded endothelial cells to the surfaces of steel stents. Proceedings of the National Academy of Sciences **105**, 698-703 (2008)

226. Tamaz S, Gourdeau R, Chanu A, Mathieu JB, Martel S. Real-Time MRI-Based Control of a Ferromagnetic Core for Endovascular Navigation. Biomedical Engineering, IEEE Transactions on **55**, 1854-63 (2008)

227. Yerebakan C, Kaminski A, Westphal B, Liebold A, Steinhoff G. Autologous bone marrow stem cell therapy for the ischemic myocardium during coronary artery bypass grafting. Minimally Invasive Therapy and Allied Technologies **17**, 143-8 (2008)

228. Nesselmann C, Ma N, Bieback K, Wagner W, Ho A, Konttinen YT, Zhang H, Hinescu ME, Steinhoff G.. Mesenchymal stem cells and cardiac repair. Journal of Cellular and Molecular Medicine **12**, 1795-810 (2008)

229. Tateishi-Yuyama E, Matsubara H, Murohara T, Ikeda U, Shintani S, Masaki H, et al. Therapeutic angiogenesis for patients with limb ischaemia by autologous transplantation of bone-marrow cells: a pilot study and a randomised controlled trial. The Lancet **360**, 427-35 (2002)

230. Hinds KA, Hill JM, Shapiro EM, Laukkanen MO, Silva AC, Combs CA, et al. Highly efficient endosomal labeling of progenitor and stem cells with large magnetic particles allows magnetic resonance imaging of single cells. Blood **102**, 867-72 (2003)

231. Kettering M, Winter J, Zeisberger M, Bremer-Streck S, Oehring H, Bergemann C, et al. Magnetic nanoparticles as bimodal tools in magnetically induced labelling and magnetic heating of tumour cells: an in vitro study. Nanotechnology **18**, 175101 (2007)

232. Mathieu JB, Martel S. Aggregation of magnetic microparticles in the context of targeted therapies actuated by a magnetic resonance imaging system. Journal of Applied Physics **106**, 044904-7 (2009)

233. Pouponneau P, Leroux JC, Martel S. Magnetic nanoparticles encapsulated into biodegradable microparticles steered with an upgraded magnetic resonance imaging system for tumor chemoembolization. Biomaterials **30**, 6327-32 (2009)

234. Han BH, Park S, Lee SY. Gradient waveform synthesis for magnetic propulsion using MRI gradient coils. Physics in Medicine and Biology **53**, 4639-49 (2008)

235. Leith D. Drag on Nonspherical Objects. Aerosol Science and Technology **6**, 153-61 (1987)

236. Erica MC, Peter GM, John KE. Particle size, magnetic field, and blood velocity effects on particle retention in magnetic drug targeting. Medical Physics **37**, 175-82 (2010)

237. Mohanty S, Baier T, Schoenfeld F. CFD Modelling of Cell Capture in BioMEMs. Proceedings of the World Congress on Engineering and Computer Science 2008 , (2008)

238. Takeda Si, Mishima F, Terazono B, Izumi Y, Nishijima S. Development of magnetic force-assisted gene transfer system using biopolymer-coated ferromagnetic nanoparticles. Science and Technology of Advanced Materials **7**, 308-14 (2006)

239. Azuma H, Funayama N, Kubota T, Ishikawa M. Regeneration of endothelial cells after balloon denudation of the rabbit carotid artery and changes in responsiveness. Jpn J Pharmacol **52**, 541-52 (1990)

240. Hui DY. Intimal hyperplasia in murine models. Curr Drug Targets **9**, 251-60 (2008)

241. Painter TA. Myointimal hyperplasia: pathogenesis and implications. 2. Animal injury models and mechanical factors. Artif Organs **15**, 103-18 (1991)

242. Heiberg E, Sjogren J, Ugander M, Carlsson M, Engblom H, Arheden H. Design and validation of Segment - freely available software for cardiovascular image analysis. BMC Medical Imaging **10**, 1 (2010)

243. Cui X, Labarrere C, He L, Cheng S, Siderys H, Kovacs R, et al. Cryopreservation and Microsurgical Implantation of Rabbit Carotid Arteries. Cell Preservation Technology **1**, 121-8 (2002)

244. Sato H, Katano M, Takigawa T, Masuda T. Estimation for the elasticity of vascular endothelial cells on the basis of atomic force microscopy and Young's modulus of gelatin gels. Polymer Bulletin **47**, 375-81 (2001)

245. Bjork R, Bahl CRH, Smith A, Pryds N. Optimization and improvement of Halbach cylinder design. Journal of Applied Physics **104**, 013910-9 (2008)

246. Arruebo M, Fernβndez-Pacheco R, Ibarra MR, Santamar∅a Js. Magnetic nanoparticles for drug delivery. Nano Today **2**, 22-32 (2007)

247. Kumar A, Jena PK, Behera S, Lockey RF, Mohapatra S, Mohapatra S. Multifunctional magnetic nanoparticles for targeted delivery. Nanomedicine **6,** 64-9, (2009)

248. Molday RS, Yen SPS, Rembaum A. Application of magnetic microspheres in labelling and separation of cells. Nature , 437-8 (1977)

249. Häfeli UO, Gilmour K, Zhou A, Lee S, Hayden ME. Modeling of magnetic bandages for drug targeting: Button vs. Halbach arrays. Journal of Magnetism and Magnetic Materials **311**, 323-9 (2007)

250. Cregg PJ, Murphy K, Mardinoglu A, Prina-Mello A. Many particle magnetic dipole-dipole and hydrodynamic interactions in magnetizable stent assisted magnetic drug targeting. Journal of Magnetism and Magnetic Materials **322,** 2087-94 (2010)

251. Terrovitis JV, Bulte JWM, Sarvananthan S, Crowe LA, Sarathchandra P, Batten P, et al. Magnetic Resonance Imaging of Ferumoxide-Labeled Mesenchymal Stem Cells Seeded on Collagen Scaffolds-Relevance to Tissue Engineering. Tissue Engineering **12**, 2765-75 (2006)

252. Kim YJ, Kuh YM, Choe KO, Choi BW, Choi EJ, Jang Y, et al. In vivo magnetic resonance imaging of injected mesenchymal stem cells in rat myocardial infarction; simultaneous cell tracking and left ventricular function measurement. The International Journal of Cardiobascular Imaging **25**, 99-109 (2009)

253. Constantine G, Shan K, Flamm SD, Sivananthan MU. Role of MRI in clinical cardiology. The Lancet **363**, 2162-71 (2004)

254. Nahrendorf M, Sosnovik DE, French BA, Swirski FK, Bengel F, Sadeghi MM, et al. Multimodality Cardiovascular Molecular Imaging, Part II. Circ Cardiovasc Imaging **2**, 56-70 (2009)

255. Vallee JP, Ivancevic MK, Nguyen D, Morel DR, Jaconi M. Current status of cardiac MRI in small animals. MAGMA **17**, 149-56 (2004)

256. Daniel JS, Carolyn AC, Damian JT, Kieran C. Cine-MRI versus two-dimensional echocardiography to measure in vivo left ventricular function in rat heart. NMR in Biomedicine **21**, 765-72 (2008)

257. Zhang L, Xue H, Cao Z, Keefe A, Wang J, Jiang S. Multifunctional and degradable zwitterionic nanogels for targeted delivery, enhanced MR imaging, reduction-sensitive drug release, and renal clearance. Biomaterials **32**, 4604-8 (2011)

258. Modo M, Cash D, Mellodew K, Williams SCR, Fraser SE, Meade TJ, et al. Tracking Transplanted Stem Cell Migration Using Bifunctional, Contrast Agent-Enhanced, Magnetic Resonance Imaging. NeuroImage **17**, 803-11 (2002)

259. Shapiro EM, Skrtic S, Sharer K, Hill JM, Dunbar CE, Koretsky AP. MRI detection of single particles for cellular imaging. Proceedings of the National Academy of Sciences of the United States of America **101**, 10901-6 (2004)